

Quarterly Report for
Contract DE-FG36-08GO18192
Stanford Geothermal Program
October-December 2011

Table of Contents

1. FRACTURE CHARACTERIZATION USING PRODUCTION DATA	3
1.1 SUMMARY	3
1.2 INTRODUCTION	3
1.3 PARAMETRIC KERNEL ESTIMATION THEORY	4
1.4 NONPARAMETRIC KERNEL ESTIMATION THEORY	8
1.5 KERNEL ESTIMATION WITH A SIMPLE RESERVOIR MODEL	12
1.6 KERNEL ESTIMATION WITH A LARGE RESERVOIR MODEL	28
2. FRACTURE CHARACTERIZATION OF ENHANCED GEOTHERMAL SYSTEMS USING NANOPARTICLES	47
2.1 SUMMARY	47
2.2 INTRODUCTION	47
2.3 MICROMODEL EXPERIMENTS	48
2.4 SYNTHESIS AND CHARACTERIZATION OF TIN-BISMUTH NANOPARTICLES	56
2.5 RESULTS	58
2.5 FUTURE WORK	61
3. FRACTURE CHARACTERIZATION USING RESISTIVITY	63
3.1 SUMMARY	63
3.2 INTRODUCTION	63
3.3 WATER FLOW ANALOGY OF ELECTRICAL FLOW	65
3.4 RESISTIVITY OF A SALINE TRACER SOLUTION	66
3.5 TWO SIMPLE FRACTURE NETWORKS	68
3.6 DISCRETE FRACTURE NETWORKS	71
3.7 FUTURE WORK	80
4. FRACTURE APERTURE DETERMINATION USING THERMAL AND TRACER DATA	83
4.1 SUMMARY	83

4.2 INTRODUCTION	83
4.3 METHODOLOGY	84
4.4 PRELIMINARY CALCULATIONS AND RESULTS	87
4.5 REVIEW OF RELATED LITERATURE	90
4.6 FUTURE WORK	96
5. REFERENCES	99

1. FRACTURE CHARACTERIZATION USING PRODUCTION DATA

This research project is being conducted by Research Assistant Egill Juliusson, Senior Research Engineer Kewen Li and Professor Roland Horne. The objective of this project is to investigate ways to characterize fractured geothermal reservoirs using production data.

1.1 SUMMARY

This report describes a revised method for analyzing tracer returns using parametric and nonparametric regression methods.

With the revised method, the tracer kernel is first predicted using a nonlinear parametric function. This parametric estimate is somewhat restricted in shape, but that can be fixed by using a nonparametric model. Regularizing and finding an appropriate discretization for a nonparametric model can be challenging, but this challenge can be met by using the parametric estimate as a prior for the nonparametric model. This had been solved previously by using a Genetic Algorithm to find the optimal set of discretization points.

The applicability of this revised method is illustrated by four examples. Two examples are given with data from a simple synthetic reservoir with three fractures, the first of which involves varying concentration and constant flow rates; the second involves varying flow rates and a ramp increase in injected concentrations. The same two scenarios were simulated with a model based on the Soultz reservoir in France.

1.2 INTRODUCTION

A multiwell tracer test will have different types of tracer going into each injection well, so as not to create any confusion about where the tracer originates from. However, there are situations where the same tracer, e.g. a natural recirculating chemical compound, could be going into all of the injection wells at once. An example of such data comes from the Palinpinon field in the Philippines, where the chloride concentration in the produced brine showed distinct variations over a 15 year production period. Figure 1.1 shows the chloride concentration in production well PN-29D, along with the variation in injection rates into each of the injection wells PN-1RD through PN-9RD. The chloride concentration of the reinjected brine had an increasing trend because part of the fluid produced from the reservoir was separated as steam going to the power plant.

Urbino and Horne (1991), Sullera and Horne (2001), Horne and Szucs (2007), and Basel et al. (2011) have worked on decoding this data set without conclusive results on how much information can be obtained. Working with the Palinpinon data was challenging because the data were sparsely sampled, a large number of predictors (nine injection wells) were influencing the response, the production rates were not available and two phase flow in the reservoir may have been affecting the tracer flow paths in highly nonlinear ways.

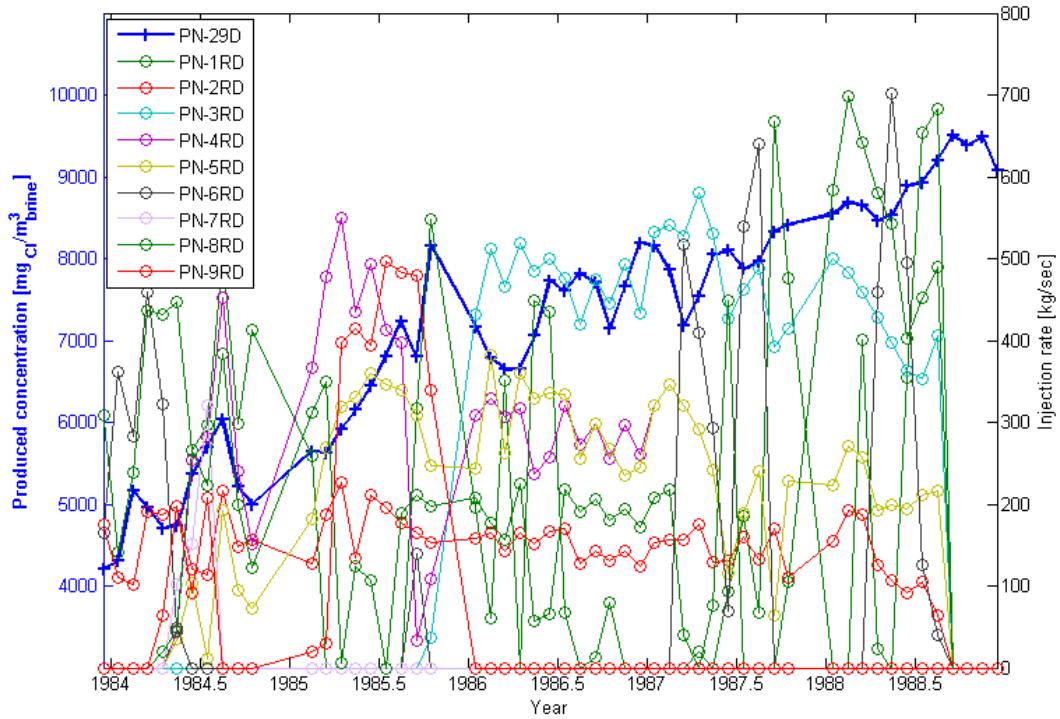


Figure 1.1: History of injection rates and produced chloride concentration in well PN-29D, in the Palinpinion field, Philippines.

In an effort to start answering questions about how much information could be obtained from this type of data it was deemed most practical to work on similar data sets that were created using numerical flow simulation models. This report describes ways to solve the multiwell tracer transport problem, where the same tracer is being injected into more than one well. This will focus, in particular, on ways by which the tracer transfer function, or tracer kernel, can be estimated. Examples will be given on how to estimate the tracer kernel at constant and variable flow rate conditions, using both parametric and nonparametric regression methods.

1.3 PARAMETRIC KERNEL ESTIMATION THEORY

In the following discussion it will be assumed that tracer concentrations are measured in flux mode (Kreft and Zuber, 1978). Then the multiwell tracer response at producer j will be:

$$c_{Pj}(t) = \sum_{i=1}^{N_I} w_{ij}(t) \int_0^{Q_{ij}(t)} c_{ii}(Q_{ij}(t) - \tilde{Q}_{ij}) \kappa_{iiPj}(\tilde{Q}_{ij}) d\tilde{Q}_{ij} \quad (2.1)$$

where Q_{ij} denotes the cumulative flow rate going from injector i to producer j , and the weighting parameter w accounts for the mixing of fluids at the producer:

$$w_{ij}(t) = \int_0^t \frac{q_{IiPj}(\tau)}{q_{Pj}(\tau)} \frac{e^{-\frac{t-\tau}{T}}}{T} d\tau \quad (2.2)$$

The flow rate is denoted by q and T is a time constant which accounts for the mixing time. The flow rate going from injector i to producer j can be computed based on an estimate of the interwell connectivity as introduced by Lee et al. (2010).

Estimating the tracer kernel with a given physical (parametric) model proved to be a relatively robust and practical way of solving the multiwell tracer transport problem. In this case the parametric model for the kernels was assumed to be

$$\kappa_{IiPj}(Q_{ij}|V_{x,IiPj}, V_{d,IiPj}, f_{IiPj}) = \frac{f_{IiPj}V_{x,IiPj}}{\sqrt{4\pi V_{d,IiPj}Q_{ij}^3}} e^{-\frac{(V_{x,IiPj}-Q_{ij})^2}{4V_{d,IiPj}Q_{ij}}} \quad (2.3)$$

where the unknown parameters were the augmented pore volume $V_{x,IiPj}$, the augmented dispersion volume, $V_{d,IiPj}$, and f_{IiPj} , which is a parameter that should ideally equal one. The parameter f was added to the model to account for possible errors in the mixing weight, thus allowing the regression model to emphasize or deemphasize the importance of each kernel on the response. These unknown parameters were sometimes grouped into the vector $\alpha_{ij} = [V_{x,IiPj}, V_{d,IiPj}, f_{IiPj}]$, or $\alpha_j = [\alpha_{1j} \dots \alpha_{N_j}]$, for notational convenience.

The parametric estimation problem builds on using nonlinear regression methods to find those parameters which provide the best match between the observed data and the model. This was achieved based on the following constrained least squares problem

$$\begin{aligned} \min_{\alpha_j} O(\alpha_j) &= (\mathbf{c}_{Pj} - \mathbf{H}_j \boldsymbol{\kappa}_j(\alpha_j))^T (\mathbf{c}_{Pj} - \mathbf{H}_j \boldsymbol{\kappa}_j(\alpha_j)) \\ \text{s. t.} \quad \alpha_j &\geq \mathbf{lb} \\ \alpha_j &\leq \mathbf{ub} \end{aligned} \quad (2.4)$$

Several of the variables in this equation need further definition. The matrix \mathbf{H}_j represents an approximation of Equation (2.1), i.e.

$$\mathbf{c}_{Pj} \approx \mathbf{H}_j \boldsymbol{\kappa}_j(\alpha_j) \quad (2.5)$$

where

$$\frac{\partial \mathbf{O}(\boldsymbol{\alpha}_j)}{\partial \boldsymbol{\alpha}_j} = \begin{bmatrix} \left(\mathbf{H}_{I_1 P_j} \frac{\partial \boldsymbol{\kappa}_{I_1 P_j}}{\partial \alpha_{1j,1}} \right)^T \\ \left(\mathbf{H}_{I_1 P_j} \frac{\partial \boldsymbol{\kappa}_{I_1 P_j}}{\partial \alpha_{1j,2}} \right)^T \\ \vdots \\ \left(\mathbf{H}_{I_{N_I} P_j} \frac{\partial \boldsymbol{\kappa}_{I_{N_I} P_j}}{\partial \alpha_{N_I j,1}} \right)^T \end{bmatrix} \left(\mathbf{c}_{P_j} - \mathbf{H}_j \boldsymbol{\kappa}_j(\boldsymbol{\alpha}_j) \right) = \mathbf{J}_j^T \Delta \mathbf{r}_j \quad (2.11)$$

The Hessian was approximated with only the first derivative terms. Thus, it could be computed from the Jacobian, \mathbf{J} , as

$$\frac{\partial^2 \mathbf{O}(\boldsymbol{\alpha}_j)}{\partial \boldsymbol{\alpha}_j^2} = \mathbf{J}_j^T \mathbf{J}_j \quad (2.12)$$

The full structure of the Hessian, i.e. with the second derivative terms included, was given in the Quarterly Report from Spring 2010. However, the second derivative terms are often left out (Gauss-Newton method), and that proved computationally efficient in this case.

The analytical equations for the derivative of the kernel functions with respect to V_x , V_d and f , were computed automatically using the Symbolic Toolbox in MATLAB. The MATLAB function *fmincon* was then used to solve problem (2.4), using the trust-region-reflective algorithm. The objective function had a number of local minima and therefore it was necessary to try a few different initial guesses to get convergence to the "true" solution. A Genetic Algorithm was applied to provide a structured approach to finding a good initial guess for $\boldsymbol{\alpha}_j$.

In practice, tracer breakthrough usually occurs only in part of the production wells. Solving the multiwell tracer deconvolution problem when this is the case becomes a bit more challenging because in the model one assumes that all injectors influence the producer. But by looking at the sensitivity of the production data to the injection data it may be possible to find out which kernels were reproduced with high dependence on the data and which ones were mostly dependent on random noise. Having this information could be valuable because it provides further understanding of which injector-producer pairs have any significant connection. Rigorous methods to test hypotheses of whether or not a parameter is significant are well known for unconstrained linear regression models. Problem (2.4), however, is nonlinear and constrained. Therefore a heuristic method was devised to determine which kernel estimates were the most significant, albeit based on similar principles as used in hypothesis testing with linear regression models.

The test statistic used was based on parameter uncertainties which were obtained based on the values of the Hessian matrix at the final solution. The covariance matrix for the kernel parameters, $\boldsymbol{\alpha}_j$ was computed as

$$\Sigma_j = \hat{\sigma}_{r_j} (\hat{J}_j^T \hat{J}_j)^{-1} \quad (2.13)$$

where σ_r denotes the sample variance of the residuals

$$\hat{\sigma}_r = \frac{(\mathbf{c}_{Pj} - \hat{\mathbf{c}}_{Pj})^T (\mathbf{c}_{Pj} - \hat{\mathbf{c}}_{Pj})}{n - 3N_I} \quad (2.14)$$

and the $\hat{\cdot}$ denotes the best estimate.

For testing the influence of each kernel on the output it seemed logical to focus on the multipliers f_{iPj} , because they represented a linear scaling of the kernel function. If the influence of a kernel was small, or zero, solutions with small f_{iPj} would be favored. Moreover, if there was a poor connection between injector i and producer j , the uncertainty in the corresponding kernel parameters would should be large, because there was little data to constrain that kernel estimate. Finally the IWCs (F) should be a good indicator of the influence of a particular injector-producer connection. Thus the following test statistic was computed

$$SO_{ij} = \frac{F_{iPj} f_{iPj} / \sigma_{f_{iPj}}}{\sum_{k=1}^{N_I} F_{kPj} f_{kPj} / \sigma_{f_{kPj}}} \quad (2.15)$$

This measure was then used to determine which kernels to include, e.g. by first adding the most significant kernel, then the second most significant etc., until some influence threshold was reached.

1.4 NONPARAMETRIC KERNEL ESTIMATION THEORY

The previous section focused on finding tracer kernels using a parametric model. This meant that the kernels had to take on a specific form and therefore they would not be able reproduce kernels that might arise from more complex flow patterns. One way to avoid this was to look for a nonparametric curve describing the tracer kernel. The nonparametric curve would be a set of points which represented the value of the kernel at discrete points in time. The curve was then defined by some interpolation between the points. The estimate of the nonparametric curve was somewhat susceptible to noise and therefore a regularization term had to be added to the estimation problem, to enforce some degree of smoothness on the kernel estimates.

A number of challenges were involved in delivering a good nonparametric kernel estimate. For example, it was important to find an efficient discretization scheme. Moreover, it was very helpful to have a good prior estimate for the kernel. Balancing the regularization term and the data misfit in the objective function required a bit of trial and error. Finally, parametric bootstrapping was used to assess the uncertainty in the kernel estimates.

As discussed earlier the model relating the input and output concentrations is given by Equation (2.1). This equation was approximated using with a trapezoidal discretization, shown in Equation (2.8) and repeated here:

$$\begin{aligned}
& \int_0^{Q(t)} c_{Ii}(Q(t) - \tilde{Q})\kappa(\tilde{Q})d\tilde{Q} \\
&= \sum_{k=1}^K \frac{c_{Ii}(Q(t) - \tilde{Q}_{k+1})\kappa(\tilde{Q}_{k+1}) + c_{Ii}(Q(t) - \tilde{Q}_k)\kappa(\tilde{Q}_k)}{2} (\tilde{Q}_{k+1} - \tilde{Q}_k) \\
&+ \frac{c_{Ii}(0)\kappa(Q(t)) + c_{Ii}(Q(t) - \tilde{Q}_K)\kappa(\tilde{Q}_K)}{2} (Q(t) - \tilde{Q}_K)
\end{aligned} \tag{2.16}$$

where K was defined as the number of the largest discretization element which is smaller than $Q(t)$.

When the discretization of the kernels was not equal to that of the measurement points, special attention had to be given to the last term in Equation (2.16). As long as $Q(t) \leq \tilde{Q}_m$, where m denotes the total number of discretization points, the following interpolation could be used for the last term

$$\kappa(Q(t)) = \kappa(\tilde{Q}_K) \frac{\tilde{Q}_{K+1} - Q(t)}{\tilde{Q}_{K+1} - \tilde{Q}_K} + \kappa(\tilde{Q}_{K+1}) \frac{Q(t) - \tilde{Q}_K}{\tilde{Q}_{K+1} - \tilde{Q}_K} \tag{2.17}$$

For $Q(t) > \tilde{Q}_m$ it was assumed that $\kappa(Q(t)) = 0$.

Each submatrix \mathbf{H}_{IiPj} was based on this, which yielded a structure similar to that shown in Equation (2.9). Then, in a similar manner as for the parametric case, the produced tracer concentration would be computed from

$$\mathbf{c}_{Pj} \approx \mathbf{H}_j \boldsymbol{\kappa}_j(\alpha_j) \tag{2.18}$$

where the vector $\boldsymbol{\kappa}_j$ represented all the nonparametric kernels

$$\boldsymbol{\kappa}_j = [\boldsymbol{\kappa}_{I1Pj} \dots \boldsymbol{\kappa}_{INiPj}]^T \tag{2.19}$$

and each kernel was represented by the m discretization points as

$$\boldsymbol{\kappa}_{IiPj} = [\kappa_{IiPj}(Q_{IiPj,1}) \dots \kappa_{IiPj}(Q_{IiPj,m})] \tag{2.20}$$

The matrix \mathbf{H}_j was defined as in Equation (2.7), with the mixing weights added in by premultiplication with \mathbf{W}_{IIPj} as defined in Equation (2.10).

Given this forward model for the tracer concentration, the following regularized least squares problem was formulated to determine the value of $\boldsymbol{\kappa}_j$

$$\begin{aligned} \min_{\boldsymbol{\kappa}_j} O(\boldsymbol{\kappa}_j) &= \overbrace{\frac{1}{2}(\mathbf{c}_{Pj} - \mathbf{H}_j \boldsymbol{\kappa}_j)^T (\mathbf{c}_{Pj} - \mathbf{H}_j \boldsymbol{\kappa}_j)}^{\text{data misfit}} + \overbrace{\frac{1}{2}(\boldsymbol{\kappa}_j - \boldsymbol{\kappa}_{j,prior})^T \mathbf{R}_j (\boldsymbol{\kappa}_j - \boldsymbol{\kappa}_{j,prior})}^{\text{roughness penalty}} \\ \text{s. t.} \quad &\boldsymbol{\kappa}_j > \mathbf{0} \end{aligned} \quad (2.21)$$

The roughness penalty (or regularization) matrix had the general formulation for each element

$$R_{pk}^d = \theta \sum_{i=1}^{m-d} \left((-1)^{k-i} \binom{d}{k-i} (-1)^{p-i} \binom{d}{p-i} \right) \quad (2.22)$$

where

$$\binom{d}{j} = 0 \quad \text{if } j < 0 \quad \text{or } j > d \quad (2.23)$$

The regularization term essentially added a penalty to the objective function if the kernel estimate deviated from the prior. It did this by adding or subtracting the deviations from one discretization point to the next with a given rule. The span of this smoothing scheme was dependent on the parameter d . For example, with $d = 2$, the regularization term would be

$$\frac{1}{2}(\boldsymbol{\kappa} - \boldsymbol{\kappa}_{prior})^T \mathbf{R}(\boldsymbol{\kappa} - \boldsymbol{\kappa}_{prior}) = \frac{\theta}{2} \sum_{k=2}^{m-1} \left((\kappa_{k-1} - \kappa_{k-1,prior}) - 2(\kappa_k - \kappa_{k,prior}) + (\kappa_{k+1} - \kappa_{k+1,prior}) \right)^2 \quad (2.24)$$

The gradient and Hessian were provided to help the optimization algorithm, as those could be derived from Equation (2.21) in a straightforward manner. The gradient was

$$\frac{\partial O(\boldsymbol{\kappa}_j)}{\partial \boldsymbol{\kappa}_j} = -\mathbf{H}_j^T (\mathbf{c}_{Pj} - \mathbf{H}_j \boldsymbol{\kappa}_j) + \mathbf{R}_j (\boldsymbol{\kappa}_j - \boldsymbol{\kappa}_{j,prior}) \quad (2.25)$$

and the Hessian:

$$\frac{\partial^2 O(\boldsymbol{\kappa}_j)}{\partial \boldsymbol{\kappa}_j^2} = \mathbf{H}_j^T \mathbf{H}_j + \mathbf{R}_j \quad (2.26)$$

Determining the appropriate range of the discretization terms, $d\tilde{Q}_{IPj}$, was particularly challenging. One way to approach the problem was to use an even discretization from zero to some $\tilde{Q}_{IPj,max}$, where the final value was found by global search algorithms (a Genetic Algorithm followed by a Pattern Search) (Juliussen and Horne, 2010). Clearly this would not give a unique optimal value for $\tilde{Q}_{IPj,max}$, but it helped to focus the estimation on the transient parts of the kernel (as opposed to late time parts which were essentially zero).

A more practical approach was to use the parametric kernel estimates as priors and determine an appropriate discretization based on those. In an effort to divide the kernels into parts that would contribute evenly to the production signal, the discretization as determined based on the following argument. The integral of the parametric kernel should equal f and a trapezoidal integration scheme with m points was to be used. Thus, the kernel could be divided into $m - 1$ areal sections, each with area $f/(m - 1)$. Therefore a sequence of discretization points could be found, starting from $Q_1 = 0$ by solving

$$\frac{\kappa(Q_{k+1}) + \kappa(Q_k)}{2} (Q_{k+1} - Q_k) = \frac{f}{m - 1} \quad (2.27)$$

for Q_{k+1} . The solution was found using the MATLAB routine *fminbnd* which is based on golden section search and parabolic interpolation. To ensure that $Q_{k+1} > Q_k$, Q_k was used as a lower bound on each search. The upper bound was given by $Q_k + V_x$. Theoretically, the last value in the discretization should tend to infinity. However, as a result of inaccuracy in the discretization and solution process, the last point would have some limited value. An example discretization from this method is given in Figure 1.2.

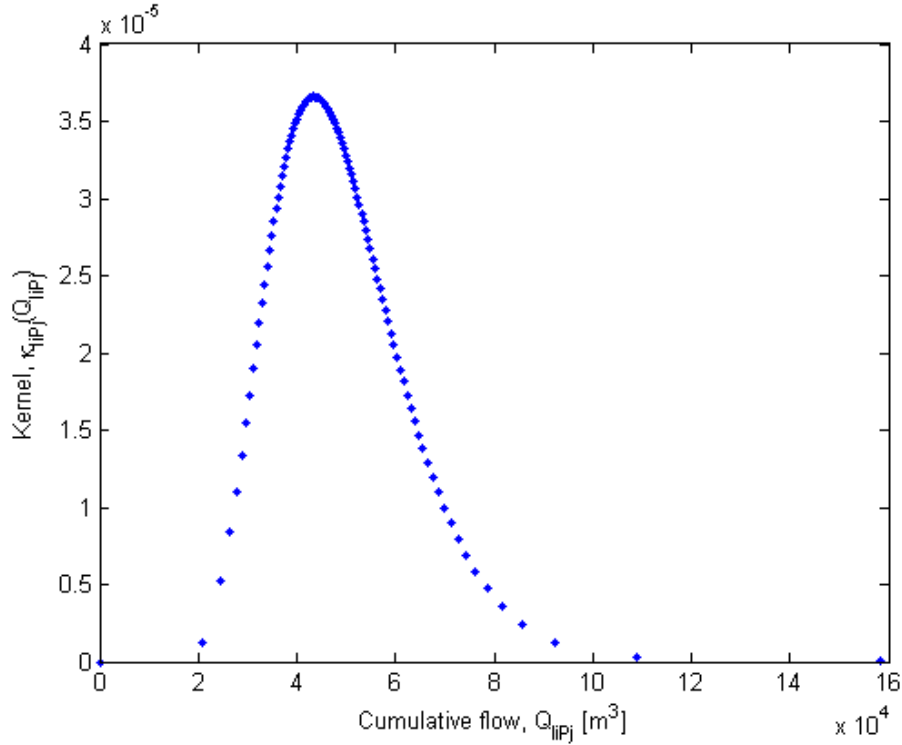


Figure 1.2: Example of a kernel discretization found using the equal area rule given by Equation (2.27). In this case there were 100 discretization points.

Estimating the uncertainty in the nonparametric kernel estimates was not straight forward because the linear regression problem (2.21) had constraints. Therefore a parametric bootstrap was used to estimate uncertainty. A parametric bootstrap is a simple way of inferring the noise in a set of data from a model fitted to that same set of data. The distribution of errors was estimated by collecting the residuals in a vector

$$\mathbf{r}_j = \mathbf{c}_{pj} - \mathbf{H}_j \boldsymbol{\kappa}_j \quad (2.28)$$

Then a new tracer production signal, c_{pj}^{sim} , was created by drawing n samples, randomly with replacement, from \mathbf{r}_j and adding them to the modeled response. This was done 1000 times and a new fit was found for each new set of simulated production data. The resulting fits were used to infer the median value of the kernel estimates, along with 95% confidence bounds.

1.5 KERNEL ESTIMATION WITH A SIMPLE RESERVOIR MODEL

The first examples of kernel estimation are shown with data generated from a simple reservoir model. This numerical reservoir model will be referred to as Model I. Model I is a two-dimensional discrete fracture model with dimensions $1000 \times 1000 \text{ m}^2$. The thickness of the two-dimensional slice was 500 m. The model had two injection wells, two production wells and three fractures, as shown in Figure 1.3. The distance between wells I1

and I2 (or P1 and P2) was 450 m, and the distance between wells I1 and P1 (or I2 and P2) was 600 m.

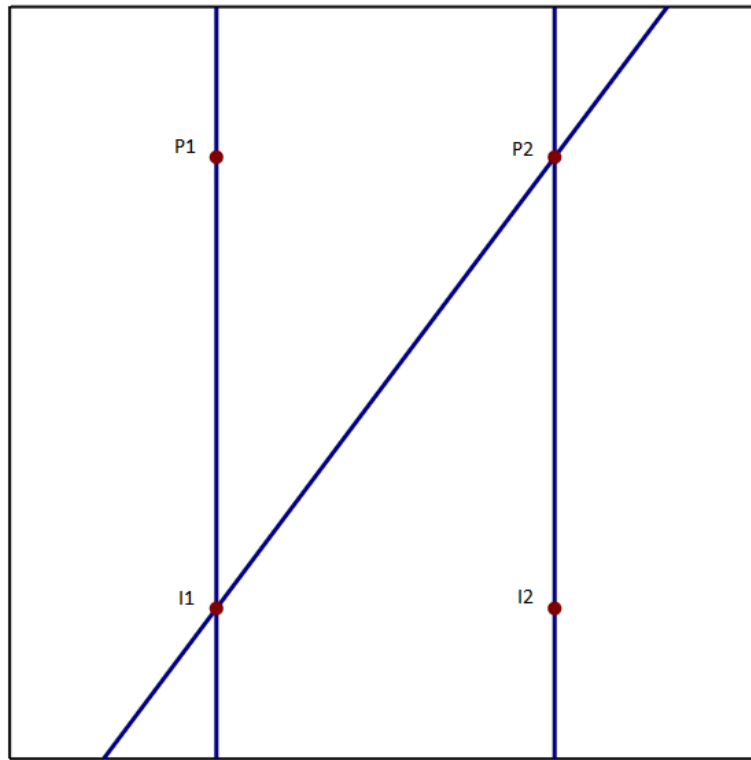


Figure 1.3: Layout of the fractures and wells in Model I.

The computational grid was generated by the triangular grid generator Triangle (Shewchuk, 1996). The grid conformed to the fractures drawn out previously, as shown in Figure 1.4. This grid had 40480 elements and 20322 nodes. The shortest element along the fracture length was around 2 m.

The fractures and matrix were given the properties specified in Table 1.1.

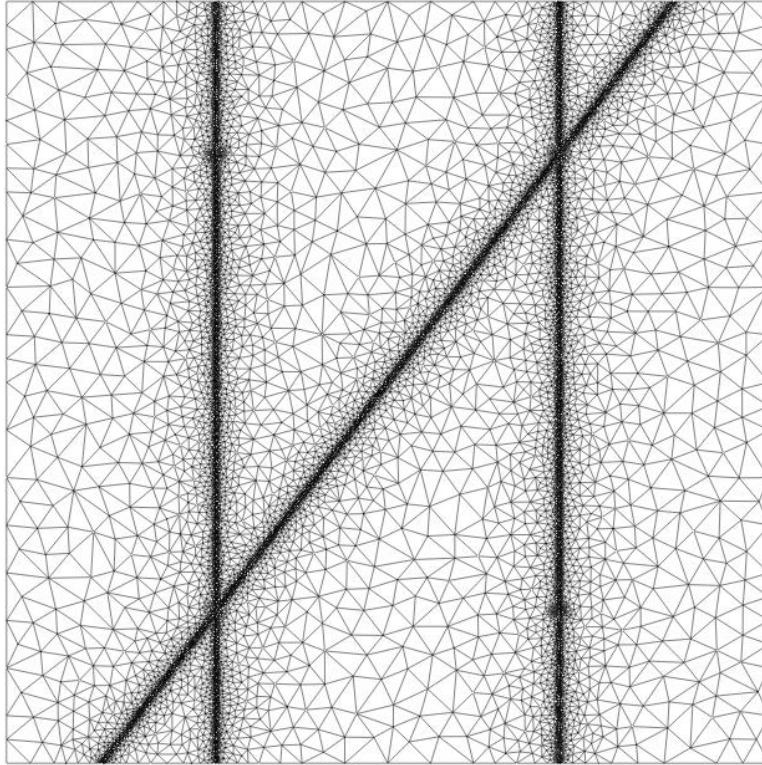


Figure 1.4: Computational grid used for Model I.

Table 1.1: Summary of properties for Reservoir Model I.

General		
	Dimensions	1000 x 1000 x 500 m ³
	Initial temperature	150 C
	Rock heat capacity	2520 kJ/m ³ /C
	Rock heat conductivity	3 J/m/s/C
	Longitudinal dispersivity	50 m
	Transverse dispersivity	5 m
Fractures		
	Number of fractures	3
	Discrete fractures	yes
	Porosity	0.05
	Permeability	10000 mD
	Total Compressibility	1e-10 1/Pa
Matrix		
	Porosity	0.001
	Permeability	0.2 mD
	Total Compressibility	1e-11 1/Pa

1.5.1 Parametric Kernel Estimation Examples

Two examples of parametric kernel estimation are illustrated in Sections 1.5.1.1 and 1.5.1.2. The examples are based on simulated data from Reservoir Model I. The first example is for a scenario where the flow rates are constant but the injected tracer concentration varies over time. The second example is from a scenario where the flow rates vary over time, but the injected concentration increases linearly over time, thus producing a signal in the produced concentration that can be used to infer the tracer kernels.

1.5.1.1 Constant Flow – Varying Concentration Example

In the constant flow – varying concentration example for Model I, the injection rates into each of the injectors was set to 2500 m^3 , and the production rates were obtained from a constant bottomhole pressure condition. An estimate of the interwell connectivity (IWC) matrix, F , was found from a varying flow rate simulation that had been run previously. The IWCs used in this case were computed from the M-ARX method (Lee et al., 2010). The estimates are given in Table 1.2.

Table 1.2: Interwell connectivity as determined by the M-ARX method (Lee et al., 2010) for Reservoir Model II.

IWC	I1	I2
P1	0.5480	0.0038
P2	0.4497	0.9904

The concentration of the injected tracer was varied, resulting in the transient production concentrations shown in Figure 1.5. A small amount of Gaussian noise was added to the production data.

The parametric kernel estimation algorithm usually yielded a result for this problem in approximately five minutes, depending on the progress of the genetic algorithm. The fitted data is compared to the actual data set for each producer in Figure 1.6.

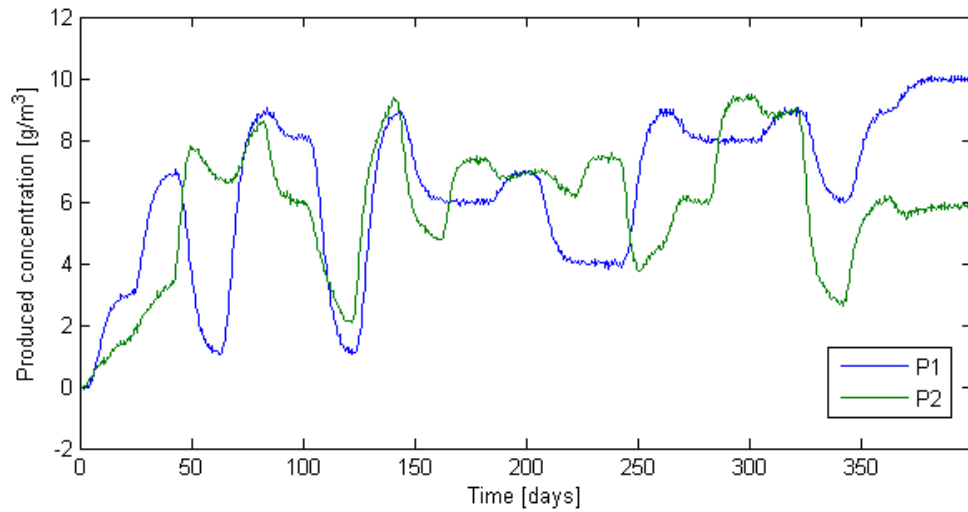
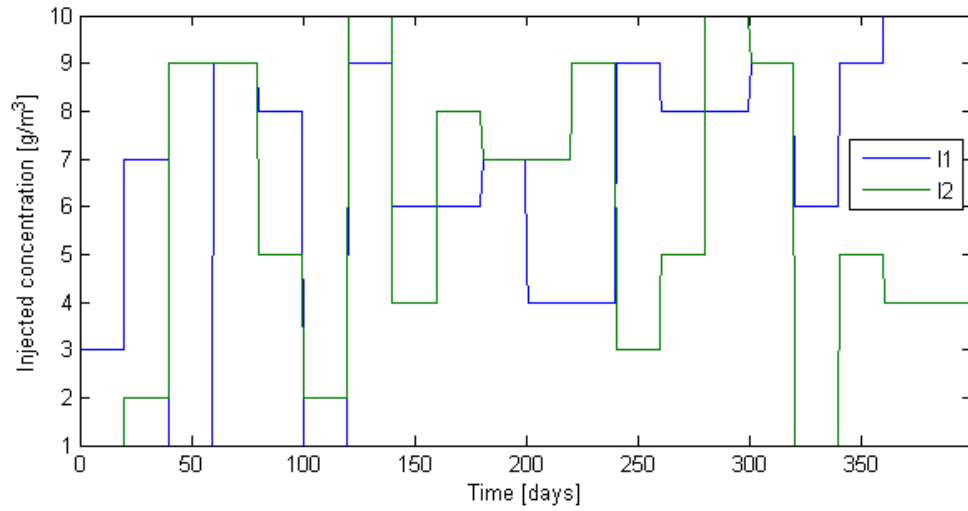


Figure 1.5: Injection and production history of tracer concentration in the constant flow – varying concentration example for Reservoir Model I.

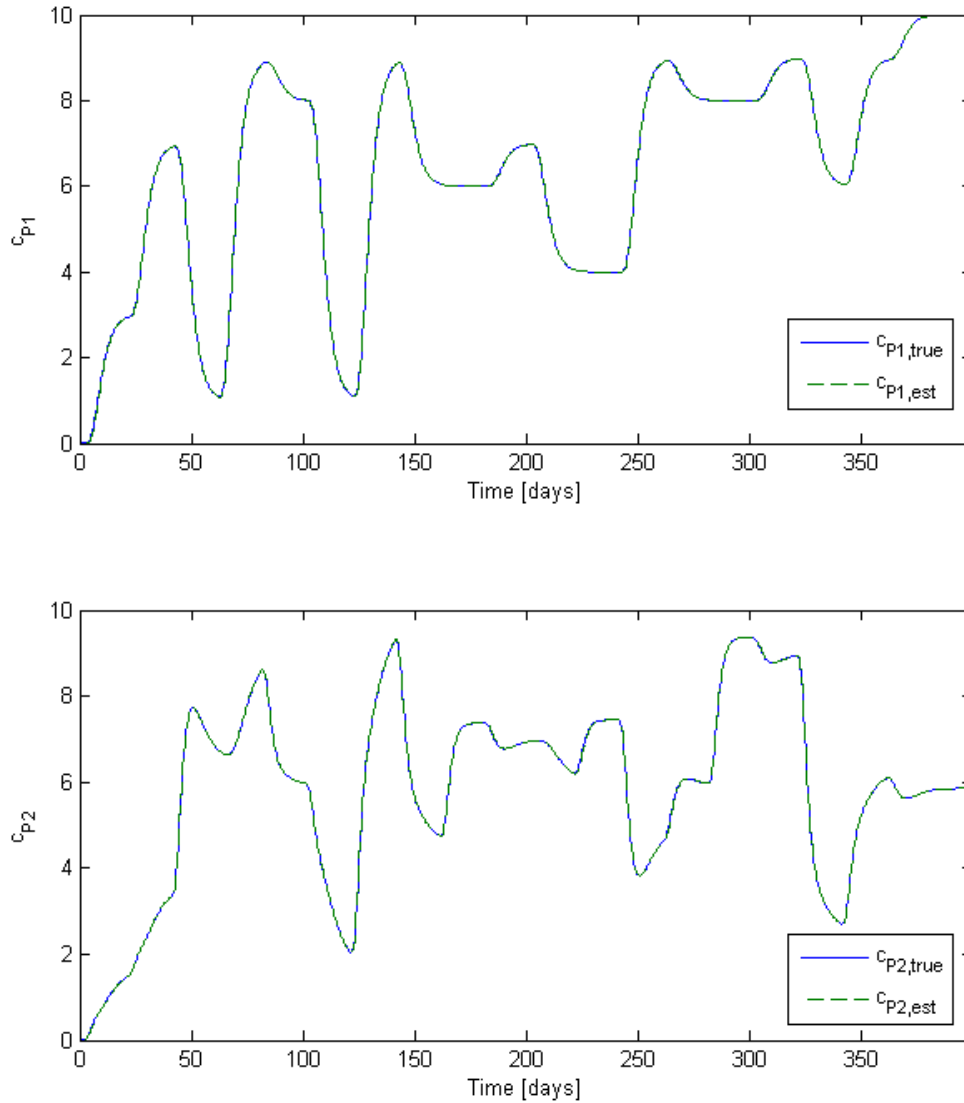


Figure 1.6: Tracer production data as reproduced from the parametric kernel estimates compared to the actual data used to calibrate the models. The true data are shown as blue solid lines and the reproduced data are given by green dashed lines.

The best estimate that the algorithm yielded for each of the four kernels is shown in Figure 1.7, along with the "true" kernels which were obtained by simulating a unit step injection test with the same numerical reservoir model. The figure shows that three of the four kernels were reproduced fairly accurately. These were the kernels which influenced the production signal the most. These results could have been anticipated by looking at the reservoir model. In practice such information would of course be unavailable. Importantly, however, a look at the IWCs would have indicated the same result.

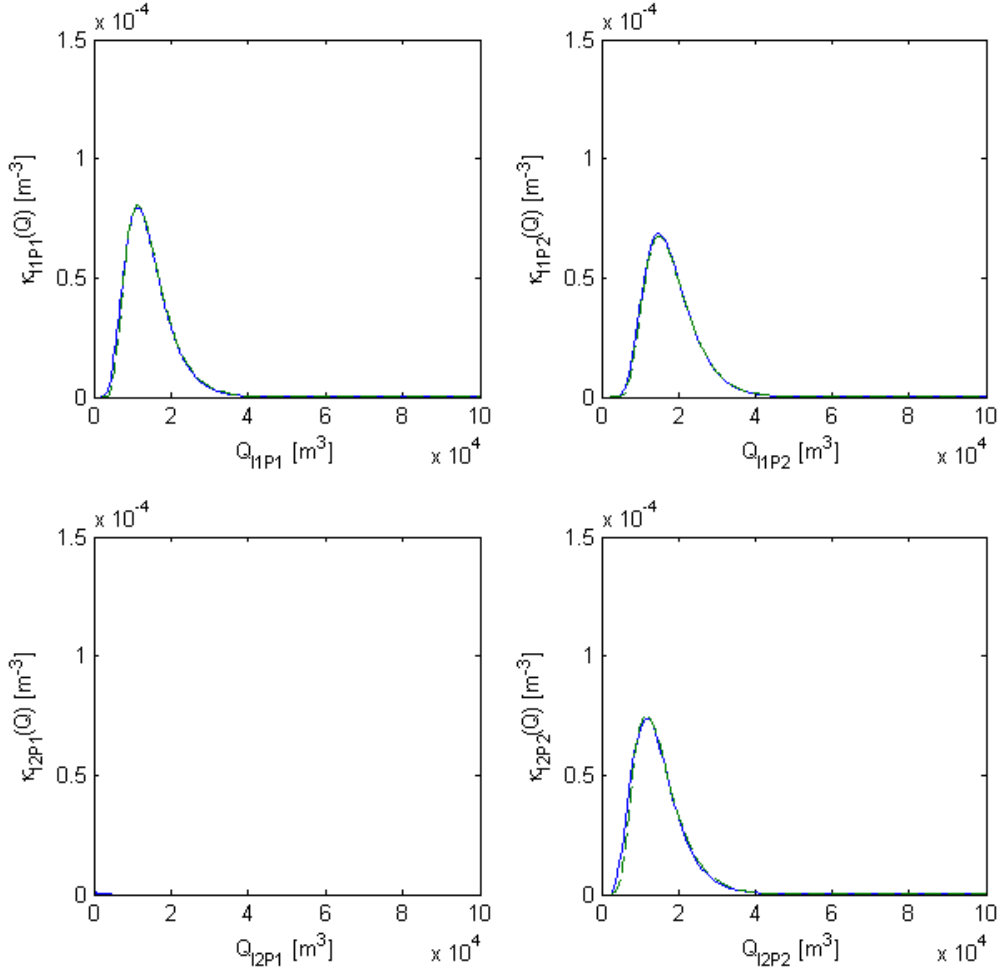


Figure 1.7: Parametric kernel estimates for each of the four injector-producer connections in Reservoir Model I. The "true" kernels are shown as blue solid lines and the parametric estimates are given by green dashed lines.

Another way to determine the significance of each kernel in the model would be to look at the test statistic S_0 , given by Equation (2.15). Similar results were obtained, as listed in Table 1.3. Note that S_0 should be between zero and one, and the closer S_0 is to one, the more significant the influence.

Table 1.3: Test statistic to determine the influence of each kernel in the constant flow rate - varying concentration example for Model I.

S_0	I1	I2
P1	1.0E+00	8.0E-25
P2	3.2E-01	6.8E-01

Assuming that only those kernels should be considered that contribute more than 1% to S_0 , for each production signal, one can construct the boolean influence matrix given in Table 1.4. This table indicates, essentially, which wells are connected and which are not.

Table 1.4: List of valid injector-producer connections based on the test statistic S_0 for Model I.

G0	I1	I2
P1	TRUE	FALSE
P2	TRUE	TRUE

1.5.1.2 Varying Flow – Ramp Concentration Example

The second parametric estimation example given for Model I was based on a data set where the injection and production rates in the reservoir were varied, while the injected tracer concentration grew linearly. Therefore this data set resembled more the data from the Palinpinon field mentioned earlier. The injection and production rates are shown in Figure 1.8.

The changes in flow rate led to variations in tracer arrival time as shown in Figure 1.9. Only the data from the first 350 days was used to estimate the kernels. An additional transient was provided by dropping the concentration to zero at after 350 days, so as to show that a sudden change in concentration could be predicted with the model.

The modeled data is compared to the produced data in Figure 1.10. The time factor for the mixing weight (T in Equation (2.2)) needed a bit of manual tuning to get the model to show such excellent agreement with the data.

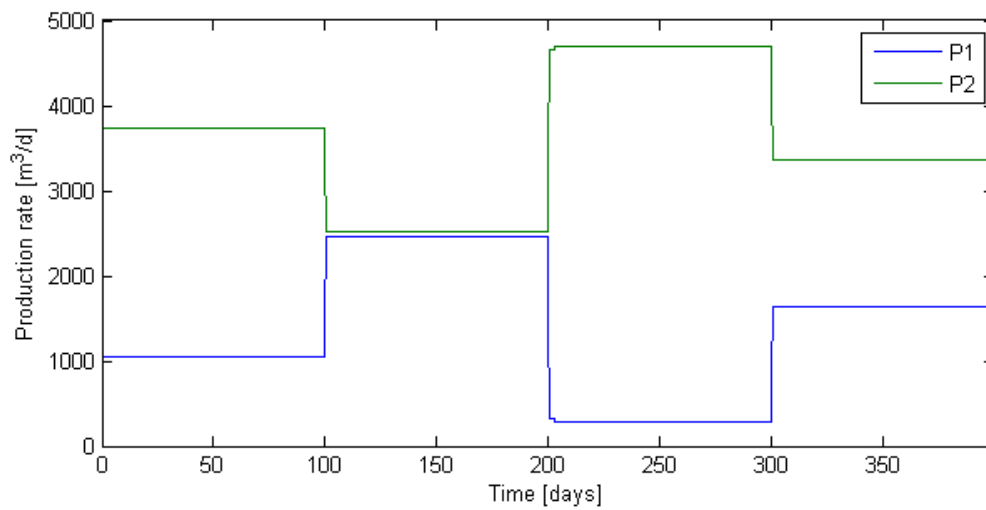
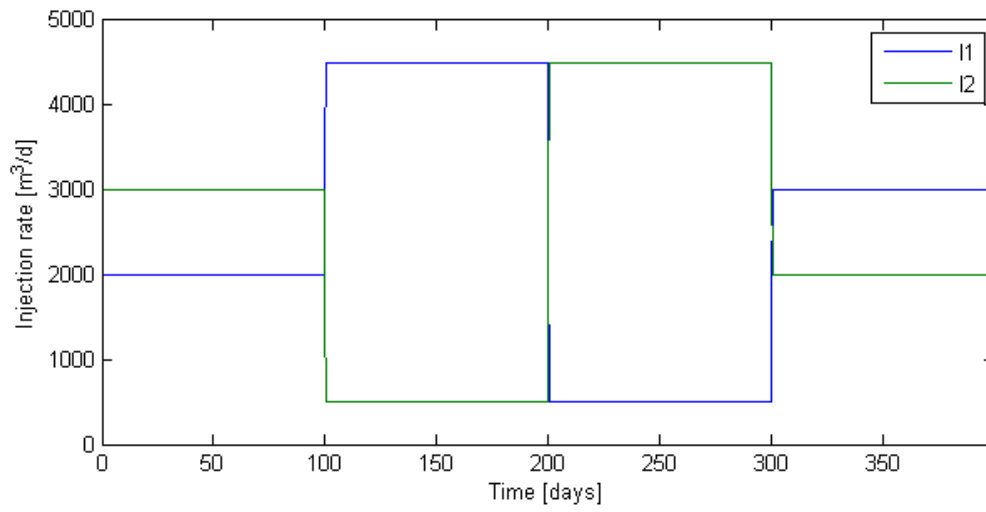


Figure 1.8: Injection and production rates in the variable flow rate - ramp tracer example for Reservoir Model I.

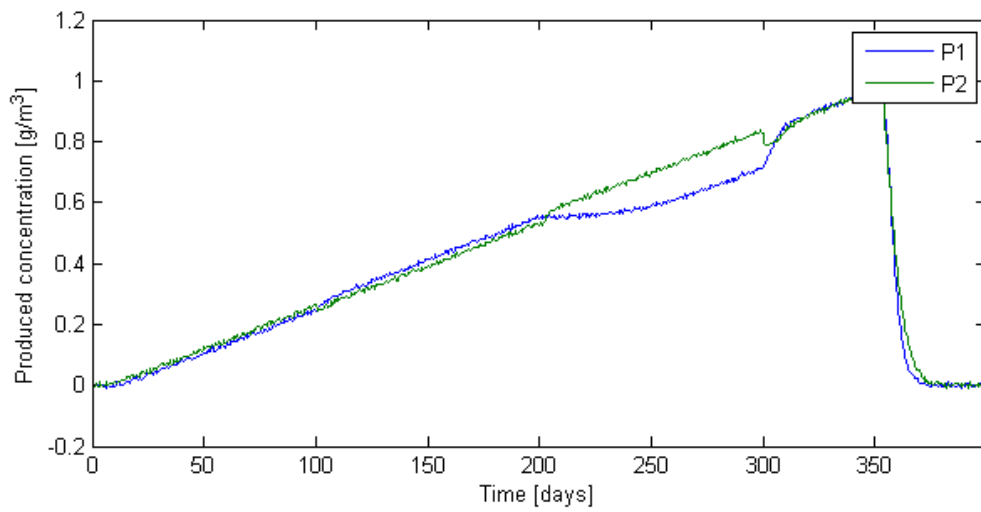
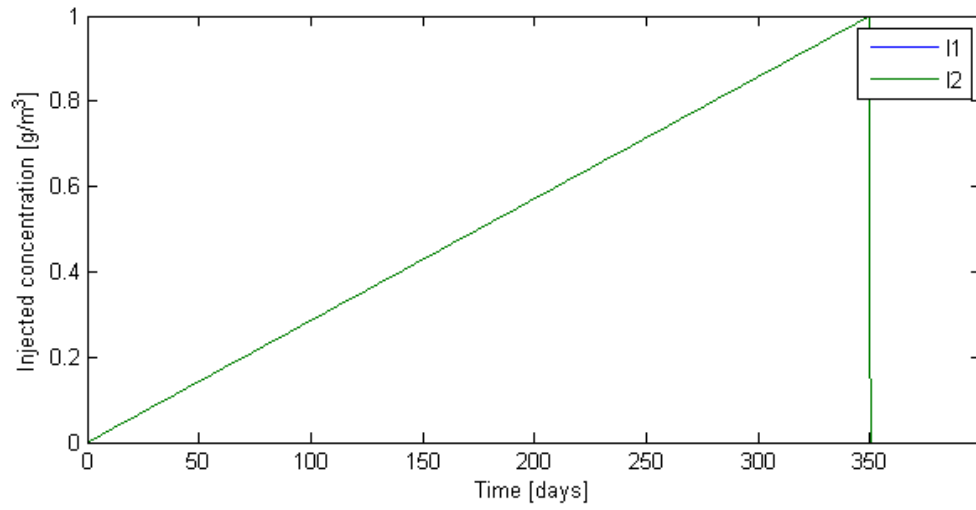


Figure 1.9: Injection and production history of tracer concentration in the variable flow rate – ramp concentration example for Reservoir Model I.

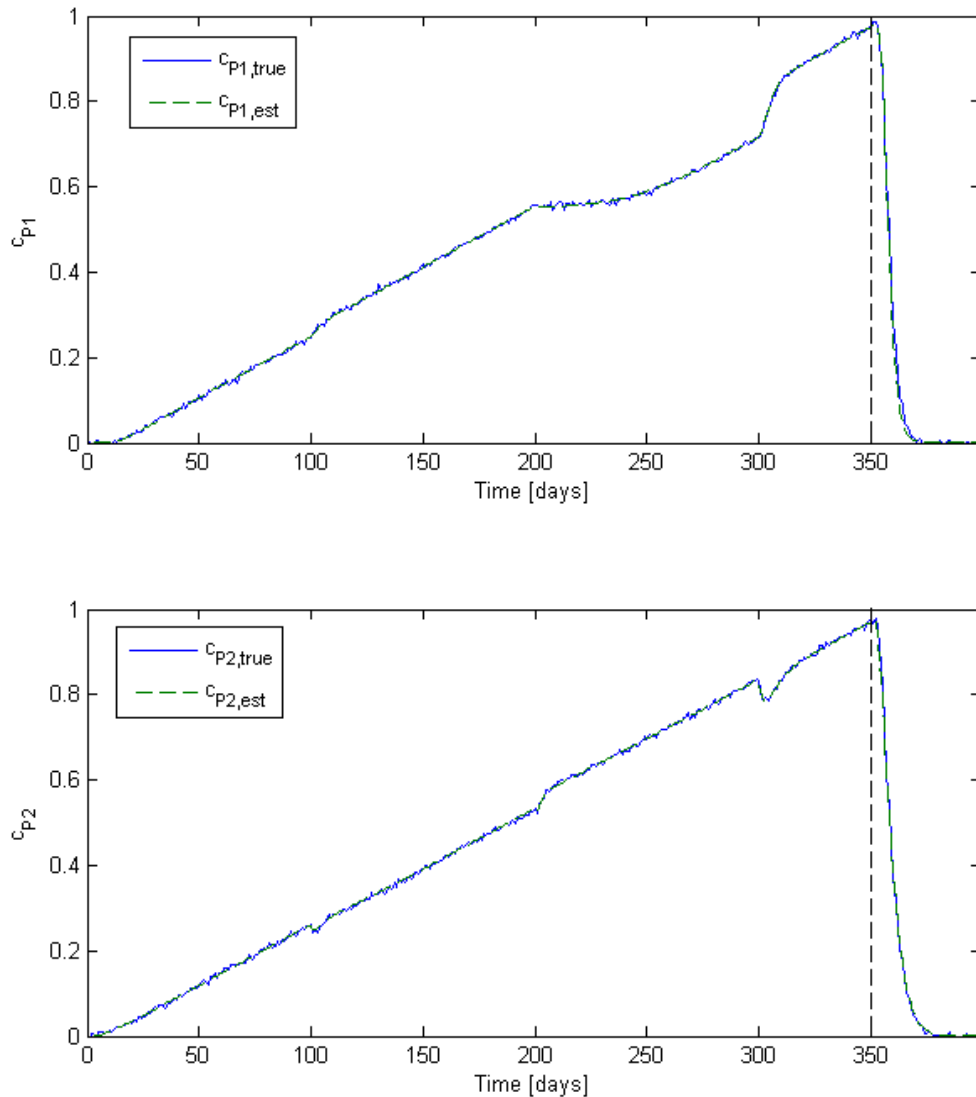


Figure 1.10: Model reproduction of the tracer production data in the variable flow rate - ramp tracer example for Reservoir Model I. The true data are shown as blue solid lines and the reproduced data are given by green dashed lines. The black dashed line divides the estimation and prediction periods.

The tracer kernels were reproduced quite accurately in this case as well, as shown in Figure 1.11.

And finally, the test statistic S_0 indicated as before that all wells were well connected other than I2 and P1, as can be inferred from Table 1.5.

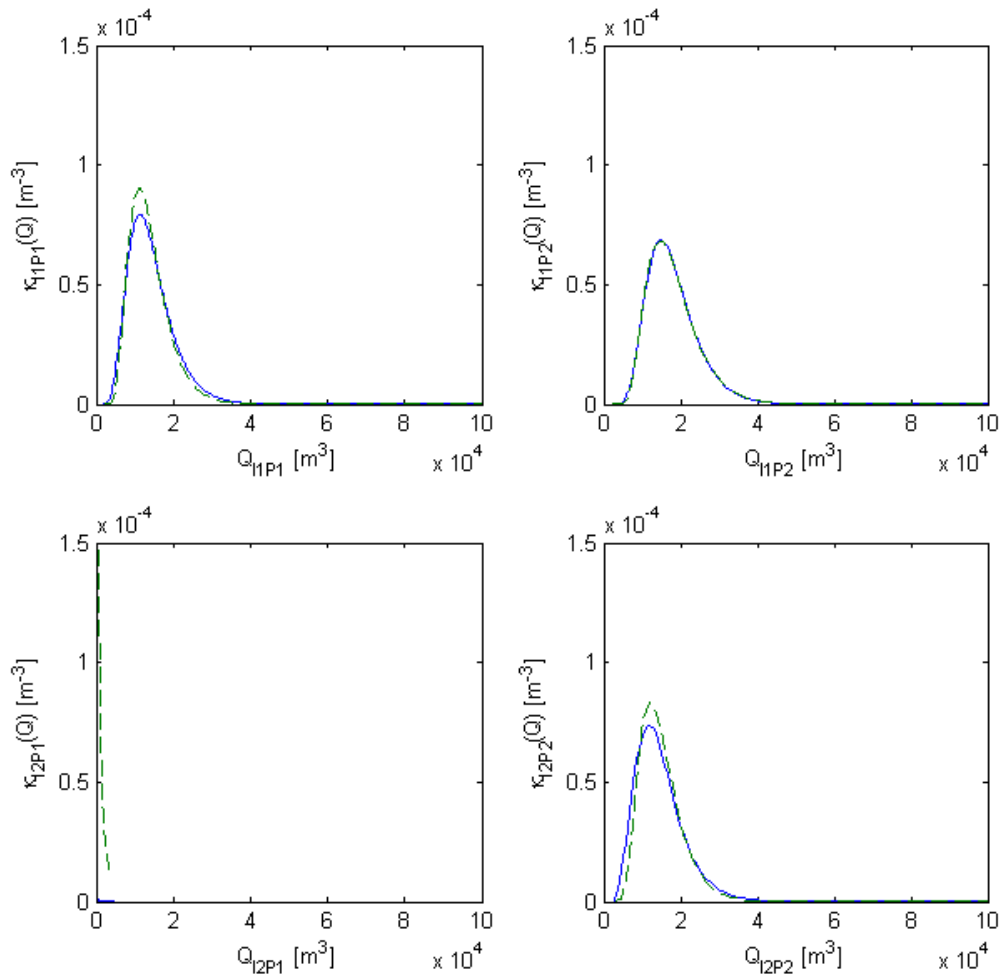


Figure 1.11: Parametric kernel estimates for each of the four injector-producer connections in Reservoir Model I. The "true" kernels for the 2500 m³/day case are plotted with blue solid lines. The parametric estimates are given by green dashed lines.

Table 1.5: Test statistic to determine the influence of each kernel in the varying flow rate – ramp concentration example for Model I.

S0	I1	I2
P1	1.0E+00	1.0E-04
P2	2.6E-01	7.4E-01

1.5.2 Nonparametric Kernel Estimation Examples

The scenarios described in Section 1.5.1 were also modeled using a nonparametric approach. The results are described in the following two sections.

1.5.2.1 Constant Flow – Varying Concentration Example

Figure 1.5 shows injection and production history that was used again to estimate the tracer kernels, but this time with a nonparametric model. The kernels that were included in the nonparametric estimation problem were only those that were deemed significant after parametric estimation.

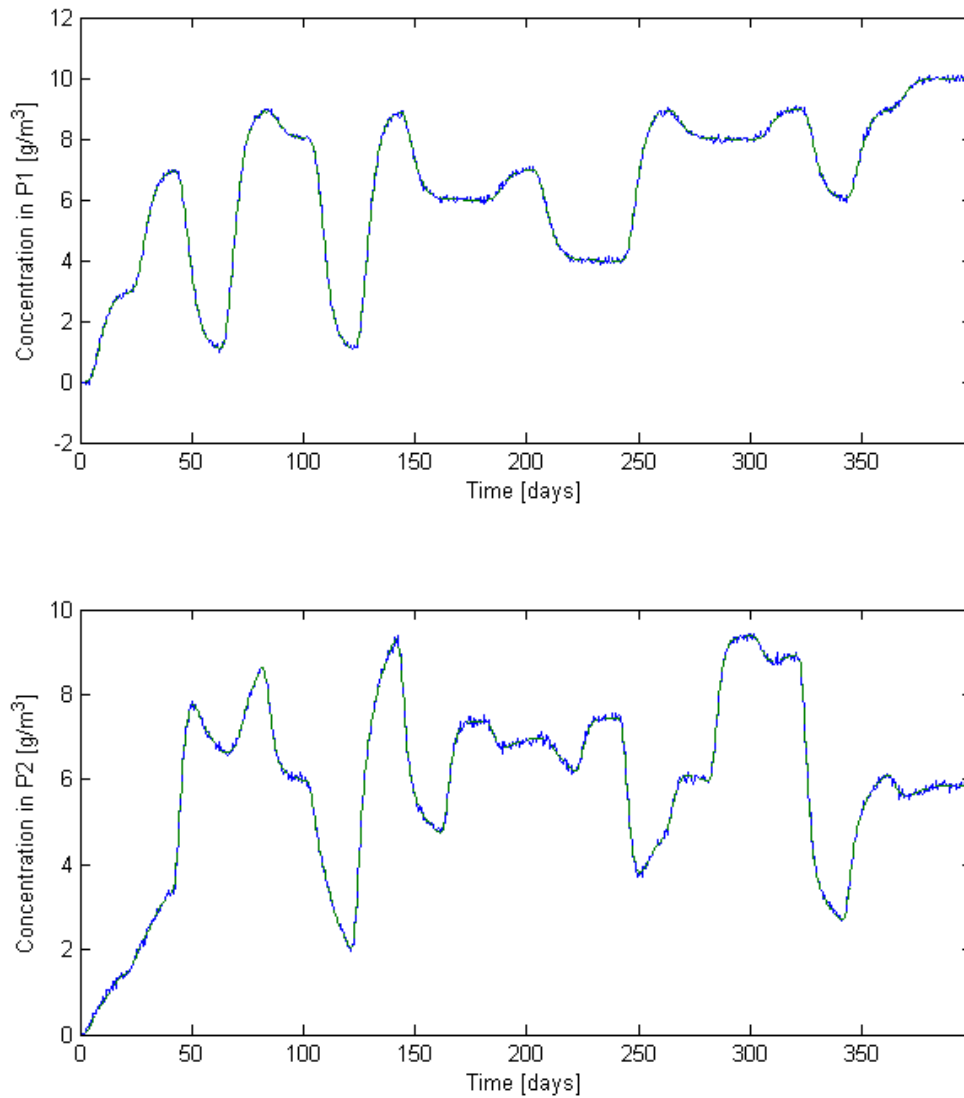


Figure 1.12: Fit to the production data from the constant flow - varying concentration example for Reservoir Model I, using nonparametric kernels.

The parametric kernels estimated in Section 1.5.1.1 were used prior to assist in constraining the shape of the nonparametric kernel estimates. This was an important

addition to the method, as it both provided a reasonable discretization scheme and made it easier to capture important transients in the kernels. For this particular model, however, the parametric kernels were able to describe the actual kernels very well. The resulting data fit is shown in Figure 1.12.

The MATLAB algorithm *fmincon* was used to solve the problem, with the trust-region-reflective algorithm.

The weighting parameter for the regularization term, θ , was set to a relatively large number (10^6) to enforce smoothness in the kernel estimates, which are shown in Figure 1.13.

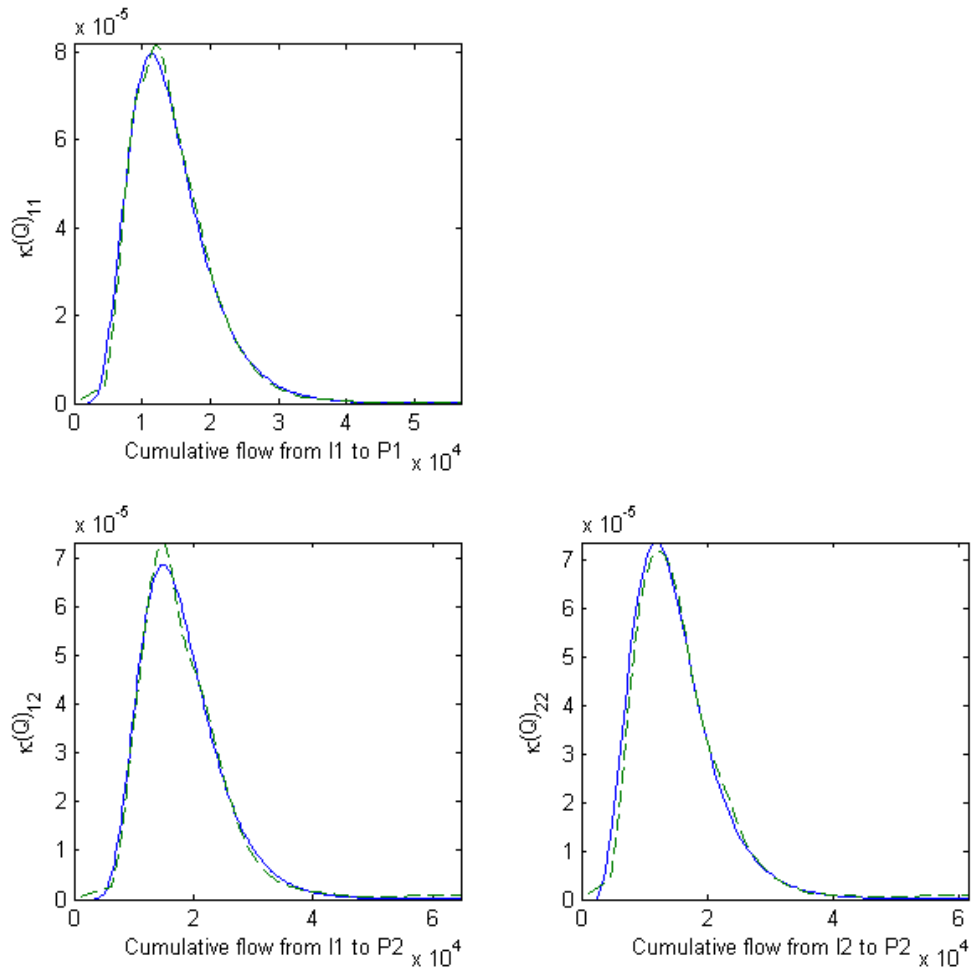


Figure 1.13: Nonparametric kernel estimates for those kernels deemed significant in the constant flow - varying tracer example for Reservoir Model I. The "true" kernels are given by blue solid lines while the estimates are in green dashed lines.

The bootstrap method was used to assess the uncertainty in the kernel estimates. The results are shown in Figure 1.14. Some parts of the actual kernels fell outside of the 95%

confidence interval. The reason for how poorly the early parts of the kernels were captured was that there were not many discretization points there.

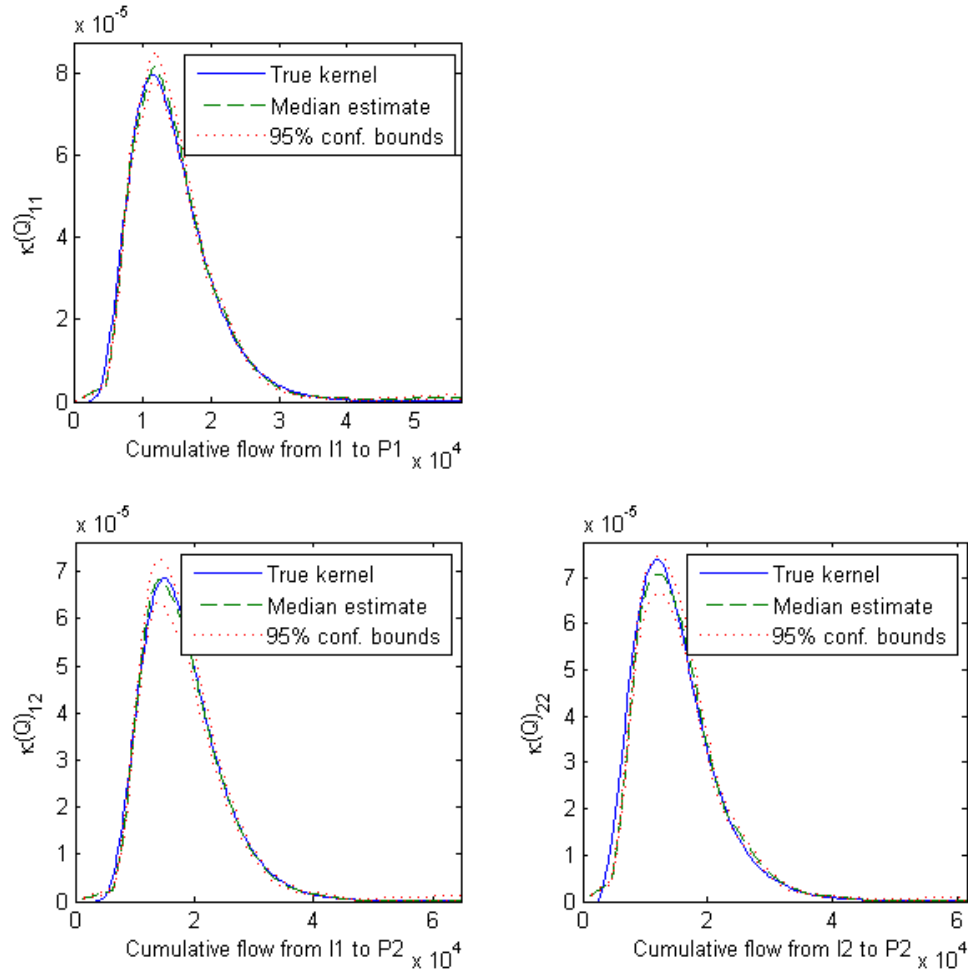


Figure 1.14: Nonparametric kernel estimates and 95% confidence bounds obtained from parametric bootstrapping for those kernels deemed significant in the constant flow - varying tracer example for Reservoir Model I.

1.5.2.2 Varying Flow – Ramp Concentration Example

The final example based on the data from Model I was to obtain a nonparametric kernel estimate with the varying flow – ramp concentration production data shown in Figure 1.8 and Figure 1.9.

Again the time scale for the mixing weights, T in Equation (2.2), needed to be tuned manually to achieve a good fit. Otherwise the problem was solved by a straightforward application of the nonparametric estimation method. The resulting data fit is shown in Figure 1.15, where data from the first 350 days was used to calibrate the kernels, and the

rest of the data was predicted based on the kernel estimates. This verification method for the model is known as cross-validation.

The estimated kernels with uncertainty bounds obtained from bootstrapping are illustrated in Figure 1.16. The estimated kernel for the IIP1 connection turned out to be a bit less dispersive than the actual kernel. The reason for this was probably that the time scale for the mixing weights needed to be relatively large get a good fit. The large time scale acted as a smoother on the response, thus incentivizing a slightly less dispersive kernel estimate.

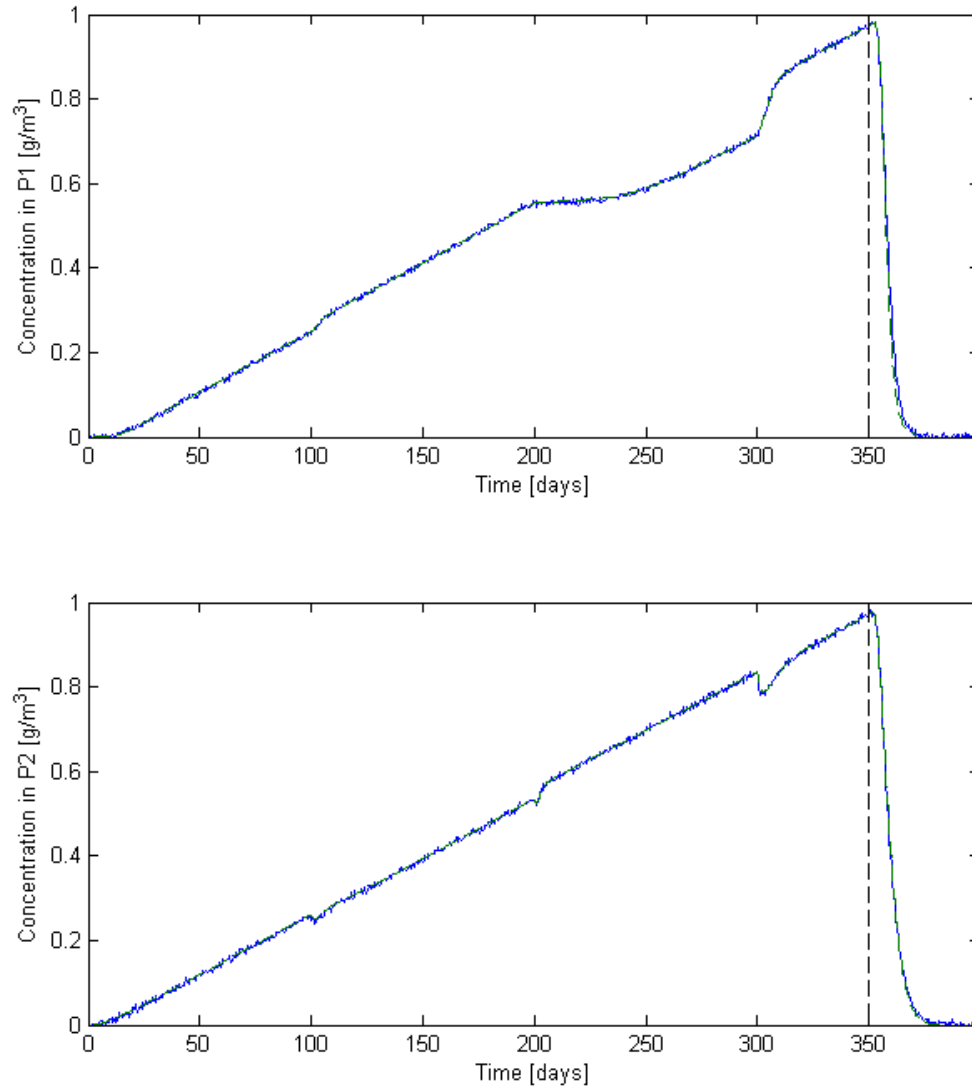


Figure 1.15: Fit to the production data from the varying flow - ramp concentration example for Reservoir Model I, using nonparametric kernels.

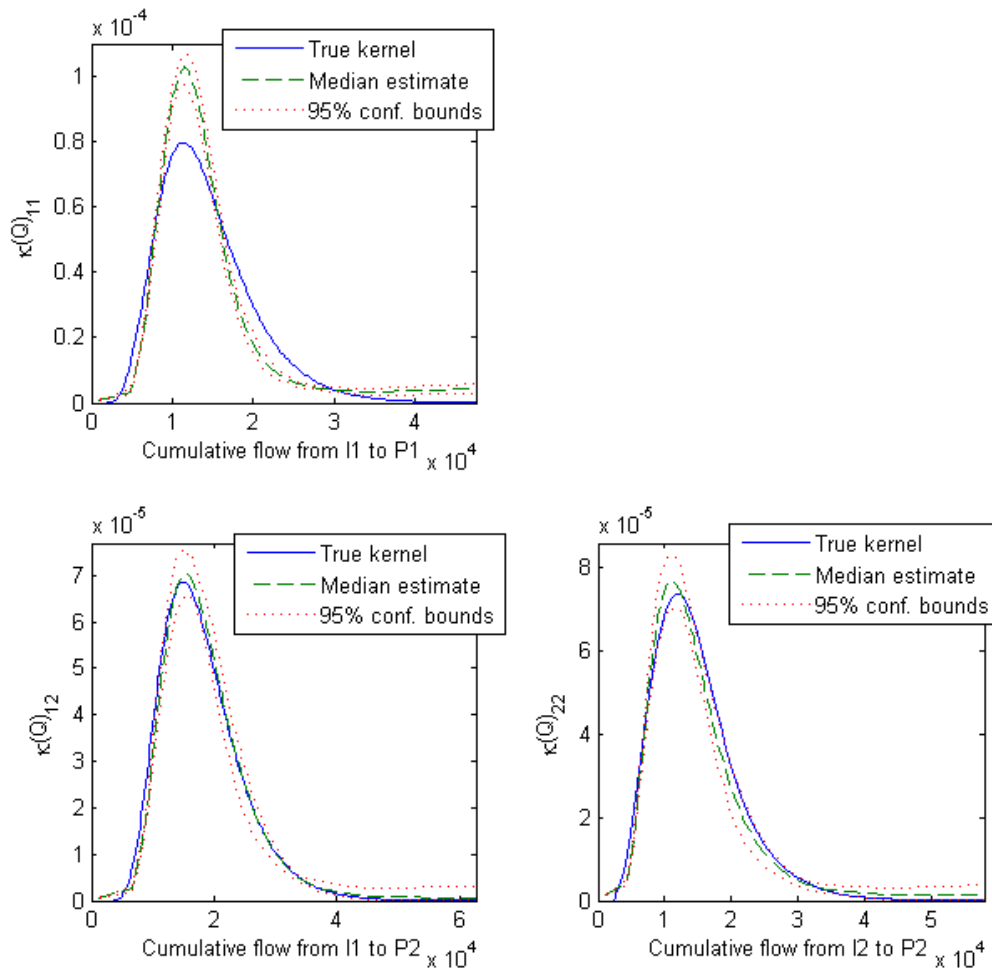


Figure 1.16: Nonparametric kernel estimates and 95% confidence bounds obtained from parametric bootstrapping for those kernels deemed significant in the varying flow - ramp concentration example for Reservoir Model I.

1.6 KERNEL ESTIMATION WITH A LARGE RESERVOIR MODEL

The second series of examples was run with a model that was partially based on data from the Soultz-sous-Forêts enhanced geothermal system in France. This will be referred to as Model II. A three-dimensional map of fractures was obtained from Place et al. (2011). The fractures were imported into the discrete fracture generation software FRACMAN. Additional fractures were generated based on data from Massart et al. (2010), and then a two-dimensional slice, $3000 \times 1000 \text{ m}^2$, of fracture traces was extracted from a region of interest (Figure 1.17).

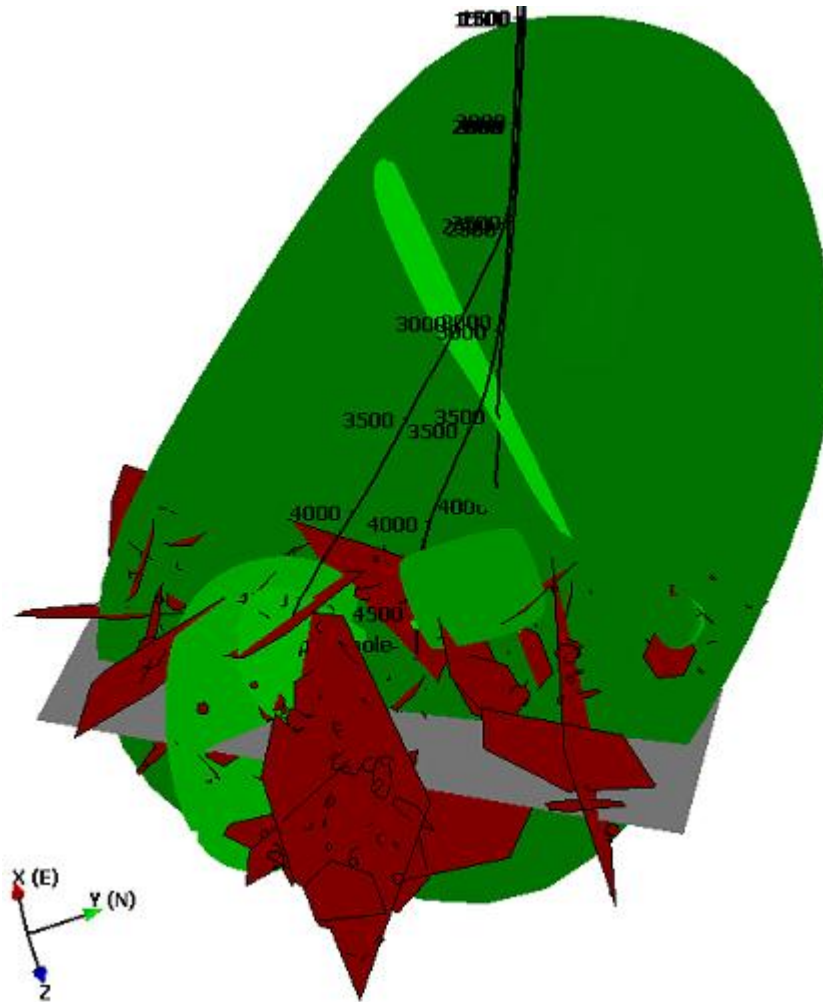


Figure 1.17: A three dimensional fracture network upon which Model II is based. The green fractures were generated obtained from Place et al. (2011). The maroon fractures were added in FRACMAN using data from Massart et al. (2010). A two-dimensional slice of interest is shown in gray.

The fracture trace map was used to outline discrete fractures in FEFLOW. Figure 1.18 shows the layout of fractures and the computational grid generated for the FEFLOW model. The grid was generated with the Triangle (Shewchuk, 1996) gridding software. This grid had 41473 elements and 20841 nodes. The shortest fracture element was approximately 4 m.

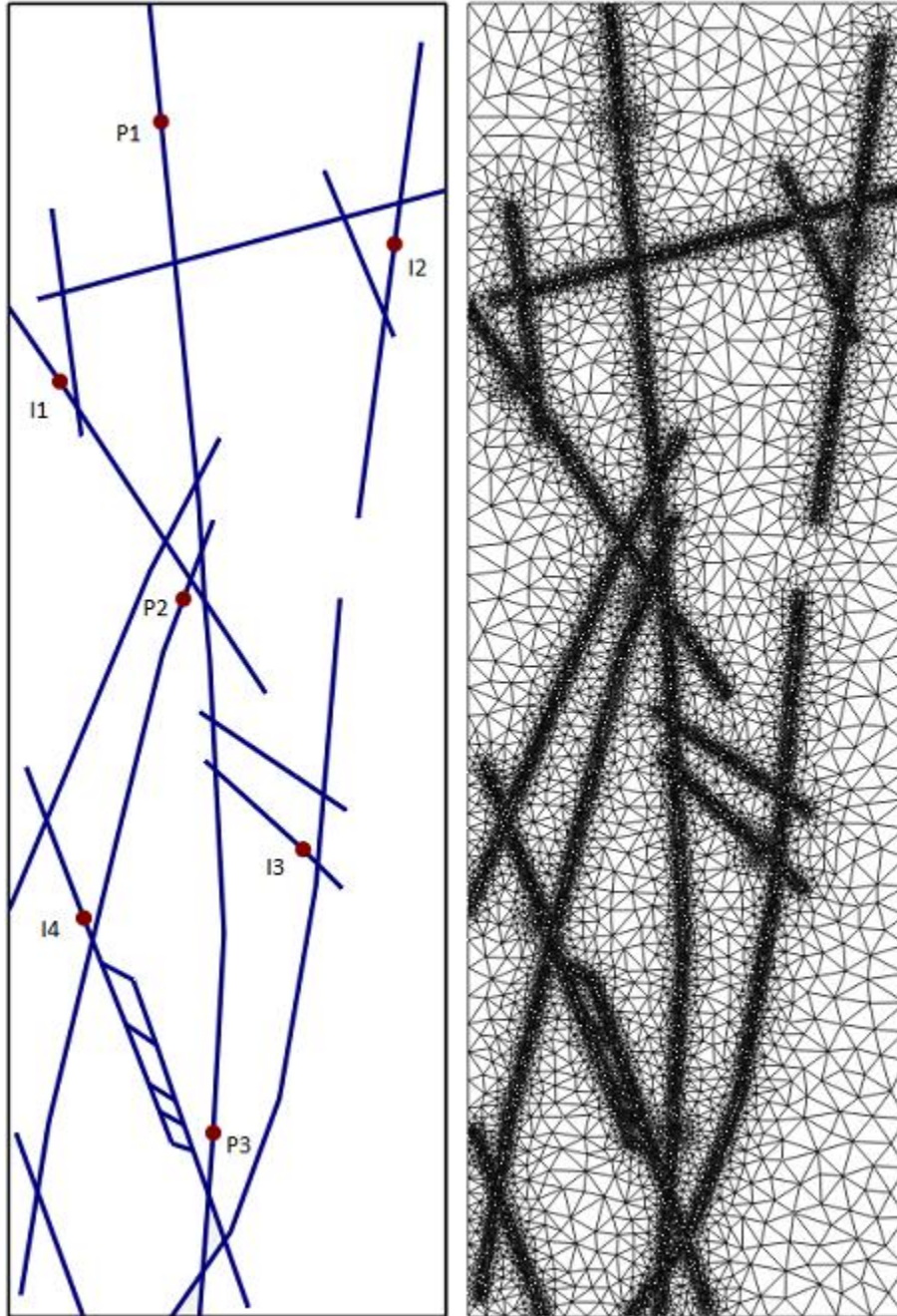


Figure 1.18: The layout of fractures and the computational grid used for Model II.

Table 1.6 summarizes the main properties of Model II. A more detailed recounting of the properties of Model II is given in Juliusson and Horne (2011).

Table 1.6: Summary of properties for Reservoir Model II.

General		
	Dimensions	3000 x 1000 x 500 m ³
	Initial temperature	150 C
	Rock heat capacity	2520 kJ/m ³ /C
	Rock heat conductivity	3 J/m/s/C
	Longitudinal dispersivity	50 m
	Transverse dispersivity	5 m
Fractures		
	Number of fractures	19
	Discrete fractures	yes
	Porosity	0.04
	Permeability	$\alpha L^{1.87}$ mD
	Total Compressibility	1e-10 1/Pa
Matrix		
	Porosity	0.001
	Permeability	0.01 mD
	Total Compressibility	1e-11 1/Pa

1.6.1 Parametric Kernel Estimation Examples

Two examples of parametric kernel estimation are illustrated in Sections 1.6.1.1 and 1.6.1.2. The examples are based on data obtained from Reservoir Model II. First example is for a scenario where the flow rates are constant but the injected tracer concentration varies over time. The second example is from a scenario where the flow rates vary over time, but the injected concentration increases linearly over time, thus producing a signal in the produced concentration that can be used to infer the tracer kernels.

1.6.1.1 Constant Flow – Varying Concentration Example

In the constant flow – varying concentration example, the injection rates into each of the four injectors was set to 3000 m³, and the production rates were obtained from a constant bottomhole pressure condition. It was assumed that an estimate of the interwell connectivity (IWC) matrix, F , was available. Such an estimate could have been obtained by one of the pressure and/or flow rate methods discussed in the Annual Report for 2010 – 2011. The IWCs used in this case were those given in Table 1.7. The concentration of the injected tracer was varied. The injection and production concentrations are shown in Figure 1.19. A small amount of Gaussian noise was added to the production data.

The parametric kernel estimation algorithm usually yielded a result for this problem within half an hour, depending on the progress of the Genetic Algorithm. The fitted data is compared to the actual data set for each producer in Figure 1.20.

Table 1.7: Interwell connectivity as determined by the M-ARX method (Lee et al., 2010) for Reservoir Model II.

IWC	I1	I2	I3	I4
P1	0.304	0.7179	0.0487	0.0597
P2	0.5896	0.1981	0.0988	0.8354
P3	0.1179	0.0641	0.8644	0.0964

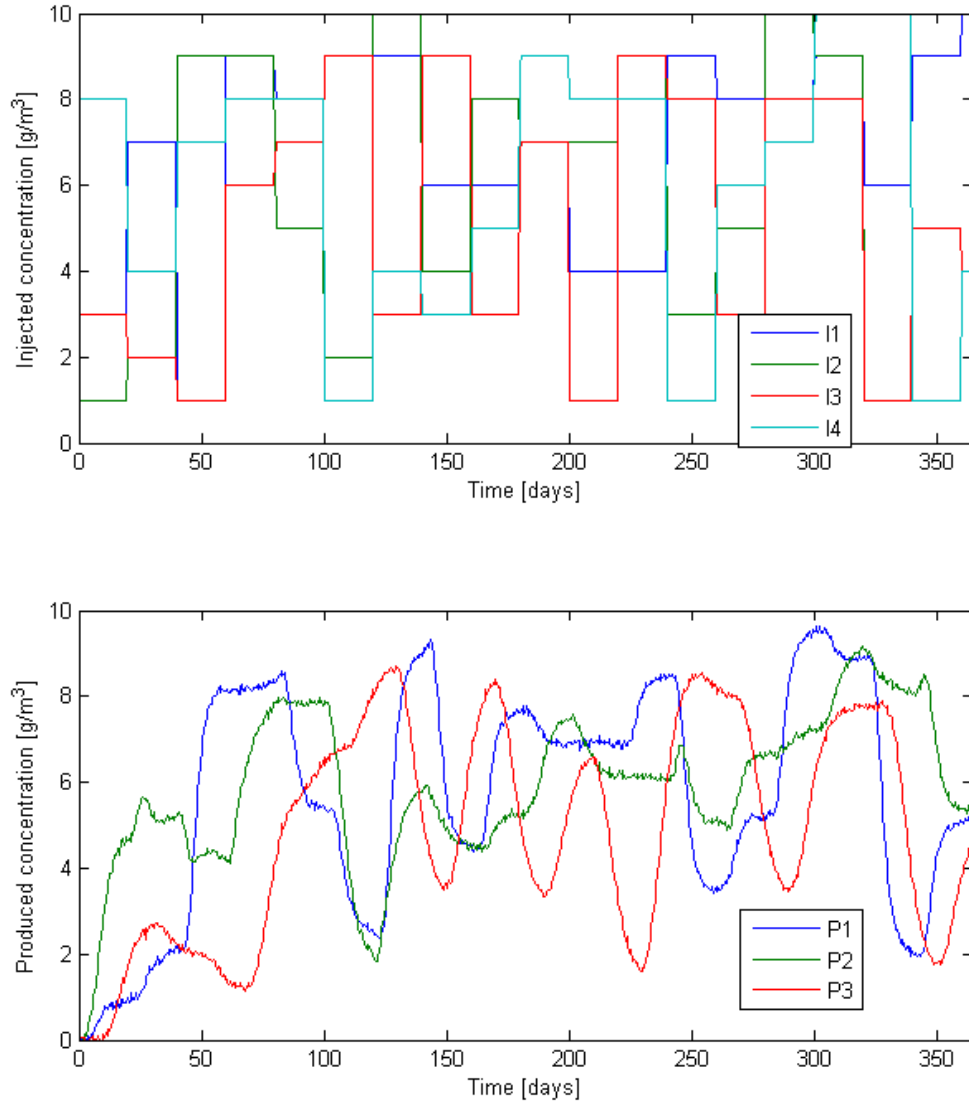


Figure 1.19: Injection and production history of tracer concentration in the constant flow – varying concentration example for Reservoir Model II.

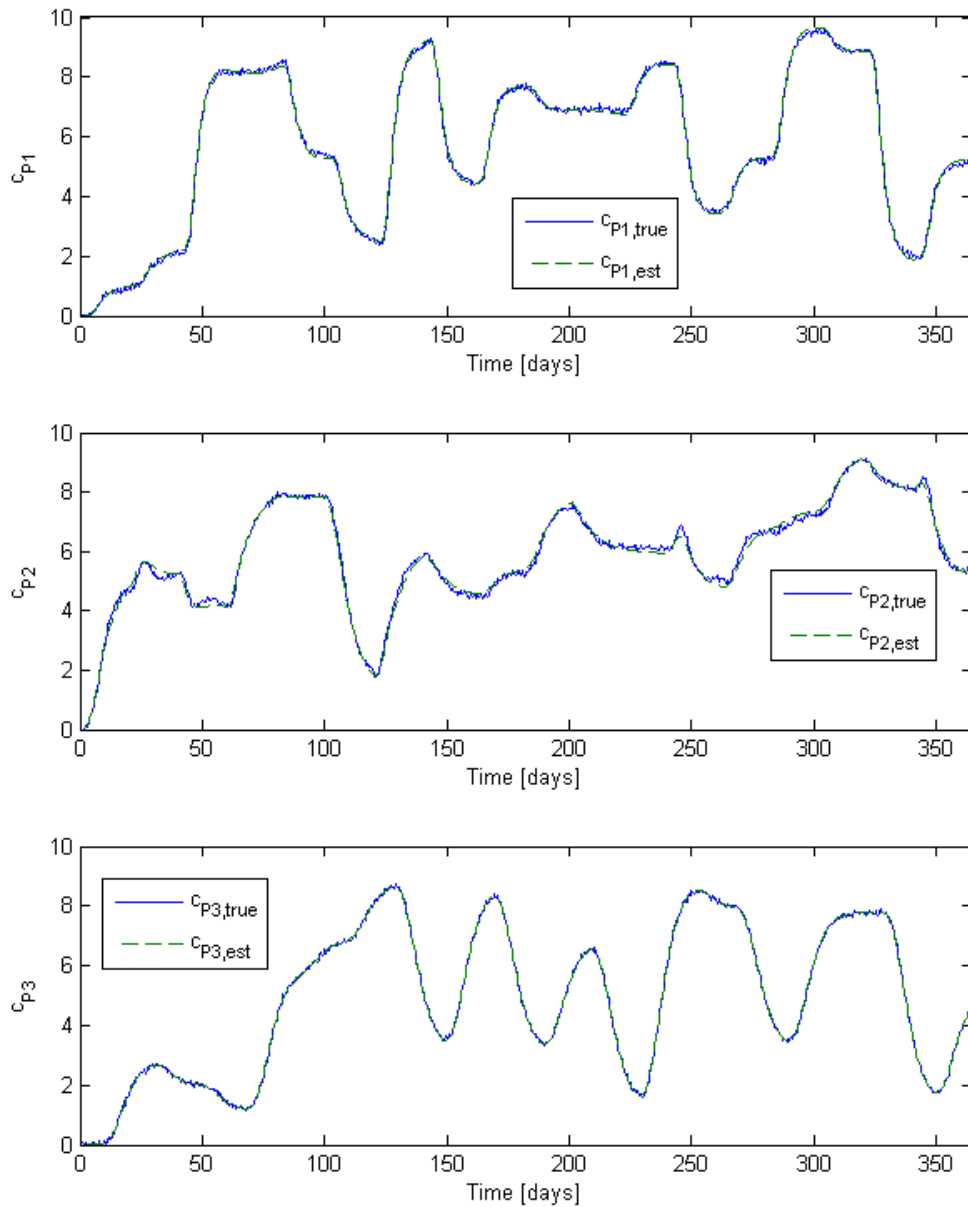


Figure 1.20: Tracer production data as reproduced from the parametric kernel estimates compared to the actual data used to calibrate the models. The true data are shown as blue solid lines and the reproduced data are given by green dashed lines.

The best estimate that the algorithm yielded for each of the twelve kernels is shown in Figure 1.21, along with the "true" kernels which were obtained by simulating a unit step injection test with the same numerical reservoir model. The figure shows that six of the twelve kernels were reproduced fairly accurately. These were the kernels which influenced the production signal the most. These results could have been anticipated by looking at the

IWCs, perhaps with the exception of the I1P3 kernel which seems to have been poorly captured, as compared to the I4P3 kernel which was captured relatively well.

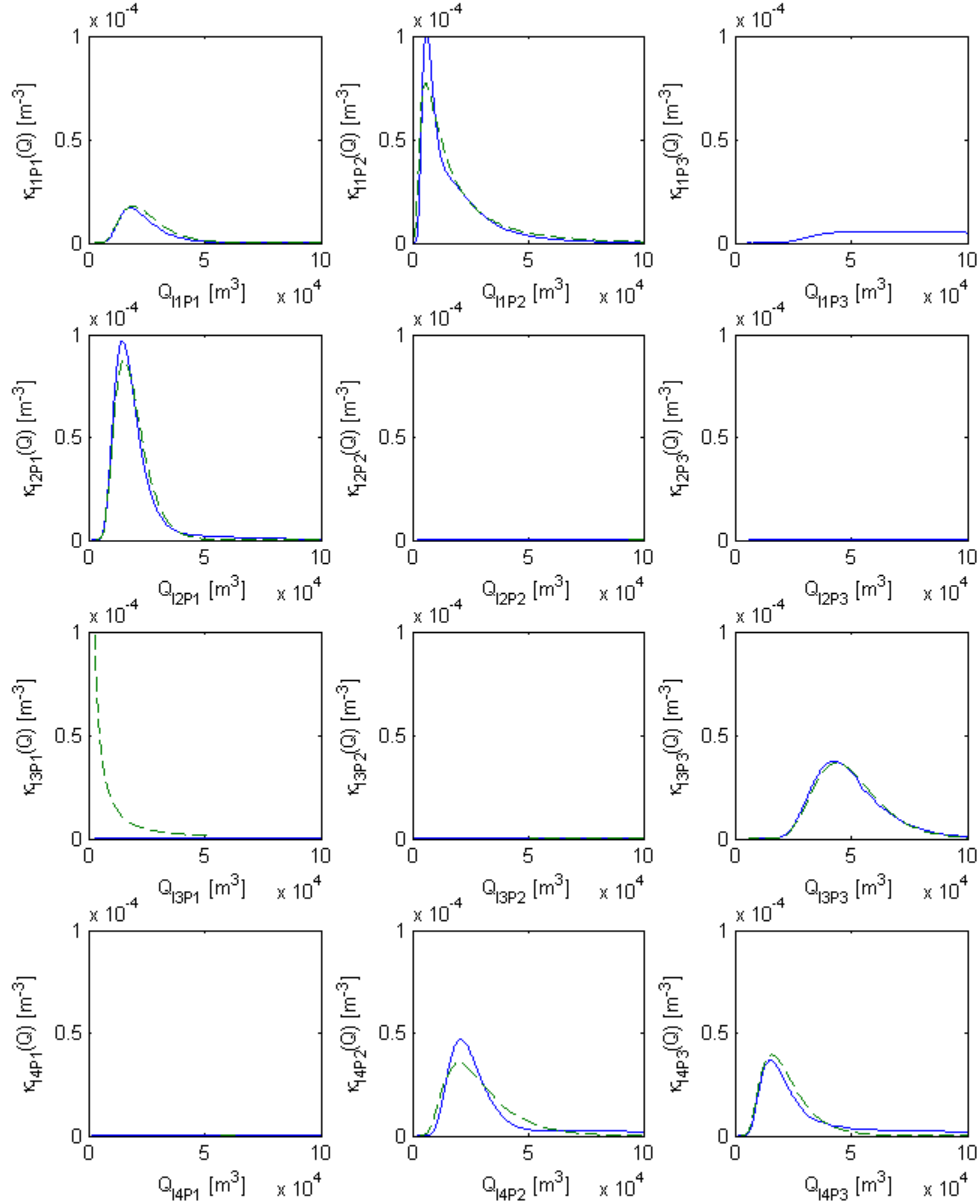


Figure 1.21: Parametric kernel estimates for each of the four injector-producer connections in Reservoir Model II. The "true" kernels are shown as blue solid lines and the parametric estimates are given by green dashed lines.

The test statistic S_0 given by Equation (2.15) was computed to determine the significance that each kernel had on the production signal. The resulting values are listed in Table 1.8.

Table 1.8: Test statistic to determine the influence of each kernel in the constant flow rate - varying concentration example for Model II.

S0	I1	I2	I3	I4
P1	4.7E-02	9.4E-01	9.3E-03	1.0E-20
P2	4.8E-01	1.3E-07	8.1E-13	5.2E-01
P3	1.0E-23	1.0E-35	9.4E-01	6.1E-02

A 0.99 threshold on the cumulative influence of the injectors on each producer, gave following boolean matrix (Table 1.9) for whether there was a meaningful connection between wells.

Table 1.9: List of valid injector-producer connections based on the test statistic S0. for Model II.

G0	I1	I2	I3	I4
P1	TRUE	TRUE	FALSE	FALSE
P2	TRUE	FALSE	FALSE	TRUE
P3	FALSE	FALSE	TRUE	TRUE

1.6.1.2 Varying Flow – Ramp Concentration Example

The second parametric estimation example that will be given for Model II was based on a data set where the injection and production rates in the reservoir vary, while the injected tracer concentration grows linearly. The injection and production rates are shown in Figure 1.22.

The changes in flow rate led to variations in tracer arrival time as shown in Figure 1.23. The variations in flow rate were designed to give a unique signal from each injector. Therefore an additional transient was provided by dropping the concentration to zero at after 600 days, although this was part of the data was only used for cross validation.

The modeled data are compared to the produced data in Figure 1.24. In experimenting with various flow configurations it seemed that the model worked well as long as the flow rate from the best connected wells was fairly high. For example, the model could not capture the concentration in producer P1 very well, in the period where the flow rate in injector I2 was very low (days 200-300). This could be because, in these situations, both numerical and molecular diffusion started to affect the signal significantly. The predictive capacity of the model was validated by a fairly accurate match over the cross validation period (days 600-730).

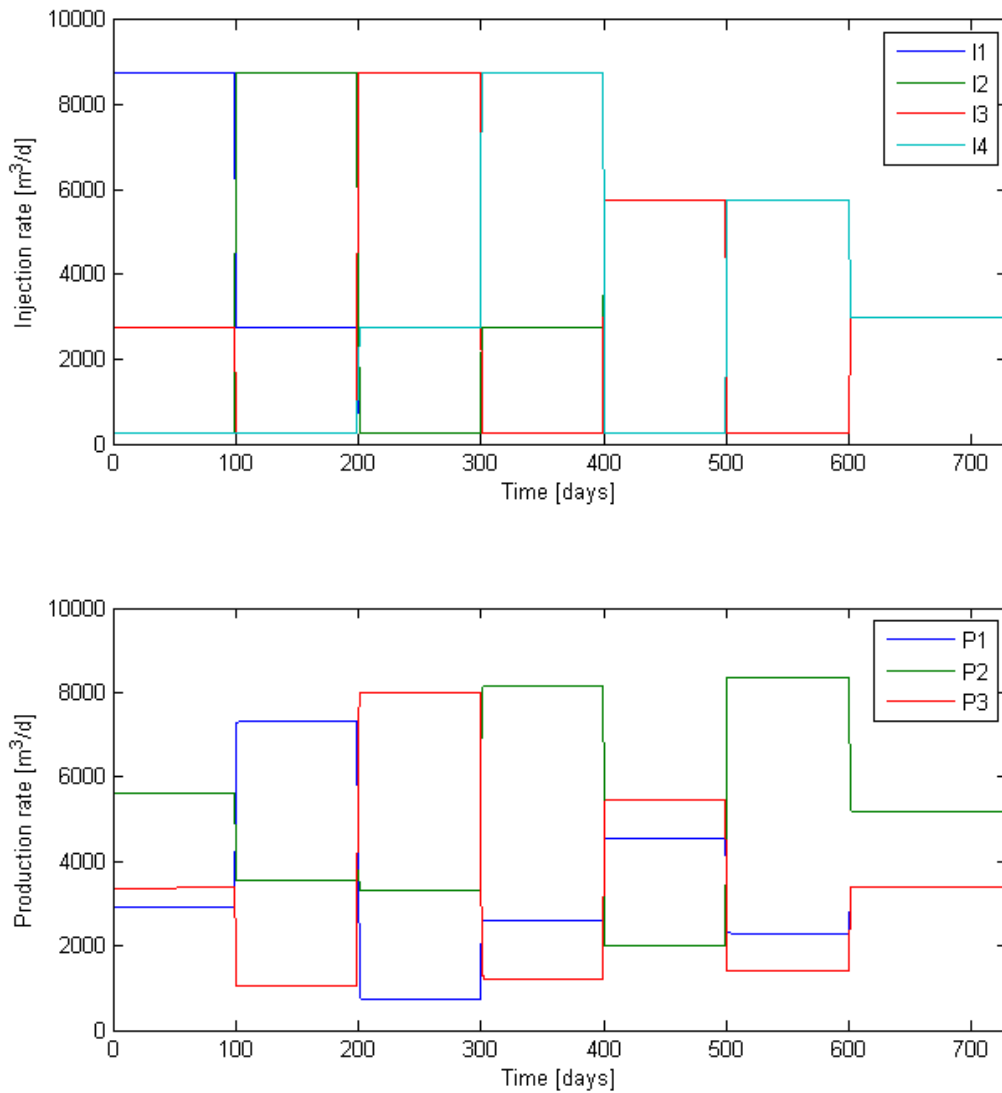


Figure 1.22: Injection and production rates in the variable flow rate - ramp tracer example for Reservoir Model II.

Another reason for parts of the ramp transients being poorly captured was that some of the flow paths between wells were shared and therefore residual tracer from, say, producer A could be pushed by producer B towards a given injector even after producer A had been turned off.

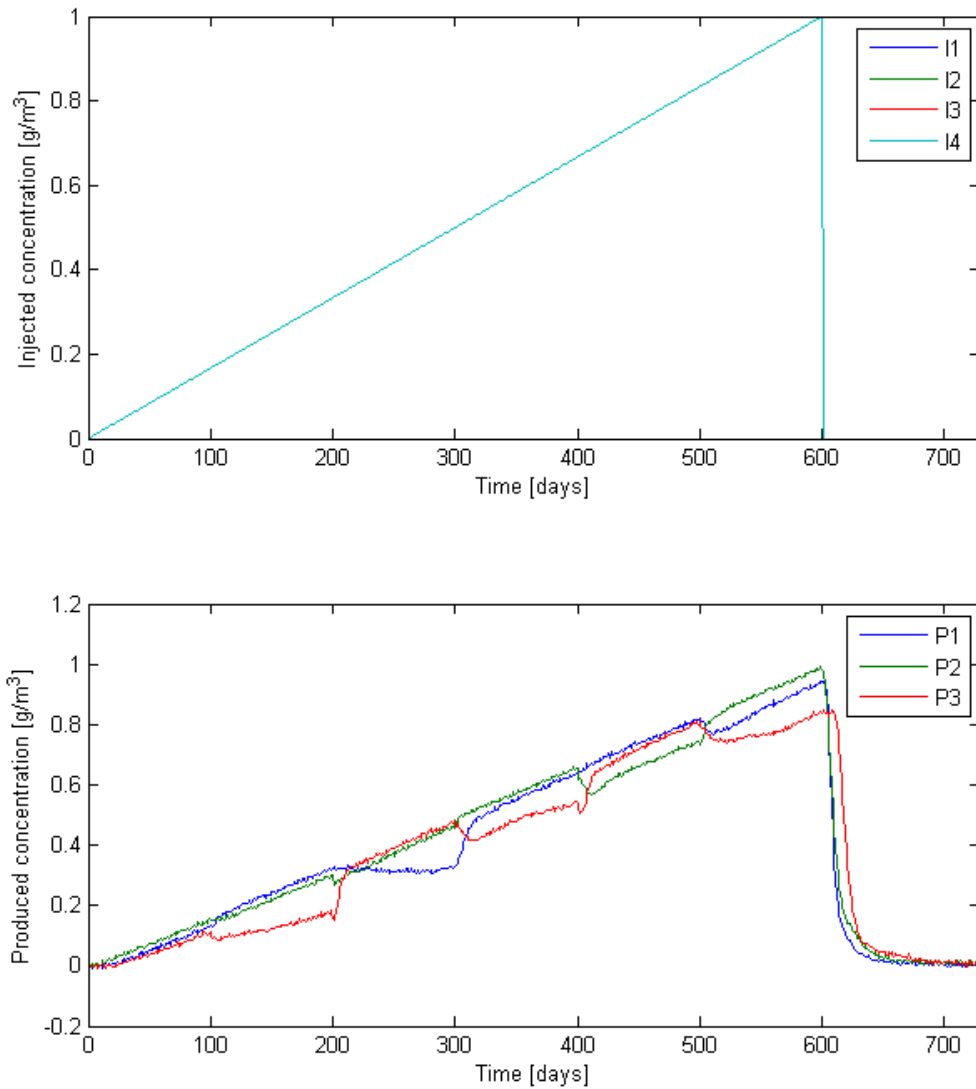


Figure 1.23: Injection and production history of tracer concentration in the variable flow rate – ramp concentration example for Reservoir Model II.

Finally, the tracer kernels would vary quite a bit depending on what the specific injection and production rates were. Several test runs with unit step injection of a different tracer into each well were performed to investigate the variability in the kernels. The kernels were computed in each case from Equation (2.29).

$$\kappa_{IiPj}(Q_{IiPj}) = \frac{1}{w_{IiPj}} \frac{\partial c_{Pj}^{step}}{\partial Q_{IiPj}} \quad (2.29)$$

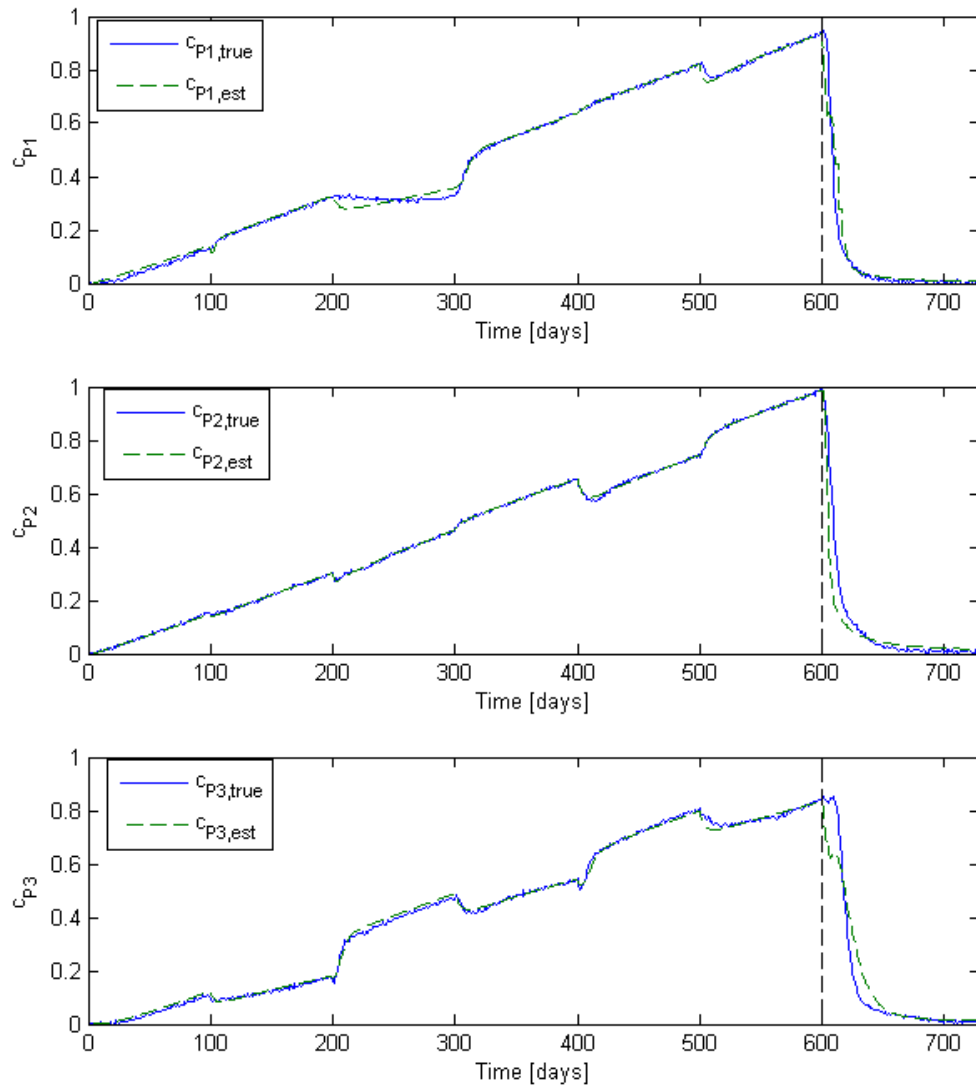


Figure 1.24: Model reproduction of the tracer production data in the variable flow rate - ramp tracer example for Reservoir Model II. The true data are shown as blue solid lines and the reproduced data are given by green dashed lines.

The configurations of the injection rates were as illustrated in Table 1.10. Each of the kernels computed from Equation (2.29) is shown in Figure 1.25, along with the kernel estimate found from solving the nonlinear regression problem.

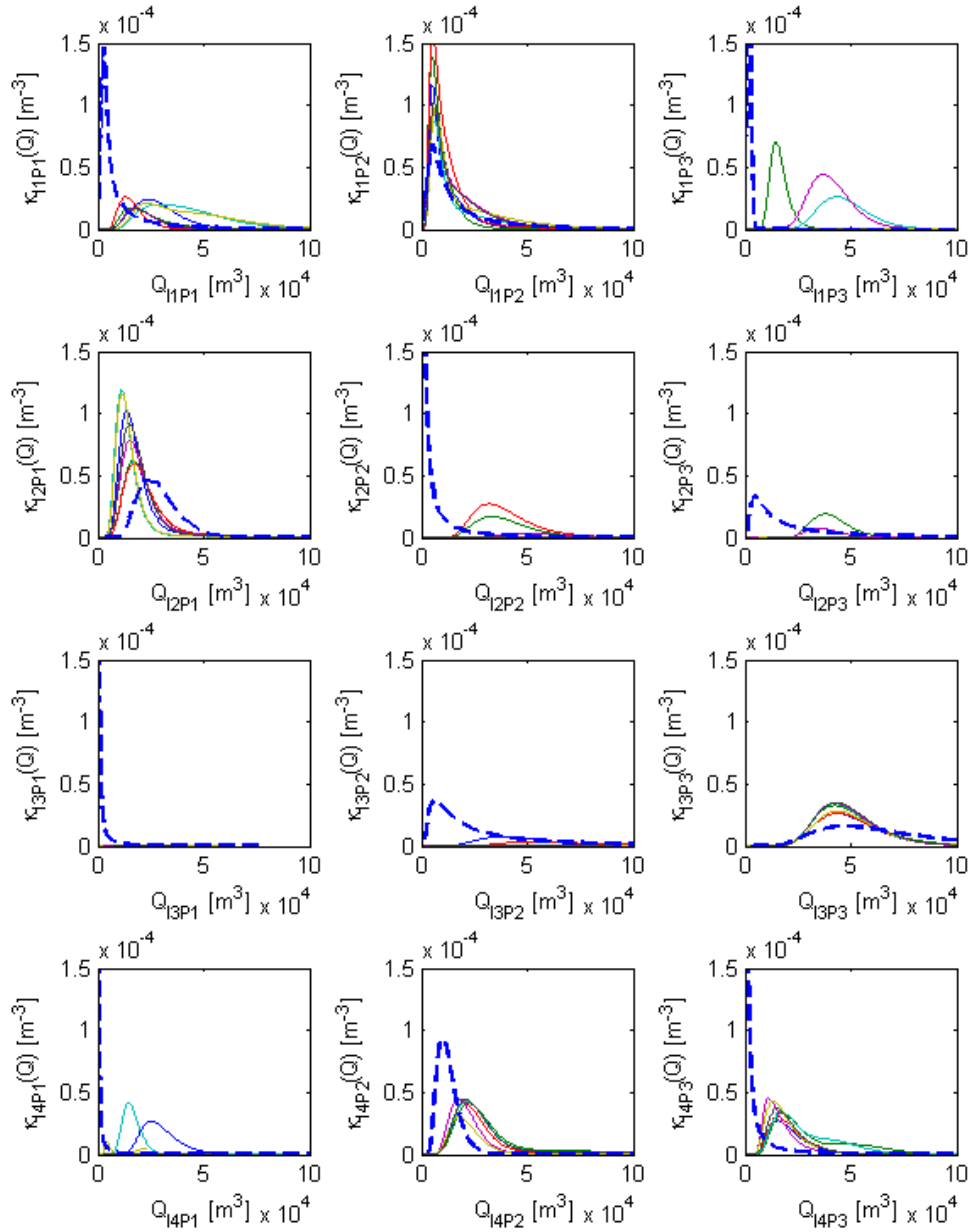


Figure 1.25: Parametric kernel estimates for each of the four injector-producer connections in Reservoir Model II. The "true" kernels for the various flow configurations are plotted with solid lines. The parametric estimates are given by blue dashed lines.

Table 1.10: Configurations of the injection rates used to illustrate the variability in tracer kernels for Model II. Injection rates are given in m^3/day .

	I1	I2	I3	I4
Config. 1	1200	1200	4800	4800
Config. 2	1200	4800	1200	4800
Config. 3	1200	1200	4800	1200
Config. 4	4800	4800	1200	4800
Config. 5	4800	1200	1200	1200
Config. 6	4800	4800	4800	1200
Config. 7	3000	3000	3000	3000

The kernel estimates are not quite as good in this case as in the constant flow rate case because the transient was less informative, and the model being used did not capture the physics of the problem as accurately. The estimates were still reasonable for the best connected kernels.

This fit yielded the $S0$ statistic significance of each kernel on the production data shown in Table 1.11. It should be noted that the statistic was quite sensitive to noise, at least for those kernels which were poorly connected. Thus, some weak connections would be rejected in one run, but accepted in another run with different random noise.

Table 1.11: Test statistic to determine the influence of each kernel in the varying flow rate – ramp concentration example for Model II.

S0	I1	I2	I3	I4
P1	3.2E-01	6.0E-01	1.0E-79	8.4E-02
P2	5.6E-01	7.3E-02	1.0E-17	3.7E-01
P3	6.8E-03	1.2E-03	9.3E-01	6.1E-02

1.6.2 Nonparametric Kernel Estimation Examples

The scenarios described in Section 1.6.1 were also modeled using a nonparametric approach. The results are described in the following two sections.

1.6.2.1 Constant Flow – Varying Concentration Example

The objective in this case was to estimate the tracer kernels using a nonparametric model, based on the injection and production history shown in Figure 1.19.

As noted earlier, the parametric kernel estimates were used as priors, κ_{prior} . Given a good prior, it was relatively straight forward to get a good fit to the production data by solving Problem (2.21). The resulting data fit is shown in Figure 1.26.

Relatively stringent conditions need to be applied for the convergence criteria for the optimization algorithm (MATLAB's *fmincon*) to get a good solution.

The weighting parameter for the regularization term, θ , was set to 10^5 to enforce smoothness in the kernel estimates, which are shown in Figure 1.27.

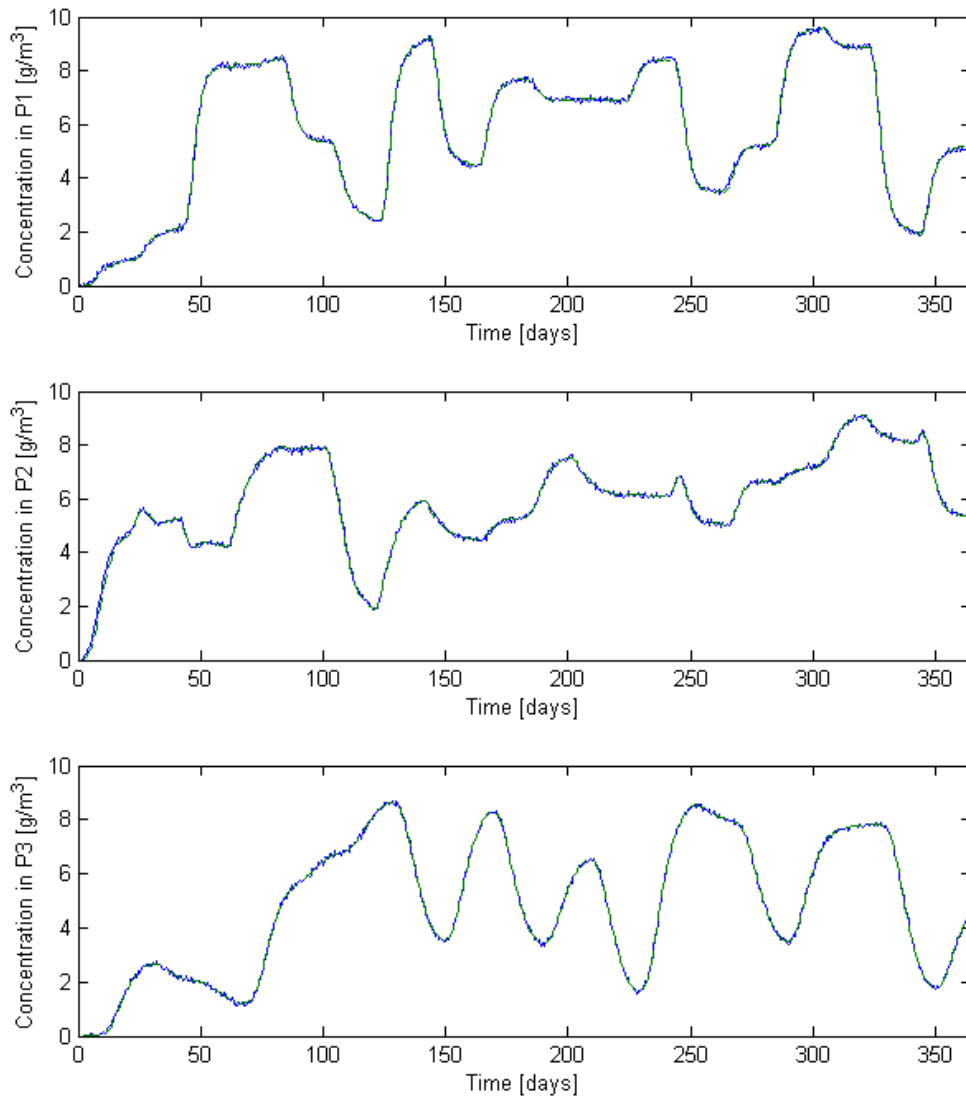


Figure 1.26: Fit to the production data from the constant flow - varying concentration example for Reservoir Model II, using nonparametric kernels.

The bootstrap method was used to assess the uncertainty in the kernel estimates. The results are shown in Figure 1.28. Some parts of the actual kernels fell outside of the 95% confidence interval. These were mostly the tail ends of some of the less significant kernels. Thus, the contribution of these parts to the signal was very small, and the shape of those tail estimates was probably more governed by the regularization term.

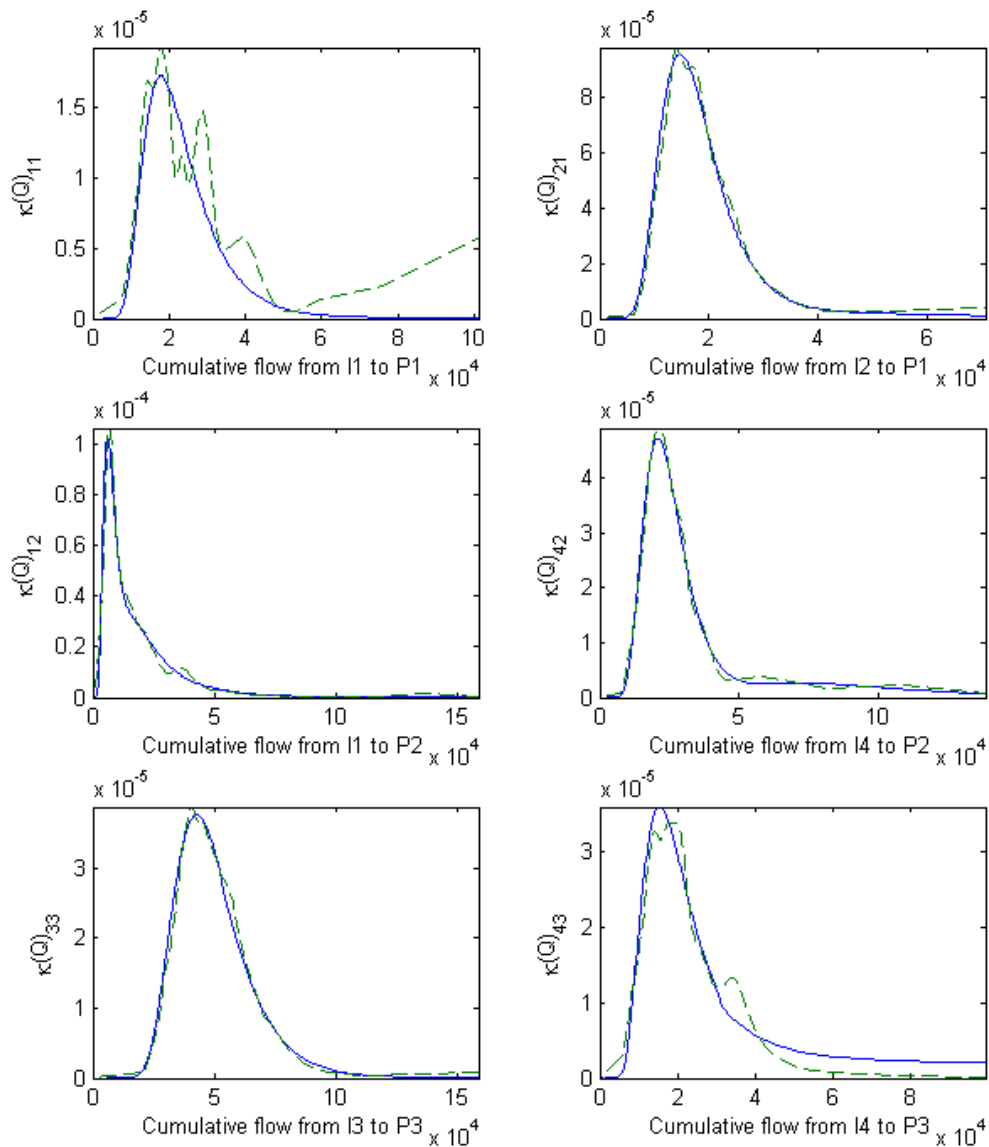


Figure 1.27: Nonparametric kernel estimates for those kernels deemed significant in the constant flow - varying tracer example for Reservoir Model II. The "true" kernels are given by blue solid lines while the estimates are in green dashed lines.

The advantage of having a nonparametric method for describing the kernels is most notable in this case, for example in the description of kernels IIP2 and I2P1.

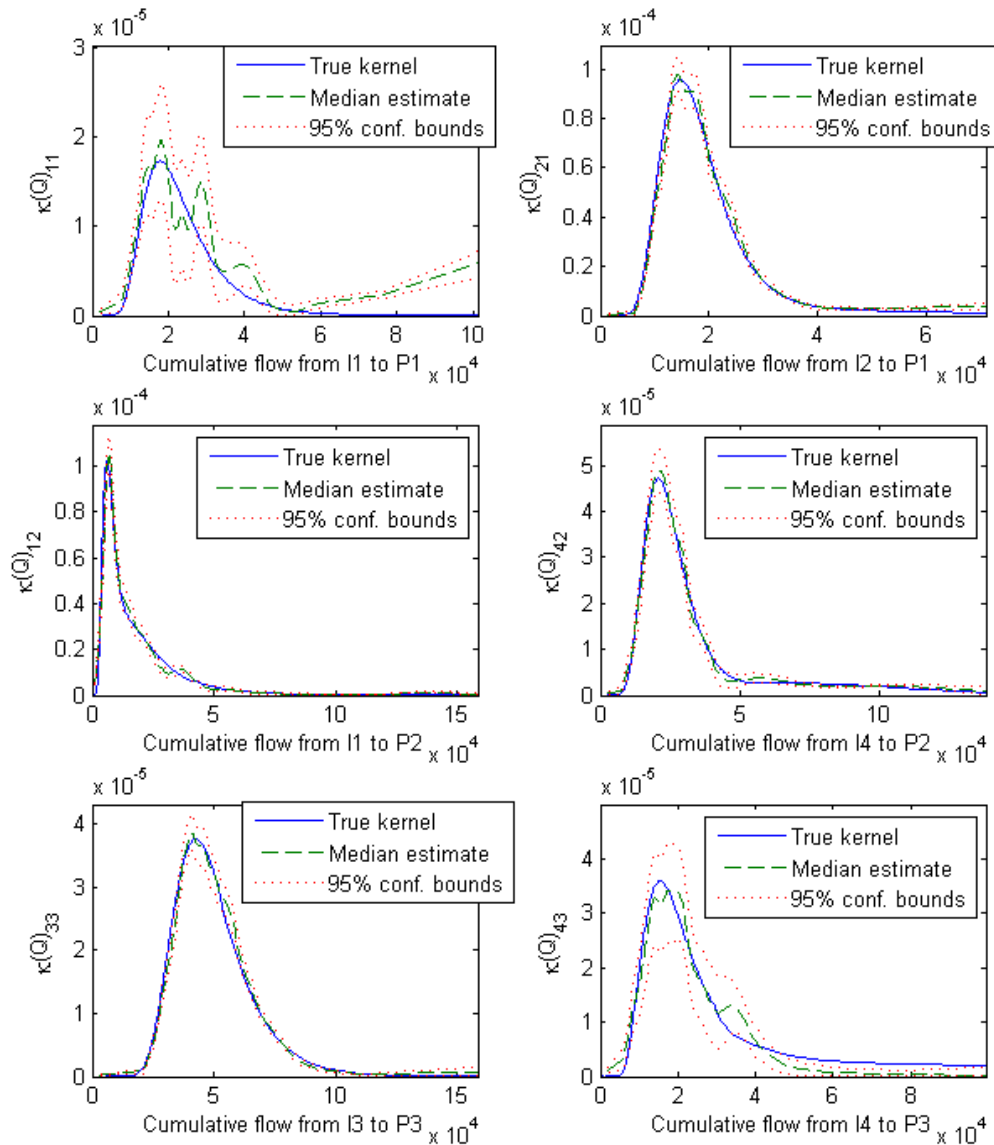


Figure 1.28: Nonparametric kernel estimates and 95% confidence bounds obtained from parametric bootstrapping for those kernels deemed significant in the constant flow - varying tracer example for Reservoir Model II.

1.6.2.2 Varying Flow – Ramp Concentration Example

The last example application is given for the varying flow –ramp concentration data set shown in Figure 1.23 and Figure 1.24. This was a particularly challenging problem because of the nonlinearities in the underlying physical model (see Section 1.6.1.2). With the inherent flexibility of the nonparametric curves, this made it very difficult to get smooth and realistic kernel estimates.

One of the problems was that using the results from the parametric model as an initial guess would only give a very good starting fit for the produced concentration, if the same discretization was used as well. Therefore the equal area discretization method discussed in Section 1.4 was not applied in this case. Another issue was that leaving some of the kernels out did not seem to work well and therefore all of them were included in the final model.

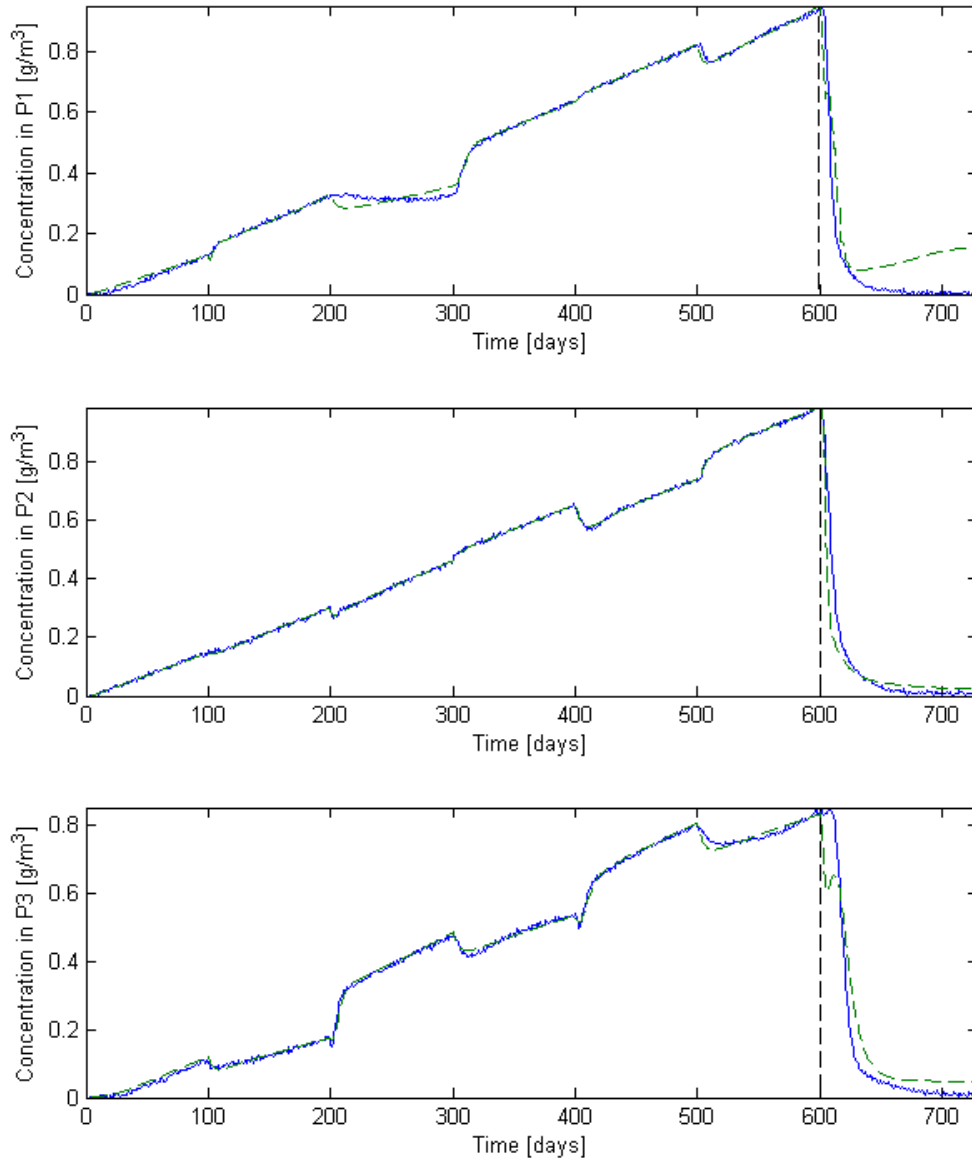


Figure 1.29: Fit to the production data from the varying flow - ramp concentration example for Reservoir Model II, using nonparametric kernels.

The data fit for this final example is shown in Figure 1.29. A fairly good fit was obtained for the first 600 days. The prediction starting at day 600 started to deviate a bit from the actual data near day 630, for producer P1. The reason is that the tail end of kernel IIP1 had a small bump (beyond the upper limit on the x-axis in Figure 1.30). This part of the kernel

could not be constrained by the data, although it might have been possible to constrain it with further manipulation of the regularization term.

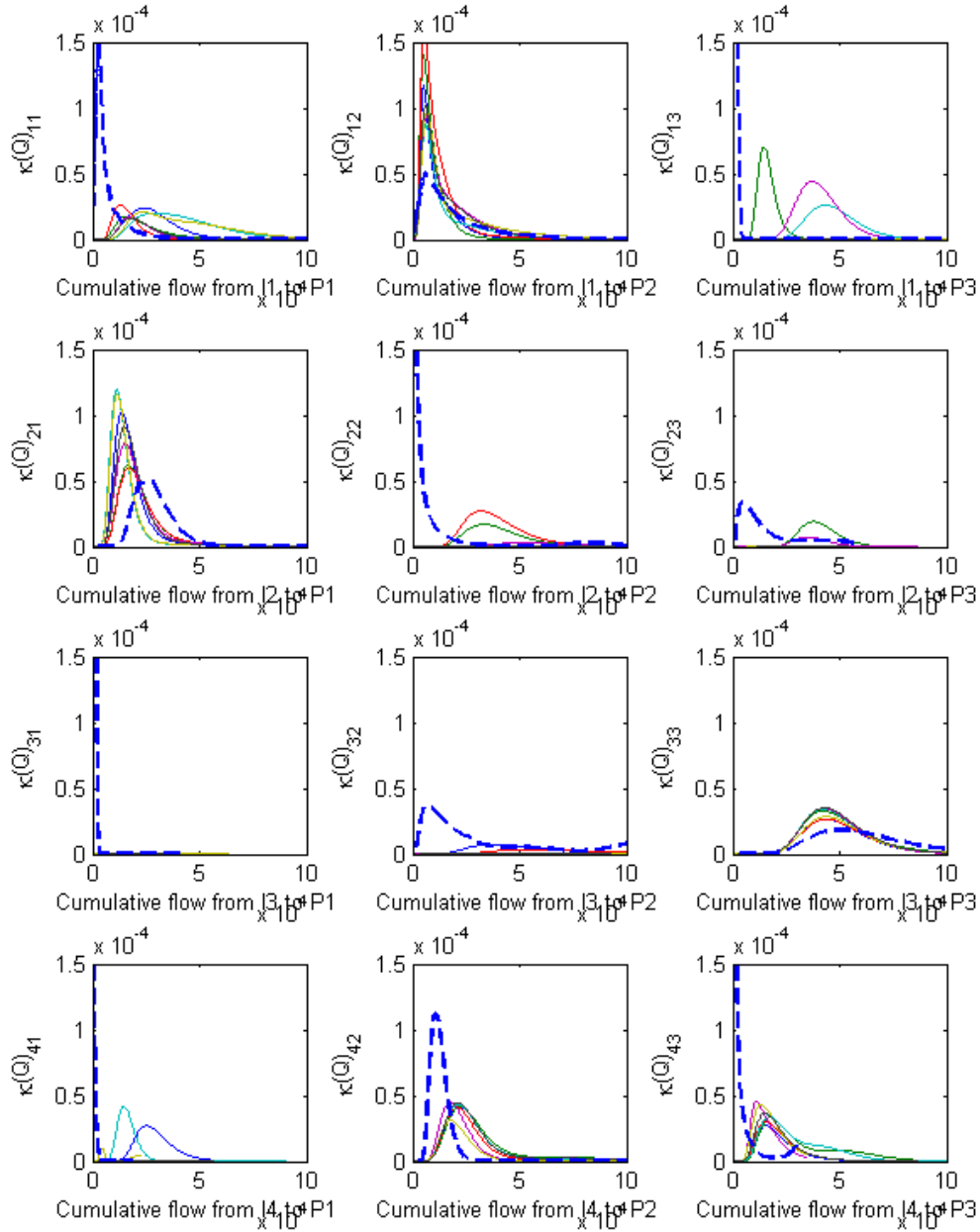


Figure 1.30: Nonparametric kernel estimates for the varying flow – ramp concentration example for Reservoir Model II.

The nonparametric kernel estimates for the varying flow – ramp concentration example are shown in Figure 1.30. These estimates are quite similar to the prior parametric kernel estimates. This was expected since the data fit for the parametric model was already quite good. The bootstrapping algorithm was not run for this case because each data fit took too

long (more than two hours), with the full discretization that had to be used to get a good initial guess.

2. FRACTURE CHARACTERIZATION OF ENHANCED GEOTHERMAL SYSTEMS USING NANOPARTICLES

This research project is being conducted by Research Associates Mohammed Alaskar and Morgan Ames, Senior Research Engineer Kewen Li and Professor Roland Horne. The objective of this study is to develop in-situ multifunction nanosensors for the characterization of Enhanced Geothermal Systems (EGS).

2.1 SUMMARY

During this quarter we began investigation of silica microparticle flow in a silicon micromodel. Fabrication of silicon wafers, containing manipulated images of Berea sandstone pore networks, was completed. Individual flow paths were isolated by anodic bonding of a glass wafer on top of the silicon wafer.

Initial injection of silica microspheres showed that particles accumulated at pore throats of grains adjacent to fracture channel. At this time, it was not clear if physical mechanisms caused by size, gravitational or electrostatic forces resulted in the particle entrapment. Attempts to enhance the recovery of particles, by increasing flow rates and/or changing ionic strength of post injection solution (NaCl of different molarity), were not successful.

A new synthesis procedure to achieve monodisperse tin-bismuth nanoparticles was attempted, and the resulting particles were characterized using Scanning Electron Microscopy (SEM). While many of the particles seemed to be fairly monodisperse and in the target size range, the presence of large micron-sized particles necessitates that the synthesis be repeated with adjusted parameters.

2.2 INTRODUCTION

Last quarter (July–September, 2011), we investigated the fracture caliper concept by injecting silica microsphere into a glass fracture model. The experimental apparatus configuration and standard measurements of fracture hydraulic aperture and permeability were completed. The fracture aperture was found to be around 57 μm , with corresponding average permeability of 272 darcy.

Preliminary injection of silica microspheres through the glass fracture model was conducted. We found that silica microspheres of 2 μm in diameter could be transported through the fracture, with a cumulative recovery of about 76%. This injection serves as a baseline experiment for future injections using the glass fracture model.

During this quarter, we investigated the flow mechanism of silica microspheres through the pore spaces of a micromodel. We fabricated the micromodel by creating an etched image of a Berea sandstone pore network into a silicon wafer. Transport of the silica microspheres was analyzed by acquiring images using an optical microscope. Work was also performed to adapt an emulsion synthesis procedure reported for monodisperse bismuth nanoparticles with the goal to synthesize monodisperse tin-bismuth nanoparticles.

2.3 MICROMODEL EXPERIMENTS

Micromodels have been developed to allow for flow visualization at the pore scale (Buckley, 1991). Micromodels are transparent network of porous structures and channels. The porous structures can be an artificial pattern such as straight or staggered cylinders to simulate grains, or real pore network found in natural rocks. Micromodels are two-dimensional systems and care must be taken when extrapolating the results to three-dimensional systems.

2.3.1 Fabrication of micromodels

The etched silicon wafer micromodels used in this work were of the type described by Sagar and Castanier (1997). A pore network of a repeated pattern obtained from an SEM (Scanning Electron Microscopy) image of Berea sandstone thin section (Figure 2.1A) was used. Continuity of repeated patterns was ensured by manipulating the image digitally (Figure 2.1B).

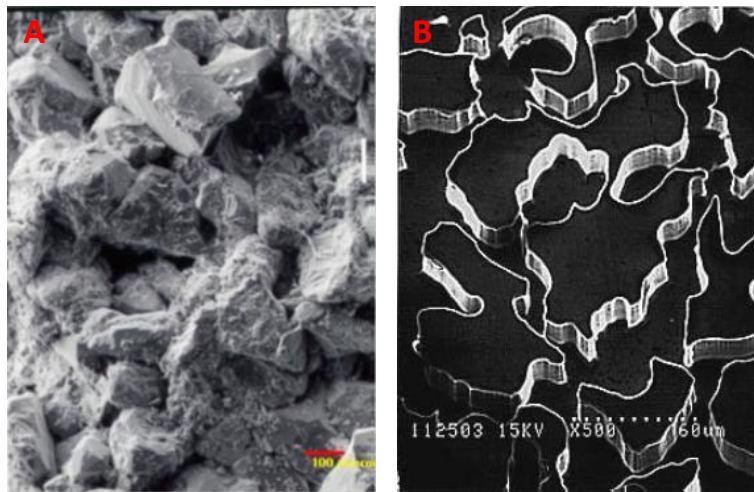


Figure 2.1: Berea sandstone thin section (A) SEM, and (B) digitally manipulated images (Rangel-Germán, 2002.)

Micromodels are made of 4-inch silicon wafers, K Prime, 4P <100> B S42565. The micromodels used in this study have 5-cm squared etched pore patterns and two flow channels (fractures) (Rangel-Germán, 2002). Each pattern is about 490 μm by 400 μm repeated more than 100 times across each side. A schematic of the micromodel is depicted in Figure 2.2. Grain sizes range from 30 to 300 μm and porosity is about 47% (Inwood, 2008). The permeability was measured and found to be approximately 1 darcy. further details of permeability measurement can be found in Section 2.3.3.

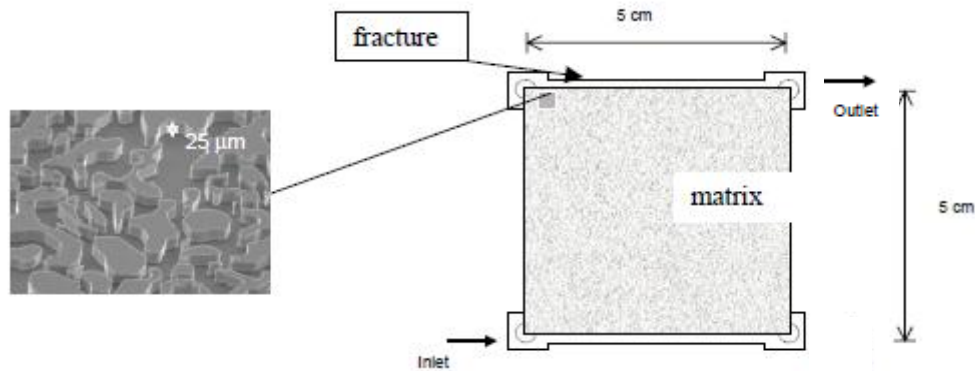


Figure 2.2: Schematic of the micromodel showing the repeated pattern and fracture channels (Rangel-Germán, 2002.). note that inlet and outlet port location were modified.

The fabrication of a micromodel begins with construction of a mask. The pore network image is reproduced as chrome on glass substrate. The grains on the glass replica are opaque while pores spaces are transparent. The image on the mask is transferred to the silicon wafer using a photoresist material (Hornbrook, 1991). Prior to the photoresist coating, the silicon wafer is dehydrated in an oven at 150°C for about 30 minutes. Dehydration involves priming the wafer with hexamethyldisilazane (HMDS) to improve the photoresist adhesion to the wafer (Alshehri, 2009).

A coating of the photoresist (Shipley 3612) is spun onto the wafer, resulting in 1.6 μm thick photoresist layer. The wafer is then baked at 90°C for 2 minutes until dry. The wafer is exposed to the mask using Karluss MA-6 contact mask aligner. During exposure, ultraviolet light is passed through the mask (Figure 2.3), leaving the photoresist coating only at grains. Soft contact program with 2.6 seconds exposure time and 40-μm gap width is selected. The silicon wafer is developed using Shipley MF-26A surfactant to remove unexposed photoresist, and then baked at 110°C for 2 minutes. After developing, the image transfer is completed and wafer is removed from the photolithography area and ready for etching.

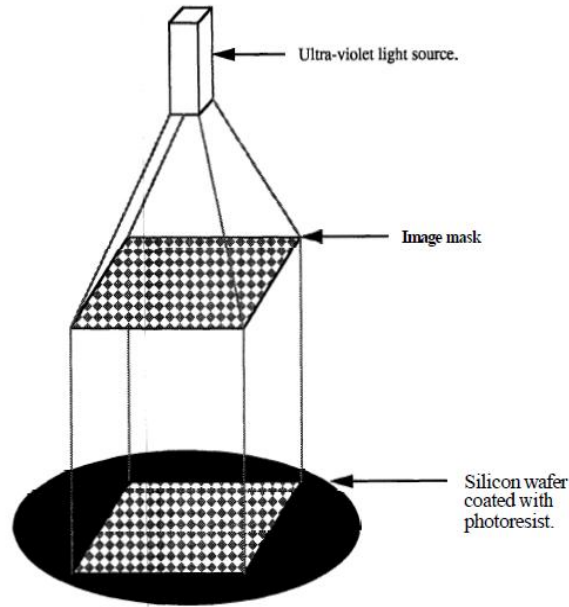


Figure 2.3: Schematic of image transfer or wafer exposure (Hornbrook, 1991).

The pore network image is dry etched using an inductive charged plasma deep reactive ion etcher. The etch process alternates between the passivating C₄F₈ plasma and the silicon etching SF₆ plasma. The wafer is etched to desired depth of approximately 25 μm . To isolate the individual flow channels, a borofloat glass wafer of 101.6 mm diameter and 1 mm thick is anodically bonded to the silicon wafer. In this work, 1 mm inlet and outlet ports were drilled, at the Stanford crystal shop, into the bonded glass substrate. Prior to bonding, wafers are cleaned in sulfuric acid/hydrogen peroxide (9:1 H₂SO₄:H₂O₂) solution bath at 120°C for 20 minutes, followed by 6-cycle deionized water rinse and spin dry.

The anodic bonding is found to form an irreversible bond between the glass and unetched portions of the silicon wafer. The bonding process involves hotplate, electrodes and power supply. The materials are arranged from bottom up: anode, etched silicon wafer, glass wafer and cathode (Hornbrook, 1991). Schematic of the bonding process is depicted in Figure 2.4.

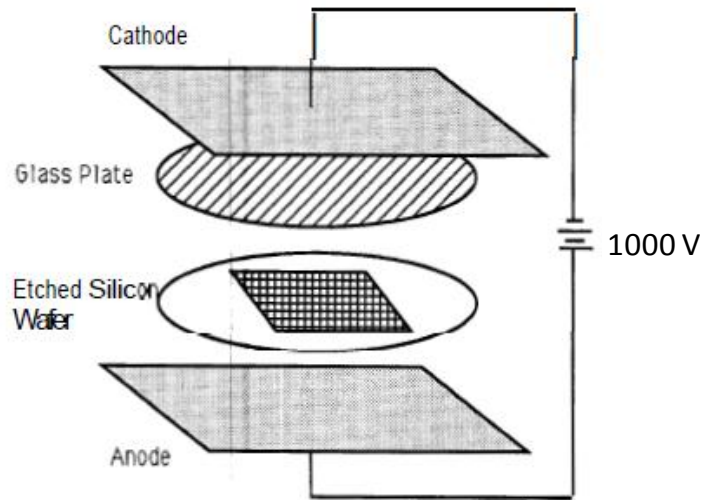


Figure 2.4: Schematic of bonding process (Hornbrook, 1991).

The bonding process starts by placing a clean silicon wafer (etched face up) on a hotplate preheated to 350°C for about 30 minutes. The wafer is dusted using compressed ultrapure air to ensure that the etched side is particle-free. A clean glass wafer is then placed carefully on top of the silicon wafer. An aluminum plate wrapped by a copper mesh is positioned above the wafers. The hotplate is connected to one electrode (anode) of the power supply, while the positive electrode (cathode) is connected to the aluminum plate. The power supply is brought to 1000 volts and left for about 45 minutes (Rangel-Germán, 2002). The bonding is observed as gradual change in color of the wafer, bonded areas appear black whereas unbounded regions appear light gray (Hornbrook, 1991).

2.3.2 Experimental Apparatus

The experimental apparatus is pictured in Figure 2.5. The apparatus consists of ultrapure water container, water pump, injection loop, pressure transducer, reflective light microscope and balance. Water used throughout the experiments was purified using Millipore A10 equipped with 0.220 μm filter. Images of particles in the micromodel pores were obtained with a reflective light microscope (Leica DM 2500 M) equipped with fast speed digital camera (Leica DFC400) controlled by Leica Application Suite (LAS) image analysis software. During particle injection experiments, images were acquired at specific times at different sections of the micromodel with a 10X, 20X or 50X objective (plus 10X eyepiece).

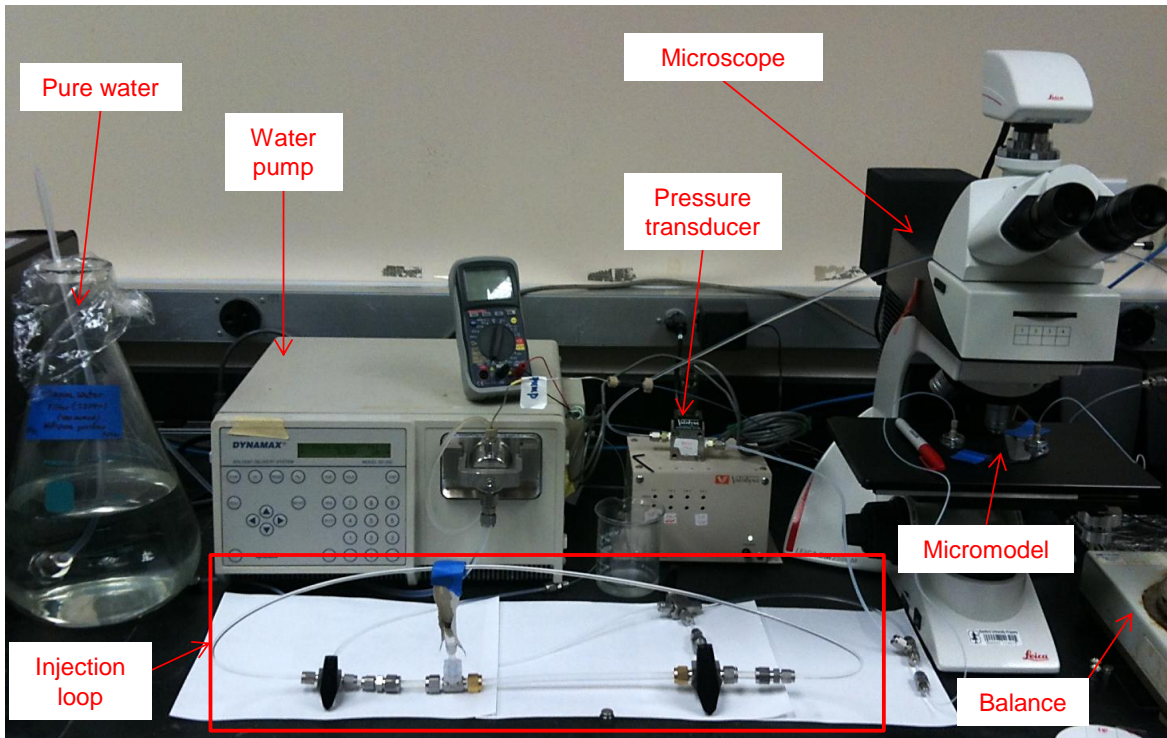


Figure 2.5: An image of the experimental apparatus.

Particles were injected using syringe through the injection loop. The injection loop allowed an alternating injection of colloid slug and particle free water, without interrupting the flow. Volumetric flow rates were varied between 0.05-1 cm³/min using steady state pump manufactured by Dynamax. The pump flow rate was calibrated using stop watch and balance (Mettler PM300) with 0.01 gram accuracy. The pump calibration curve is depicted in Figure 2.6. The differential pressure across the micromodel was measured using differential pressure transducer (Validyne Model DP215-50) with diaphragm (3-46) rated at maximum pressure of 50 psi. The transducer was calibrated with standard pressure gauge with accuracy of 1.25% of full range. The differential pressure transducer calibration curve is shown in Figure 2.7.

The micromodel was placed in a horizontal position on top of the microscope stage. The inlet and outlet ports were placed diagonally and fitted with special nanoport connection assemblies (Nano-Port model N-333 Headless, 1.5 mm diameter) for chip-base application (i.e. flat glass wafer) manufactured by IDEX Health and Science (Figure 2.8). The nanoports were attached to the glass wafer using an adhesive ring provided by the manufacturer according to the following procedure. First bonding surfaces were cleaned with isopropyl alcohol. The gasket seal was inserted on the recess in the bottom of the port and center the adhesive ring on glass wafer. The port was clamped to glass wafer and placed in oven at temperature of 170°C for one hour to develop complete bond between the ports and wafer.

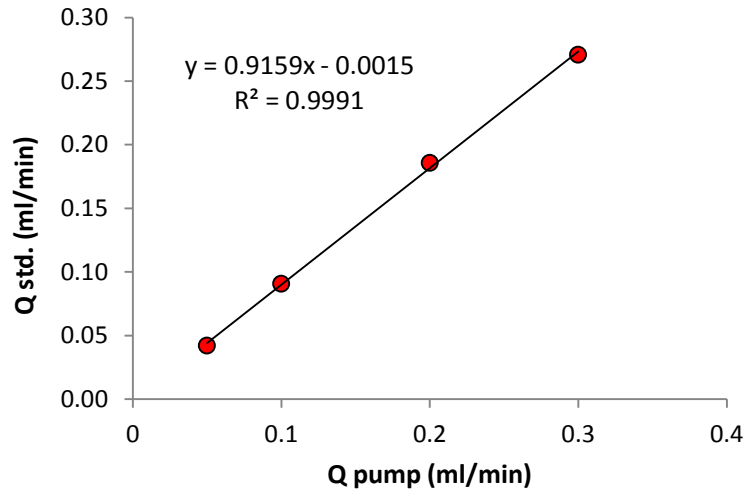


Figure 2.6: Pump calibration curve.

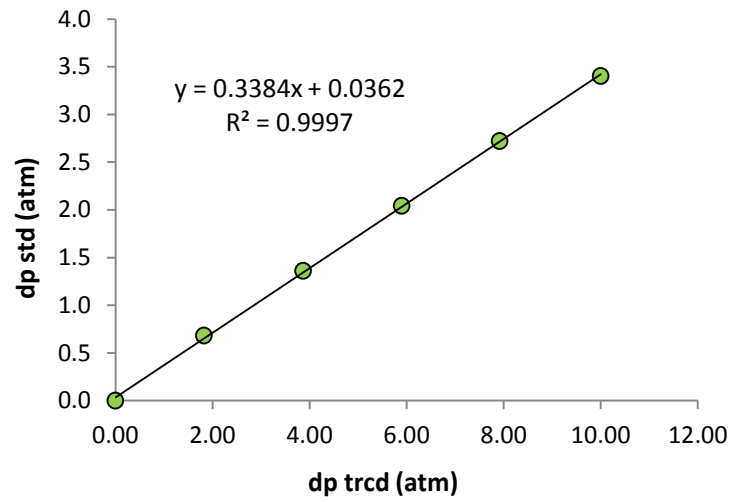


Figure 2.7: Differential pressure transducer calibration curve.

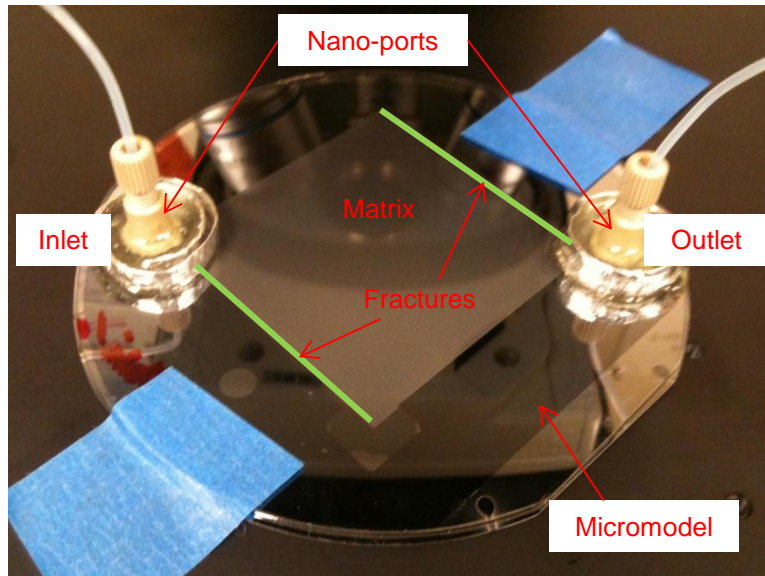


Figure 2.8: An image of the micromodel showing nano-ports, matrix and channels or fractures (green).

2.3.3 Micromodel permeability measurement

The permeability of the micromodel was measured at various flow rates ranging from 0.05-0.3 cm³/min. Higher flow rates were not used to avoid overpressurizing the micromodel. Initially, the micromodel and connecting tubes were all fully saturated with ultrapure water. Complete saturation of the micromodel was confirmed using image analysis. Darcy's Law of incompressible horizontal fluid flow was used to calculate the absolute permeability. Validity of Darcy's Law was confirmed by linearity between flow rates and pressure drop as shown in Figure 2.9.

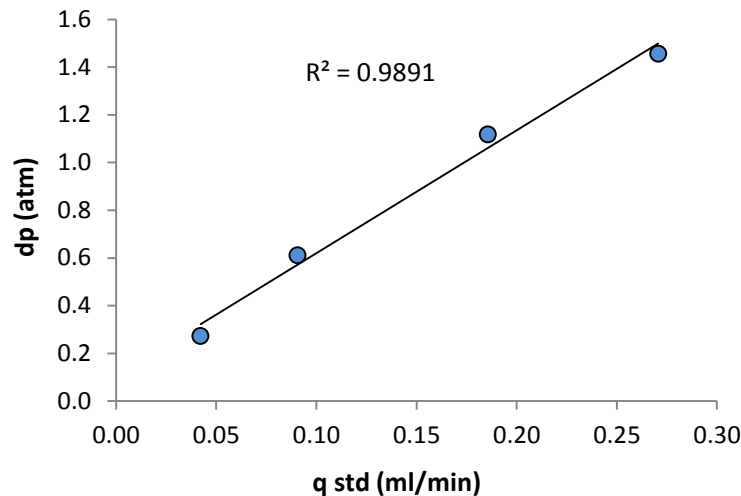


Figure 2.9: Linearity between volumetric flow rates and pressure drop confirm validity of Darcy's Law.

The area used was the cross-sectional area at the fracture-matrix interface (i.e. 5 cm by 0.0025 cm, length and depth of micromodel). The average absolute permeability was found to be approximately 1.09 darcy (Figure 2.10).

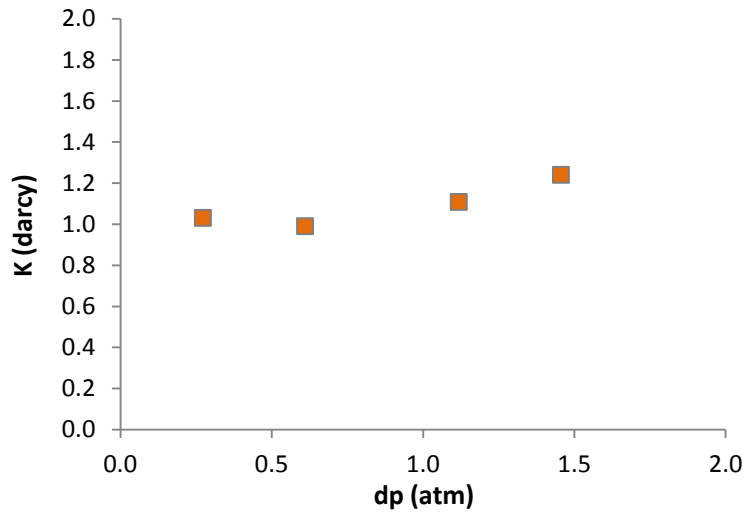


Figure 2.10: Absolute permeability measured at different pressure drops.

2.3.4 Particle injection into micromodel

Preliminary investigation of the flow mechanism of particles was conducted by injecting blue fluorescent silica microspheres through a micromodel with pore network replica of that naturally occurring Berea sandstone. The microspheres were characterized in terms of size and shape, and zeta potential. The zeta potential measurement was not possible because of the quick settlement of the silica microparticles to the bottom of the measurement cell (due to their size) during the analysis, leading to erroneous measurements. The size and shape of the microspheres were characterized using an optical microscope and scanning electron microscope (Figure 2.11).

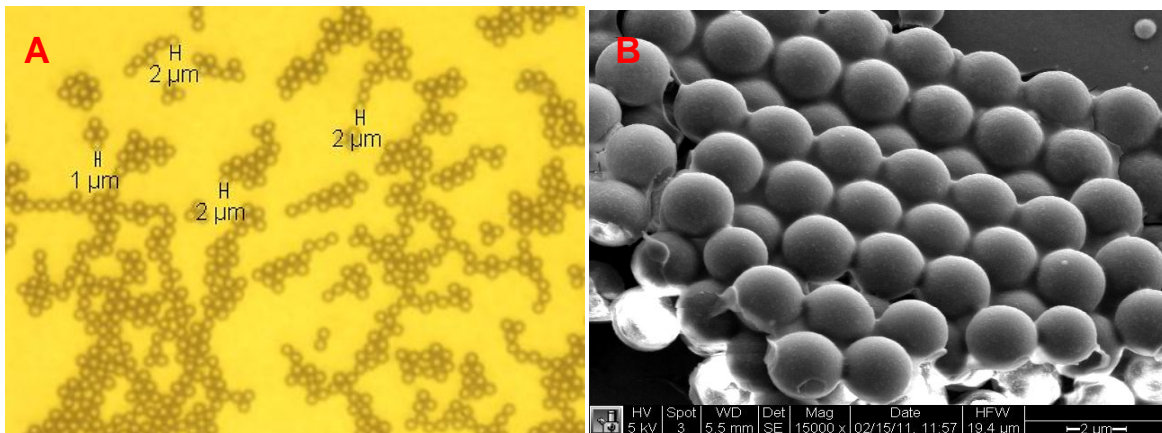


Figure 2.11: Blue microspheres (A) optical and (B) SEM images.

The sample was shown to have uniformly shaped spheres with an average particle size of about 2 μm . The sample was originally five cubic centimeters with concentration of five percent. The density of the sample was measured in the laboratory at temperature of 24.5°C. An accurate pipette was used to obtain one cubic centimeter of microfluid at original concentration. The weight of the one cubic centimeter sample was measured using a balance with one milligram accuracy. It was found that the density of the blue silica microfluid sample was about $4.995 \times 10^{-2} \text{ g/cm}^3$.

The microfluid was contained in a syringe downstream the water pump. The sample was injected into the injection loop and flowed to the micromodel using the pump. Influent samples of two concentrations, one part to 50 and 200 parts of deionized water, were prepared. The new concentrations of (1:50 and 1:200) diluted samples were 9.99×10^{-4} and $2.49 \times 10^{-4} \text{ g/cm}^3$, respectively. The volume injected of 1:50 and 1:200 diluted samples was three and two cubic centimeter, respectively. Prior to the injection of the microfluid, the micromodel was fully saturated with ultrapure water (same water used during post injection).

2.4 SYNTHESIS AND CHARACTERIZATION OF TIN-BISMUTH NANOPARTICLES

Tin-bismuth nanoparticles are being investigated as candidate nanosensors. Tin-bismuth was chosen as a material of interest due to the capability to tune its melting point within a wide temperature range of geothermal temperatures (139°C – 271°C) by changing the alloy composition. In previous quarterly reports (Apr – Jun 2010, Jul – Sep 2010, Oct – Dec 2010 and Jan – Mar 2011), we have reported on work done with tin-bismuth nanoparticles. Tin-bismuth nanoparticles were synthesized in mineral oil using an ultrasonic processor, resulting in a wide particle size distribution (100 – 500 nm). A heating experiment was performed, and particle growth and a widening of the size distribution was observed (100 – 1000 nm). A sample of these particles was injected into a Berea sandstone core, and no particles larger than 200 nm were recovered in the effluent. In order to determine whether tin-bismuth nanoparticles with diameters less than 200 nm could be recovered successfully, we attempted to centrifugally separate size fractions of the nanofluid. However, the particle size distributions after separation did not fit the desired criteria.

In order to generate more conclusive results to heating and injection experiments of tin-bismuth nanoparticles and more definitively evaluate their feasibility as geothermal nanosensors, it is desired to synthesize monodisperse tin-bismuth nanoparticles with a mean particle diameter of about 100 nm. This was not achieved using the sonochemical synthesis procedure due to limitations of the ultrasonic processor used. For this reason, a different synthesis route was attempted, which is based on reported methods to synthesize monodisperse bismuth nanoparticles with the same mean particle diameter (Wang 2004).

2.4.1 Emulsion synthesis of tin-bismuth nanoparticles

The top-down emulsion synthesis method reported by Wang and Xia (2004) was adapted with the goal to synthesize monodisperse tin-bismuth nanoparticles with a mean particle diameter of 100 nm. After two unsuccessful attempts to yield nanoparticles, the synthesis parameters were adjusted to the following. 0.07 gm eutectic tin-bismuth powder (300 mesh, American Elements) and 0.2 gm Poly(vinyl pyrrolidone) (PVP) were added to 20 ml diethylene glycol (DEG) at 130°C and stirred at 1100 rpm for 20 minutes. The ~50 µm tin-bismuth powder melted to produce liquid droplets, which were broken into smaller droplets by the shear forces associated with vigorous stirring. The PVP was used to stabilize these smaller droplets in suspension. After stirring, this hot emulsion was poured into 200 ml of cold ethanol at 5°C. The particles were harvested using centrifugation, washed with a 100 mM solution of PVP in ethanol, centrifuged again, and suspended in deionized water. All centrifugations were performed at 6000 rpm for 15 minutes.

2.4.2 Characterization of tin-bismuth nanoparticles

The tin-bismuth nanoparticles were characterized using SEM. The resulting SEM images are displayed in Figure 2.12.

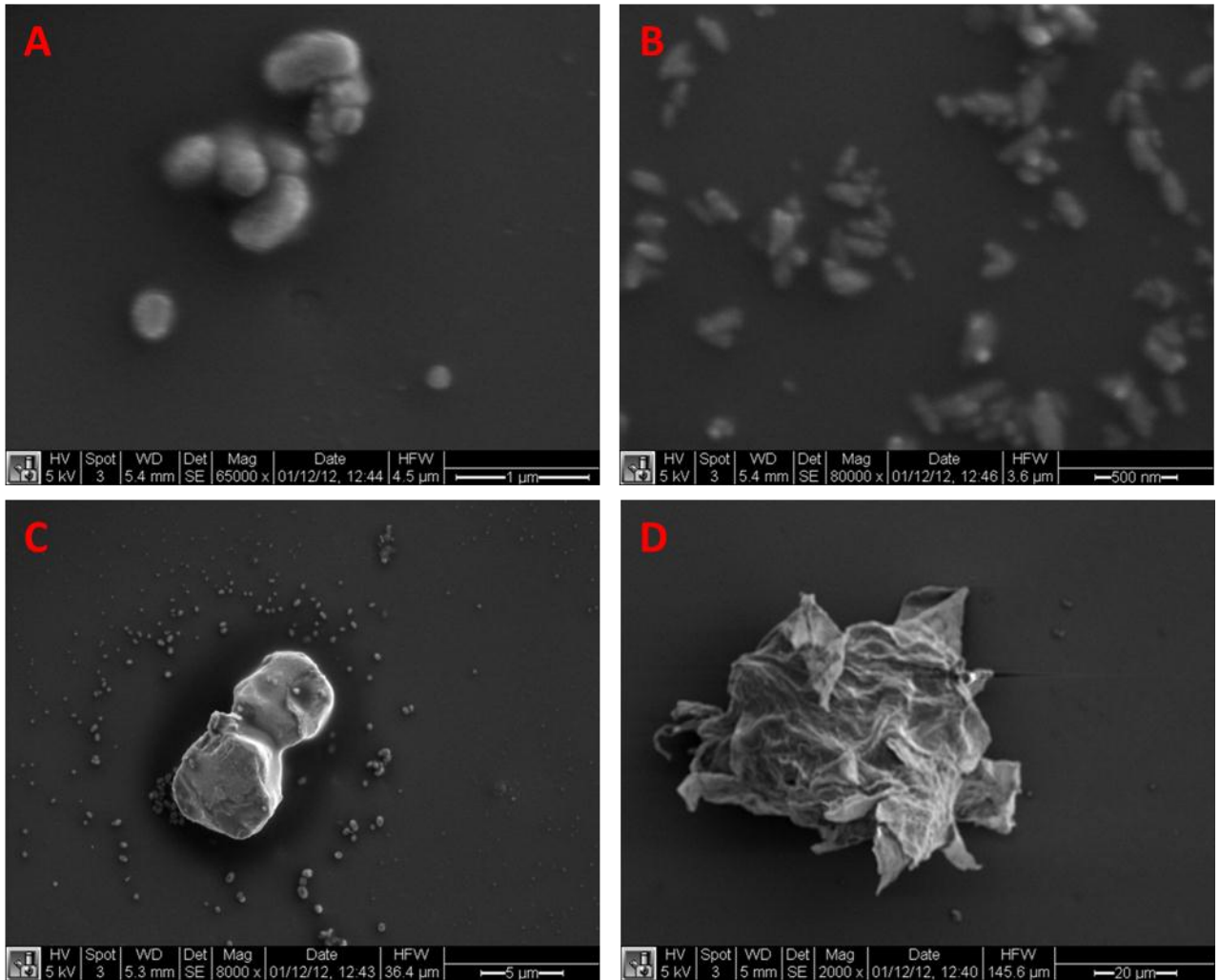


Figure 2.12: SEM images showing (A), (B, and (C) tin-bismuth nanoparticles and (D) poly(vinyl pyrrolidone).

The images shown in Figure 2.12A and B suggest that both spherical and ellipsoidal tin-bismuth nanoparticles were synthesized, and that the particle size distribution is not as uniform as desired. The large tin-bismuth particle shown in Figure 2.12C has a length of 10 μm, demonstrating that the sample synthesized does not meet the predetermined quality criteria. Finally, the particle shown in Figure 2.12D does not have the same structure as the tin-bismuth particles, suggesting that it is PVP. The synthesis process will be repeated, adjusting the synthesis parameters of PVP amount, emulsion temperature, and ethanol temperature.

2.5 RESULTS

This section provides the results of the preliminary injection of fluorescent silica microspheres into the micromodel. One objective was to study visually the way that particles enter pore throats, and perhaps visualize the plugging or bridging mechanisms. The silica microspheres were found trapped at pore throats of grains adjacent to the

fracture (Figure 2.13-14). The minimum flow rate ($0.05 \text{ cm}^3/\text{min}$) or Darcy velocity of $9 \text{ cm}/\text{min}$ was determined to be significantly higher than should have been used in order to observe particles in motion. The microspheres appear to snap between pore throats at even higher velocities. It was hypothesized that some particles were transported; however, effluent samples collected during injection have not been analyzed yet.

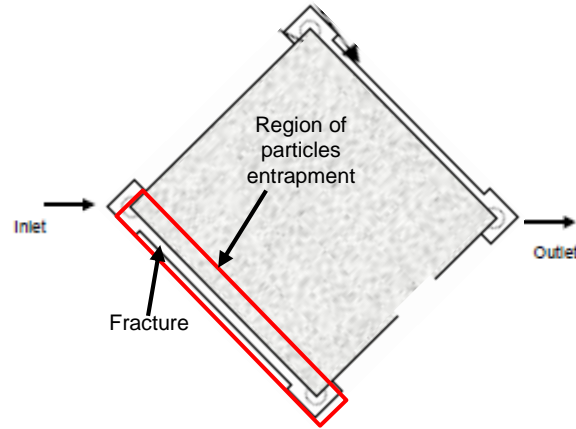


Figure 2.13: Schematic of micromodel showing general region of microspheres entrapment.

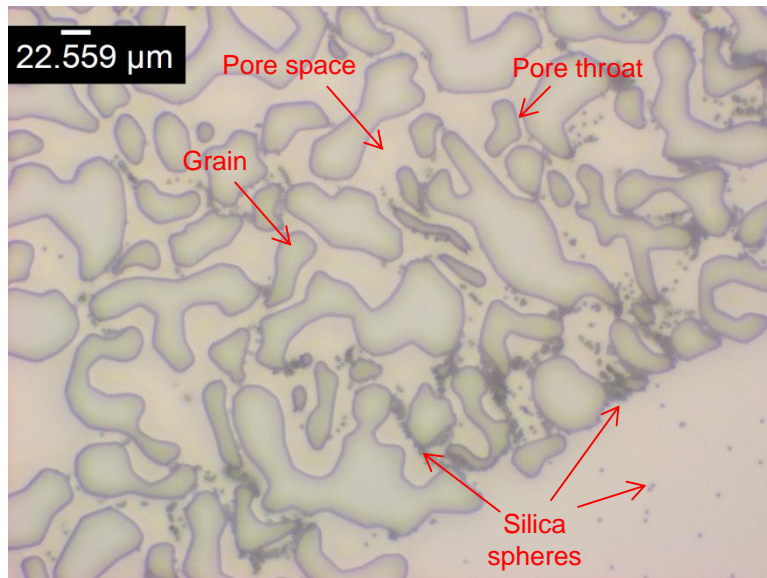


Figure 2.14: Optical image of pore network showing the silica microsphere trapped at pore throats, at 200X magnification.

Attempts to recover microspheres by increasing flow rate and/or pressure drop (increase of viscous forces) and changing the ionic strength (electrostatic forces) of solution were carried out. Increasing flow rates by 20 fold did not mobilize the microspheres. Figure 2.15 shows two optical images taken at 0.05 and $1 \text{ cm}^3/\text{min}$ (after 5 minutes or post-injection of 166 pore volumes) at the same location. By comparison, the two images were identical; neither particles at the pore throats nor those in the pore space were mobilized by viscous forces.

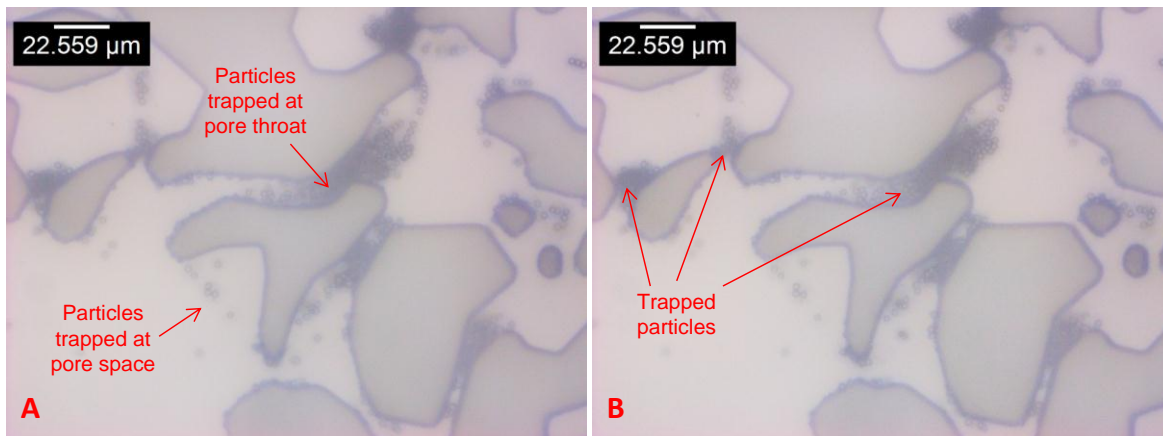


Figure 2.15: Optical images taken at the same location in micromodel at injection flow rates of (A) 0.05, and (B) 1 cm³/min, at 500X magnification.

Mobility of the microspheres was not improved by changing ionic strength of post-injected water. Two ionic strength solutions were prepared, 0.001 M and 0.01 M NaCl. Figure 2.16 shows comparison of the trapped microspheres before and after post-injection of 234 pore volumes of 0.001 M NaCl solution at same flow rate (0.3 cm³/min). There was no observable change in recovery. Similarly, an order of magnitude increase of salt content (0.01 M NaCl) had no effect on demobilizing particles at region of interest (Figure 2.17).

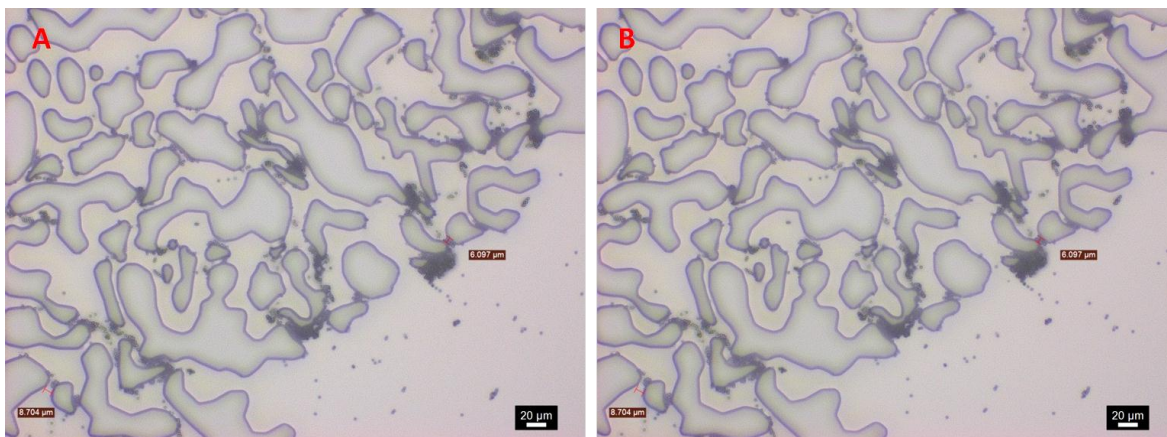


Figure 2.16: Optical images taken at the same location in micromodel (A) before, and (B) after the injection of 234 PV of 0.001 M NaCl, at 200X magnification.

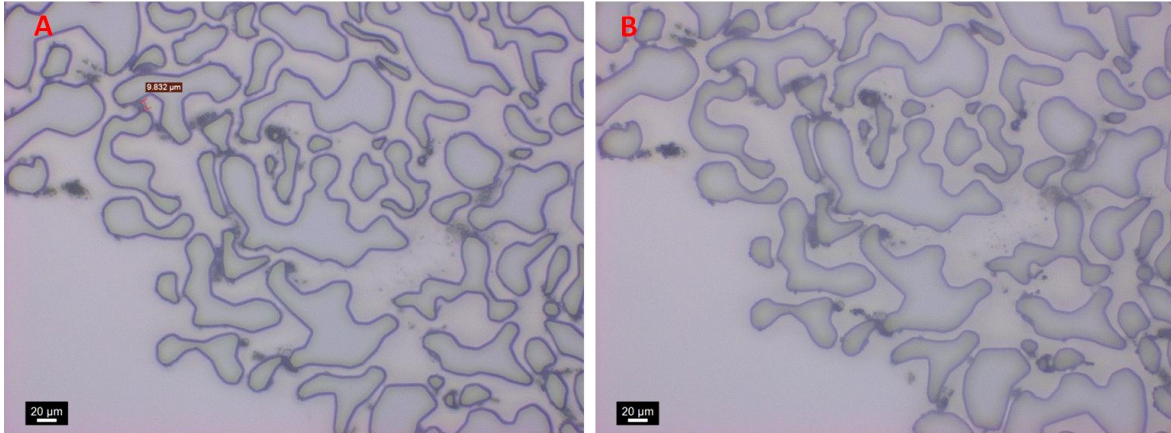


Figure 2.17: Optical images taken at the same location in micromodel (A) before, and (B) after the injection of 0.01 M NaCl for 30 minutes, at 200X magnification.

2.5 FUTURE WORK

It is planned to continue our investigation of the flow of particles through the micromodel. We plan to inject at lower flow rate using syringe pumps to visually study the flow mechanism of particles through pore throats. Injection experiments with particles that have similar density as water will be conducted. It is also planned to repeat the emulsion synthesis of tin-bismuth particles with tuned synthesis parameters in order to achieve a monodisperse sample.

3. FRACTURE CHARACTERIZATION USING RESISTIVITY

This research project is being conducted by Research Assistant Lilja Magnusdottir, Senior Research Engineer Kewen Li and Professor Roland Horne. The objective of this project is to investigate ways to use resistivity to infer fracture properties in geothermal reservoirs.

3.1 SUMMARY

In this project, the aim is to use Electrical Resistivity Tomography (ERT) to characterize fracture properties in geothermal fields. The resistivity distribution of a field can be estimated by measuring potential differences between various points while injecting an electric current into the ground and resistivity data can be used to infer fracture properties due to the large contrast in resistivity between water and rock. The contrast between rock and fractures can be increased further by injecting a conductive tracer into the reservoir, thereby decreasing the resistivity of the fractures. In this project, the potential difference has been calculated between two points (an injector and a producer) as conductive fluid flows through fracture networks. The time history of the potential field depends on the fracture network and can therefore be used to estimate where fractures are located and the character of their distribution.

The flow simulator TOUGH2 was used to calculate how the conductive tracer distributes through the reservoir and the analogy between Ohm's law that describes electrical flow and Darcy's law describing fluid flow made it possible to use TOUGH2 also to calculate the electric fields. The EOS1 module in TOUGH2 was used to calculate the tracer flow and EOS9 module was used to calculate the electric potential. First, the time history of the potential difference between an injector and a producer was calculated for two simple fracture networks to explore the relationship between fracture networks and the changes in potential field. Next, the time histories of the potential difference was studied for more realistic fracture networks by using a discrete-fracture model introduced by Karimi-Fard et al. (2003) to create more complicated fracture networks. Four cases were studied and they all gave different results for the time histories of the potential difference, verifying that the potential field is dependent on the fracture networks.

Future work includes looking at more fracture networks and greater number of wells to study further the relationship between fracture networks and the change in potential differences as conductive tracer is injected into the reservoir. Future work also includes implementing self-potential calculations into the model since the change in self-potential affects the measured potential difference and could facilitate fracture characterization. Another future goal is to study the possibility of using the potential differences with inverse modeling to characterize fracture patterns as well as to study different electrode layouts. It is also of interest to explore the use of nanotracers and the influence of injecting varying tracer concentrations.

3.2 INTRODUCTION

Characterizing the dimensions and topology of fractures in geothermal reservoirs is crucial for optimal designing of production and to find feasible drilling locations. Fractures carry most of the fluid in the reservoir so fracture configuration is central to the performance of a

geothermal system both in fractured reservoirs as well as in Enhanced Geothermal System (EGS) applications. The knowledge of fluid-flow patterns is necessary to ensure adequate supply of geothermal fluids and efficient operation of geothermal wells and to prevent short-circuiting flow paths from injector to producer that would lead to premature thermal breakthrough. Fracture characterization therefore increases the reliability of geothermal wells and the overall productivity of geothermal power plants.

The goal of this study is to find ways to use Electrical Resistivity Tomography (ERT) to characterize fractures in geothermal reservoirs. ERT is a technique for imaging the resistivity of a subsurface from electrical measurements. Pritchett (2004) concluded based on a theoretical study that hidden geothermal resources can be explored by electrical resistivity surveys because geothermal reservoirs are usually characterized by substantially reduced electrical resistivity relative to their surroundings. Electrical current moving through the reservoir passes mainly through fluid-filled fractures and pore spaces because the rock itself is normally a good insulator. In these surveys, a direct current is sent into the ground through electrodes and the voltage differences between them are recorded. The input current and measured voltage difference give information about the subsurface resistivity, which can then be used to infer fracture locations.

Resistivity measurements have been used in the medical industry to image the internal conductivity of the human body, for example to monitor epilepsy, strokes and lung functions as discussed by Holder (2004). In Iceland, ERT methods have been used to map geothermal reservoirs. Arnarson (2001) describes how different resistivity measurements have been used effectively to locate high temperature fields by using electrodes located on the ground's surface. Stacey et al. (2006) investigated the feasibility of using resistivity to measure saturation in a rock core. A direct current pulse was applied through electrodes attached in rings around a sandstone core and it resulted in data that could be used to infer the resistivity distribution and thereby the saturation distribution in the core. It was also concluded by Wang and Horne (2000) that resistivity data have high resolution power in the depth direction and are capable of sensing the areal heterogeneity.

In the approach considered in this project so far, electrodes would be placed inside two or three geothermal wells and the potential differences between them studied to locate fractures and infer their properties. Due to the limited number of measurement points, the study is investigating ways to enhance the process of characterizing fractures from sparse resistivity data. For example, in order to enhance the contrast in resistivity between the rock and fracture zones, a conductive tracer would be injected into the reservoir and the time-dependent voltage difference measured as the tracer distributes through the fracture network.

Slater et al. (2000) have shown a possible way of using ERT with a tracer injection by observing tracer migration through a sand/clay sequence in an experimental $10 \times 10 \times 3 \text{ m}^3$ tank with cross-borehole electrical imaging. Singha and Gorelick (2005) also used cross-well electrical imaging to monitor migration of a saline tracer in a $10 \times 14 \times 35 \text{ m}^3$ tank. In previous work, usually many electrodes were used to obtain the resistivity distribution for

the whole field at each time step. The resistivity distribution was then compared to the background distribution (without any tracer) to see resistivity changes in each block visually. These resistivity changes helped locate the saline tracer and thereby the fractures. Using this method for a whole reservoir would require a gigantic parameter space, and the inverse problem would not likely be solvable, except at very low resolution. However, in the method considered in this study, the potential difference between the wells which corresponds to the changes in resistivity, would be measured and plotted as a function of time while the conductive tracer flows through the fracture network. Future work will involve finding ways to use that response, i.e. potential difference vs. time, in an inverse modeling process to help characterizing the fracture pattern.

First, the analogy between water flow and electrical flow is defined and the resistivity of a saline tracer is studied. Next, the time history of the potential difference between an injector and a producer is calculated for two simple fracture networks to explore the relationship between fracture networks and the changes in potential field. The time histories of the potential difference is also studied for more realistic fracture networks by using a discrete-fracture model introduced by Karimi-Fard et al. (2003) to create more complicated fracture networks. Finally, future work is outlined.

3.3 WATER FLOW ANALOGY OF ELECTRICAL FLOW

The steady-state flow of an electric current through a conducting medium due to differences in energy potential is analogous to the steady-state flow of a fluid through porous medium. Darcy's law is an empirical relationship similar to Ohm's law,

$$J = -\sigma \nabla \varphi \quad (3.1)$$

where J is current density [A/m^2], σ is the conductivity of the medium [Ωm] and φ is the electric potential [V] but instead of describing electrical flow Darcy's law describes fluid flow through a porous medium,

$$q = -\frac{k}{\mu} \nabla p \quad (3.2)$$

where q is the flow rate [m/s], k is permeability [m^2], μ is viscosity of the fluid [kg/ms] and p is pressure [Pa]. Table 1 presents the correspondence between the variables and relations of water flow (Darcy's law) and electric current flow (Ohm's law).

Table 1: Correspondence between electric current flow and water flow.

	Darcy's law: $q = -\frac{k}{\mu} \nabla p$	Ohm's law: $J = -\sigma \nabla \phi$
Flux of:	Water q [m/s]	Charge J [A/m ³]
Potential:	Pressure p [Pa]	Voltage ϕ [V]
Medium property:	Hydraulic conductivity $\frac{k}{\mu}$ [m ² /Pa·s]	Electrical conductivity σ [1/Ωm]

The similarities between these two equations imply that it is possible to use flow simulator like TOUGH2 to solve electric field due to flow of electric current. Then, the pressure results from TOUGH2 would correspond to the electric voltage, the current density to the flow of water and the electrical conductivity would correspond to the hydraulic conductivity, i.e.

$$\sigma = \frac{k}{\mu} \quad (3.3)$$

However, it must be taken into account that viscosity depends on pressure while conductivity of a reservoir does not depend on the electric voltage used. Previous quarterly report (July-September) described how the EOS9 module in TOUGH2 was successfully used to solve the electric field by defining the liquid viscosity, density and compressibility constant.

3.4 RESISTIVITY OF A SALINE TRACER SOLUTION

The tracer injected into the reservoir is a NaCl solution whose resistivity changes with temperature and concentration. Ucoq et al. (1980) have established experimentally the resistivity of saline fluids over the temperature range 20-350°C and their results for resistivity of NaCl solution calculated using a three-dimensional regression formula is shown in Figure 3.1.

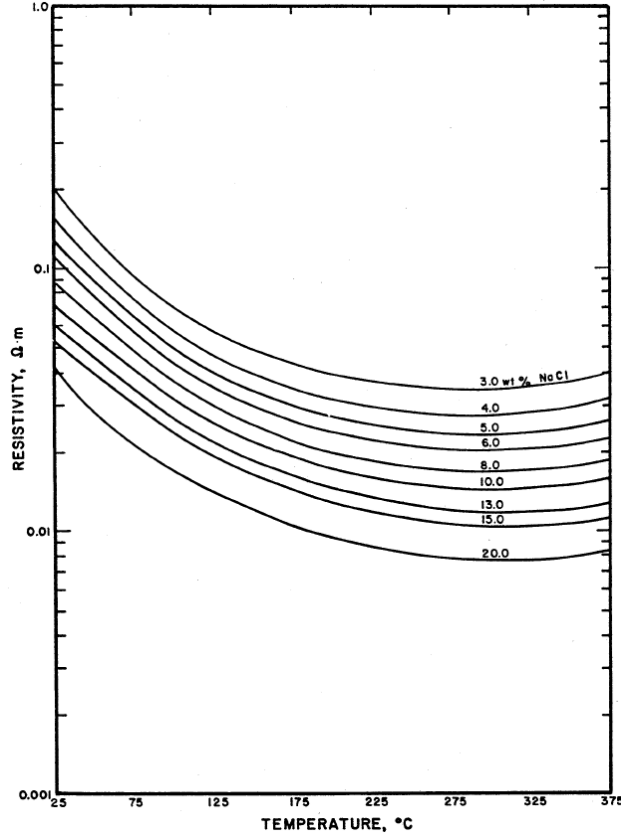


Figure 3.1: Resistivity of a NaCl solution as a function of temperature and concentration (Ucok et al., 1980).

Ucok et al. (1980) calculated that the dependence of resistivity is best represented by the formula:

$$\rho_w = b_0 + b_1T^{-1} + b_2T + b_3T^2 + b_4T^3 \quad (3.4)$$

where T is temperature and b are coefficients found empirically. The best fit for the concentration dependence was found to be

$$\rho_w = 10/(\Lambda c) \quad (3.5)$$

where

$$\Lambda = B_0 - B_1c^{1/2} + B_2c \ln c + \text{higher order terms} \quad (3.6)$$

Coefficients B depend on the solution chemistry and c is the molar concentration.

In this project, the tracer concentration resulting from the flow simulation is changed into molar concentration and the following B coefficient matrix for the three-dimensional

regression analysis of the data studied by Ucock et al. (1980) is used to calculate the resistivity of the NaCl solution,

$$B = \begin{matrix} & 3.470 & -6.650 & 2.633 \\ & -59.23 & 198.1 & -64.80 \\ 0.4551 & -0.2058 & 0.005799 & \\ -0.346E-5 & 7.368E-5 & 6.741E-5 & \\ -1.766E-6 & 8.787E-7 & -2.136E-7 & \end{matrix}$$

Then, the resistivity of water saturated rock, ρ , is calculated using Archie's law,

$$\rho = a\phi^{-b} \rho_w \quad (3.7)$$

where ϕ is the porosity of the rock and a and b are empirical constants, here a is set as 1 and b as 2. The resistivity value of each block, therefore depends on the tracer concentration in that block and the value decreases as more tracer flows into the block.

3.5 TWO SIMPLE FRACTURE NETWORKS

Flow simulations were performed using the EOS1 module in TOUGH2 reservoir simulator to see how a tracer, which increases the conductivity of the fluid, distributes after being injected into different reservoirs. The simulations were carried out on two-dimensional grids with dimensions $2000 \times 2000 \times 1 \text{ m}^3$ with fractures first modeled as a long path from the injector to the producer as shown in Figure 3.2 and then as a path straight from the injector to the producer, shown in Figure 3.3. The goal was to study the difference in potential field history between these two cases as conductive fluid is injected into the reservoir.

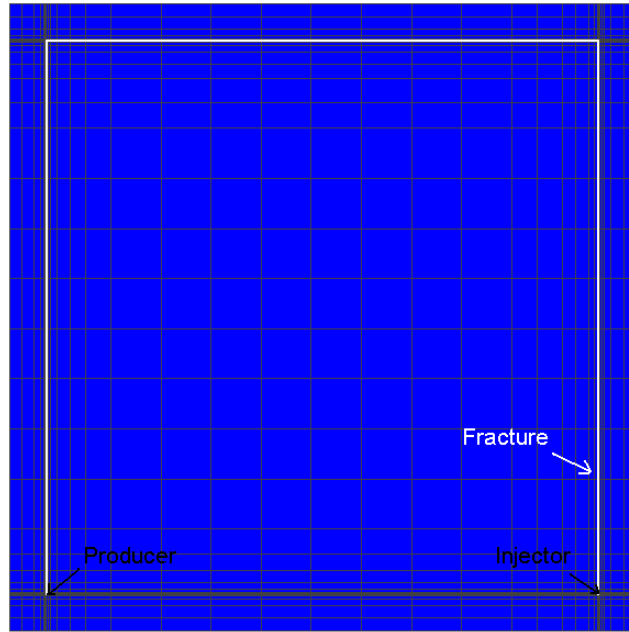


Figure 3.2: Reservoir with a fracture from the injector, around the reservoir and to the producer.

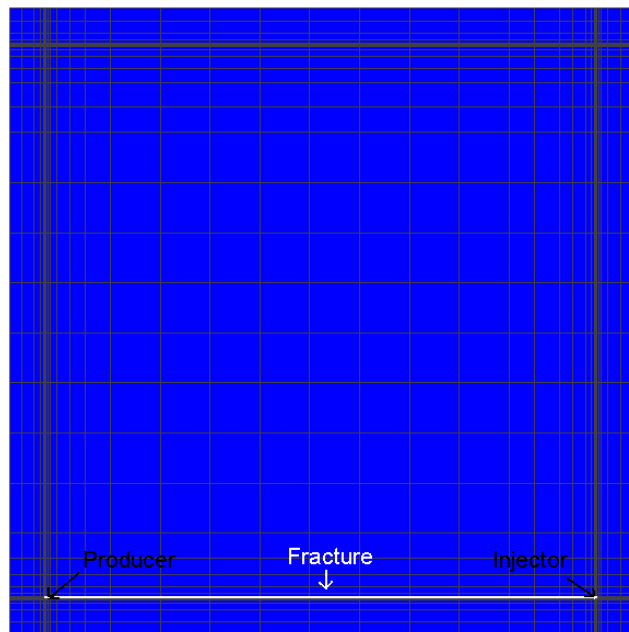


Figure 3.3: Reservoir with a fracture straight from the injector to the producer.

The reservoir is modeled with a porosity of 0.2 and a permeability of 10^6 md (10^{-9} m²) while the fractures have a permeability of 10^{11} md (10^{-4} m²). No-flow boundary conditions were used and 100 kg/s of water was injected in the lower right corner with enthalpy 100 kJ/kg, and 0.1 kg/s of tracer with enthalpy 100 kJ/kg. The initial pressure was set to 10^6 Pa, temperature to 150°C and initial tracer mass fraction to 10^{-9} because the simulator could not solve the problem with a zero initial tracer mass fraction.

The EOS9 module in TOUGH2 was used to calculate the electric potential distribution for the reservoirs in Figures 3.2 and 3.3. A current was set equal to 1 A at the injector and as -1 A at the producer and the potential field calculated based on the resistivity of the field at each time step. The pressure solved in a flow simulation is usually of higher magnitude than the voltage in the electric case. Therefore, in order to solve the electric problem using a flow simulator, some of the electric parameters need to be scaled. The initial pressure was set to 10^6 Pa and the injection to $\pm 1 \times 10^2$ kg/s, so the appropriate pressure had to be subtracted from the pressure results in order to obtain the electric potential results assuming initial voltage to be zero. The results were then multiplied by 10^7 to get the electric potential results in volts. Figures 3.4 shows how the potential difference, which corresponds to the changes in resistivity, between the injector and the producer changes with time for the reservoirs in Figure 3.2 and Figure 3.3.

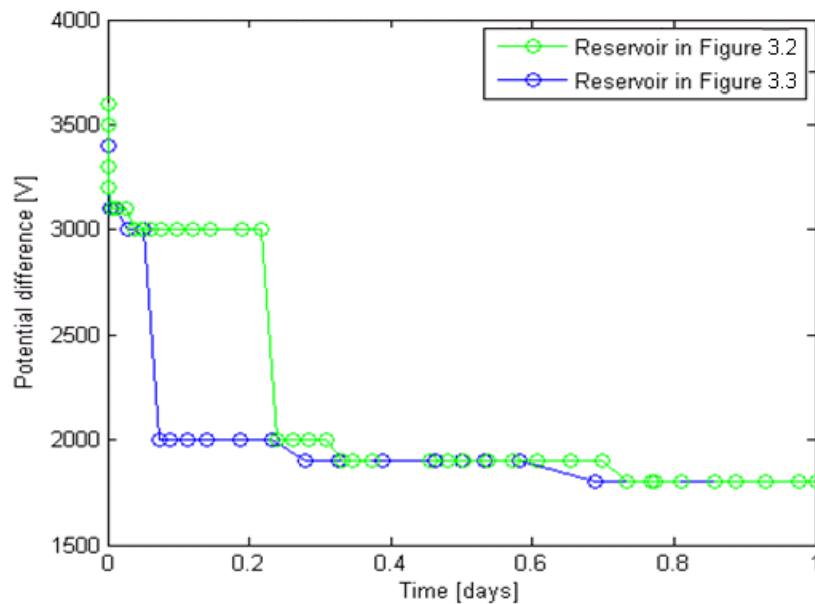


Figure 3.4: Potential difference between wells for reservoirs in Figure 3.2 and Figure 3.3

Figure 3.4 clearly illustrates that the electric potential history is different for the two fracture networks. After 0.239 days the potential difference plotted in green (reservoir in Figure 3.2) drops from 3000 V to 2000 V but the potential difference plotted in blue (reservoir in Figure 3.3) drops the same amount much earlier, or after 0.074 days. Therefore, these histories of the potential differences show that the conductive tracer flows faster through the fracture network in Figure 3.3 than in Figure 3.2 which tells us that the fracture path from the injector to the producer is shorter for that fracture network. In these examples, as well as in all following examples, it is assumed that the reservoir does not have any water until the conductive water is injected into the reservoir. The resistivity between the injector and the producer is therefore very high until the tracer reaches the production well, allowing the current to flow easily between the wells. When the tracer has gone fully through the fracture networks for both cases the potential differences are the same. These results show that the potential difference histories with conductive tracer flow

give valuable information about the fracture networks and can therefore help characterize the fractures.

3.6 DISCRETE FRACTURE NETWORKS

Discrete Fracture Network (DFN) models represent fracture-dominated flow paths in geothermal reservoirs more accurately since the fractures are treated discretely instead of being defined by high permeability values in course-scale grid blocks, as done in the previous example. By employing a DFN approach introduced by Karimi-Fard et al. (2003) we were able to generate a more realistic fracture network with fracture grid blocks of realistic dimensions. A MATLAB code written by Juliusson and Horne (2009) was used to generate a two-dimensional stochastic fracture network, run flow simulations on the network with TOUGH2, and plot the tracer flow results. EOS1 module in TOUGH2 was used to both solve the tracer flow as well as the electric flow. Figure 3.5 shows the fracture network generated, where the computational grid was formed using the triangular mesh generator Triangle, developed by Shewchuk (1996).

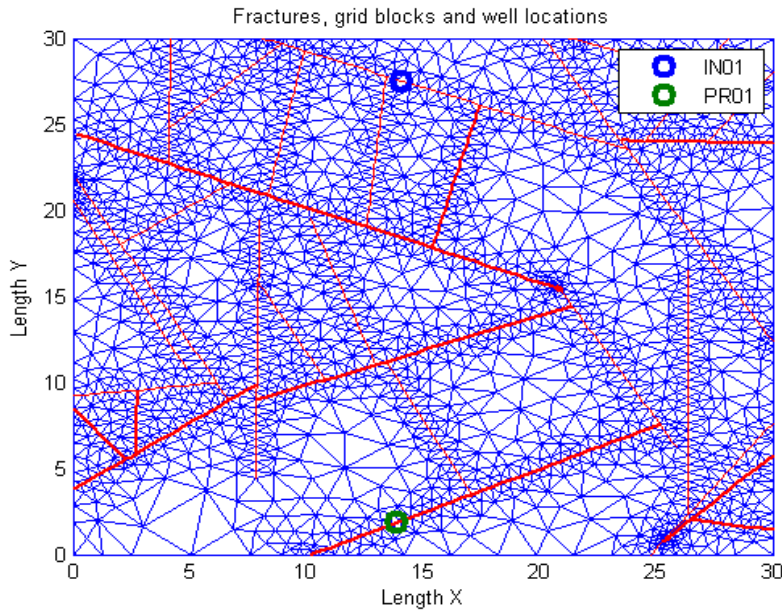


Figure 3.5: Two-dimensional discrete fracture network.

The dimensions of the two-dimensional grid were $30 \times 30 \times 1 \text{ m}^2$ and closed (no-flow) boundary conditions were used. The porosity of the fractures was set to 0.9 and the width, w , was assigned as a function of the fracture length L ,

$$w = L \cdot 10^{-2} \quad (3.8)$$

The corresponding permeability was determined by

$$k = \frac{w^2}{24} \quad (3.9)$$

The matrix blocks were given a porosity value of 0.12 and a very low permeability value so the conductive fluid only flows through the fractures.

By using the DFN approach every element (both triangles and fracture segments) was given a transmissibility value which is related to the flow between two adjoining elements as,

$$Q_{ij} = T_{ij}(p_j - p_i) \quad (3.10)$$

where Q is the flow rate between gridblocks i and j , T is the transmissibility and p is the pressure. More details on the approach can be found in the reference by Karimi-Fard et al. (2003).

Case 1

The well configuration for Case 1 is shown in Figure 3.5, an injection well at the top of the figure and a production well at the bottom. Water was injected at the rate of 5.6×10^{-2} kg/s with enthalpy 3.14×10^5 kJ/kg and the tracer injected was 0.1% of the water injected. The production well was modeled to deliver against a bottomhole pressure of 10^6 Pa with productivity index of 4×10^{-12} m³ (as specified for TOUGH2). The initial pressure was set to 10^6 Pa and the temperature to 25°C and the initial tracer mass fraction was set to 10^{-7} because TOUGH2 could not to solve the problem with initial tracer set as zero.

Figure 3.6 shows how the tracer concentration in the producer (green) changed with time as more tracer was injected into the reservoir.

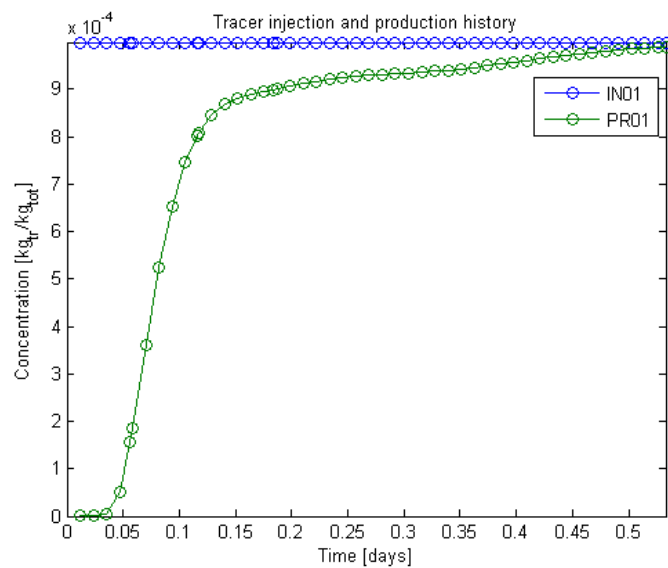


Figure 3.6: Tracer history at the injector and at the producer.

The electrical resistivity method described earlier was used to examine how the potential difference history, which corresponds to the changes in resistivity, relates to the fracture network. The current was set as 1 A at the injector and as -1 A at the producer and the potential field calculated. The potential difference between the injector and the producer drops very fast to begin with, as tracer is being injected, see Figure 3.7.

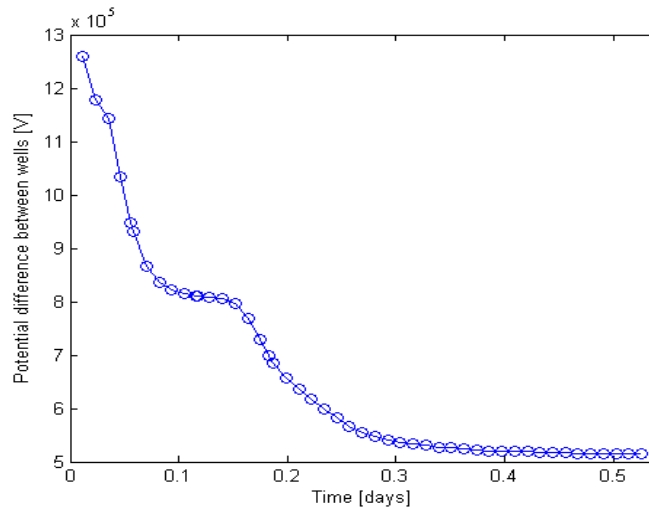


Figure 3.7: Potential difference between the injector and the producer.

After about 0.08 days the potential difference starts decreasing more slowly until after approximately 0.15 days where it drops relatively faster until it reaches about 5.2×10^5 V. Figure 3.8 shows the tracer distribution after approximately 0.01, 0.08, 0.15 and 0.35 days.

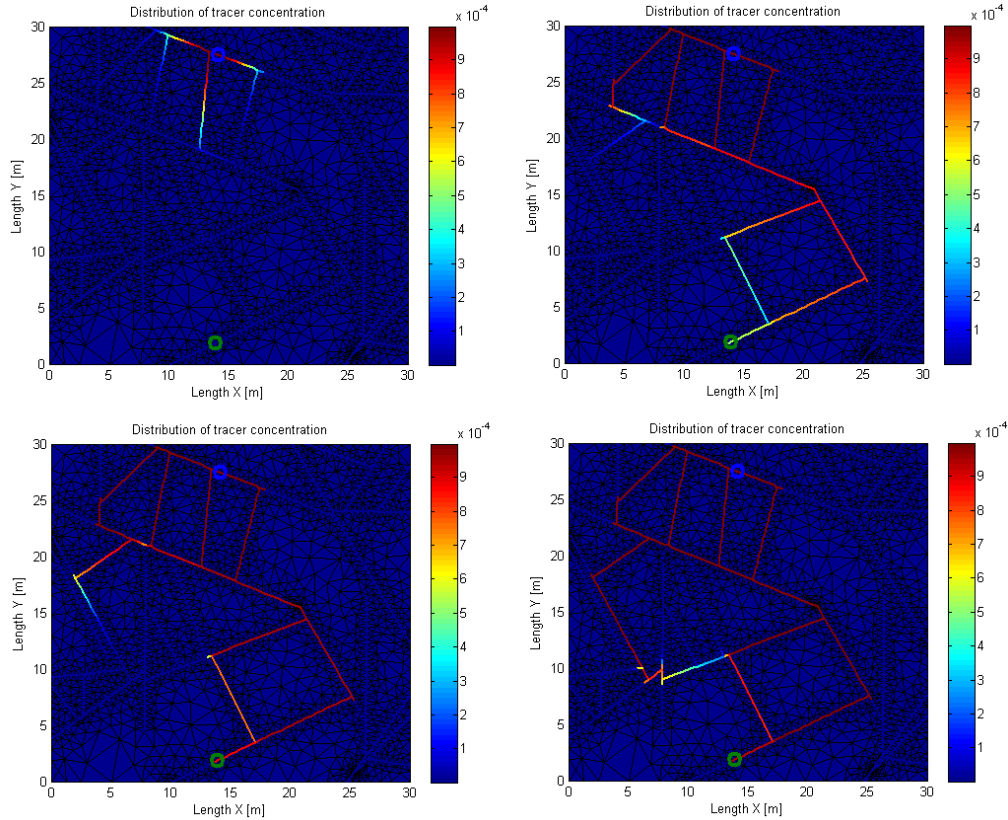


Figure 3.8: Tracer distribution in the reservoir after 0.01 days (upper left corner), 0.08 days (upper right corner), 0.15 days (lower left corner) and after 0.35 days (lower right corner).

By examining the tracer flow it can be seen that the potential difference starts decreasing more slowly as the tracer has reached the production well. As the reservoir has a very high resistivity until the tracer flows through the fractures it can be thought of as an electric circuit where in the lower left corner of Figure 3.8 the resistance is very high except for the formed path (in red) from the injector to the producer. Once these fractures have been filled the potential difference stops decreasing as much because the current will flow through the previously formed path until another path has been fully formed. When another path to the left has been formed, the ‘circuit’ has two paths connected in parallel, see lower right corner of Figure 3.8. Therefore, the potential difference starts dropping again until the second path to the left has also been fully concentrated with tracer. Once the tracer has entirely reached the producer from all possible fracture paths the potential difference stops decreasing.

Case 2

For the second case, the locations of the injector and the producer were switched. Now, after about 0.01 days the tracer flow has only been divided into two flow paths, see Figure 3.9, instead of three paths as for Case 1 (shown in the upper left part of Figure 3.8).

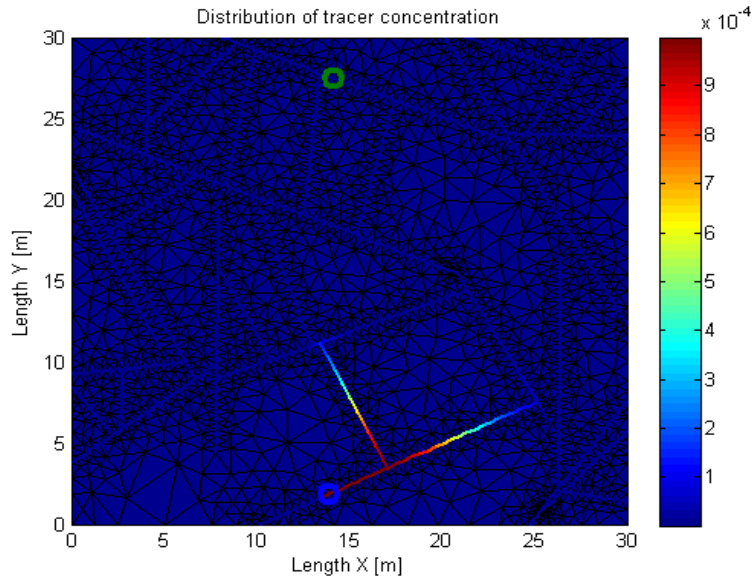


Figure 3.9: Tracer distribution in the reservoir for Case 2 after 0.01 days of tracer injection.

Therefore, the tracer in Case 2 is being distributed faster towards the producer which results in the potential difference dropping a little bit faster, as can be seen in Figure 3.10 where the potential difference time histories for Case 1 and Case 2 are compared.

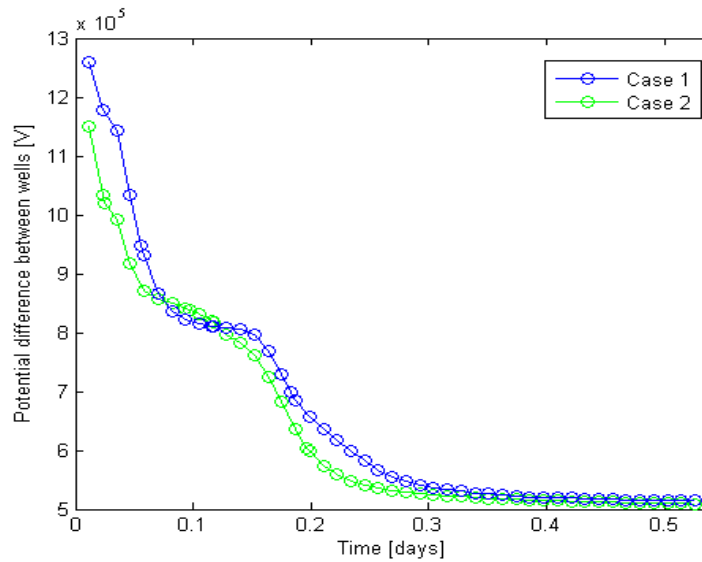


Figure 3.10: Time histories of potential differences for Case 1 and Case 2.

The potential fields are somewhat different for these two cases because the flow paths are different until the tracer has reached the production well through all possible fracture paths for both cases.

Case 3

In the third case, the injection well and the production well were located closer to each other, see Figure 3.11, to investigate whether the resistivity (or the potential difference) decreases faster than in previous cases.

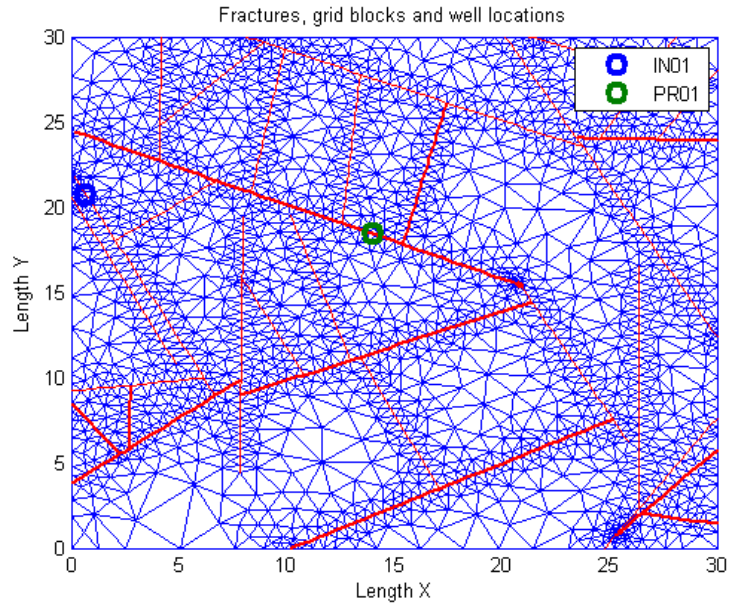


Figure 3.11: Two-dimensional discrete fracture network with the injector and the producer located close to each other.

The tracer distributes faster from the injection well to the production well than for Case 1, as can be seen by comparing Figure 3.12 to Figure 3.6, since the wells are connected and located closer to each other.

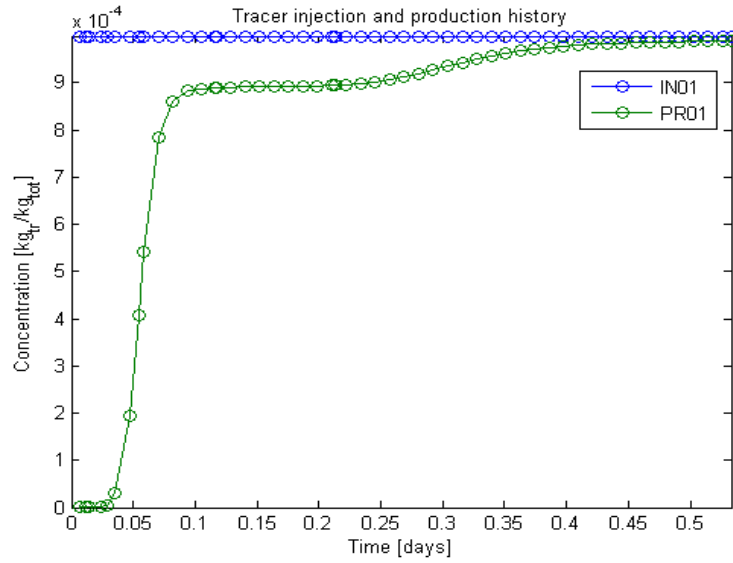


Figure 3.12: Tracer history at the injector and at the producer for Case 3.

After 0.09 days the tracer concentration at the producer has reached 8.8×10^{-4} , compared to only about 6×10^{-4} for Case 1 (see Figure 3.6). Figure 3.13 shows the potential difference for Case 3 as well as for Case 1.

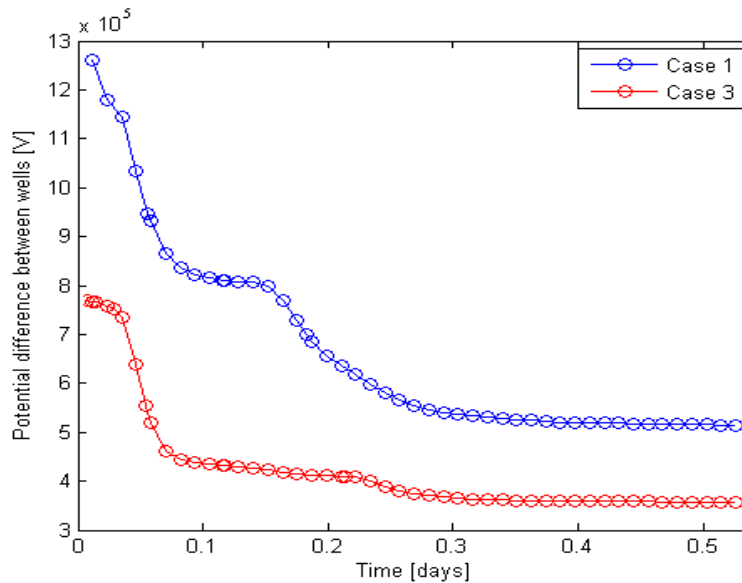


Figure 3.13: Time histories of potential differences for Case 1 and Case 3.

The potential difference is less for Case 3 since there is less distance between the wells and it has dropped all the way down to 4×10^5 V after only 0.08 days, which is close to the steady state difference, 3.6×10^5 V. Most of the current will go through the first path formed from the injector to the producer, even once another path has been formed because the second path is considerably longer than the first path. Therefore, the potential difference only drops slightly once the second path is formed. In Case 1, the potential difference has only dropped down to 8.4×10^5 V after 0.08 days but it drops down to 5.2

$\times 10^5$ V once the second path is formed since in that case similar amount of current will be flowing through the two different paths. The shapes of the two curves are therefore distinctive, since each one corresponds to its flow path, i.e. its fracture network.

Case 4

By increasing the number of wells more information can be provided and used to distinguish between possible fracture patterns. In Case 4, one injection well was modeled and two production wells, see well configuration in Figure 3.14.

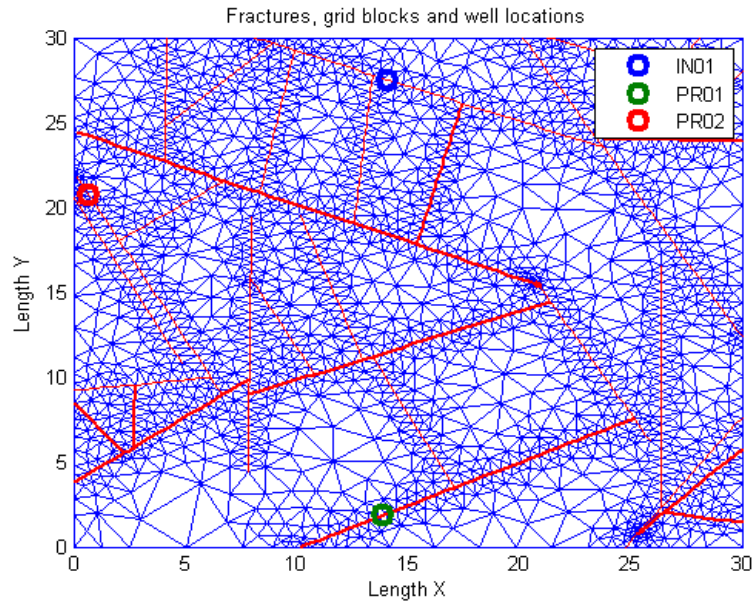


Figure 3.14: Two-dimensional discrete fracture network with one injector and two producers.

The injection was the same as for previous cases but now both producers were modeled to deliver against a bottomhole pressure of 10^6 Pa with productivity index of 4×10^{-12} m³. The potential differences between the injector and the two producers can be seen in Figure 3.15.

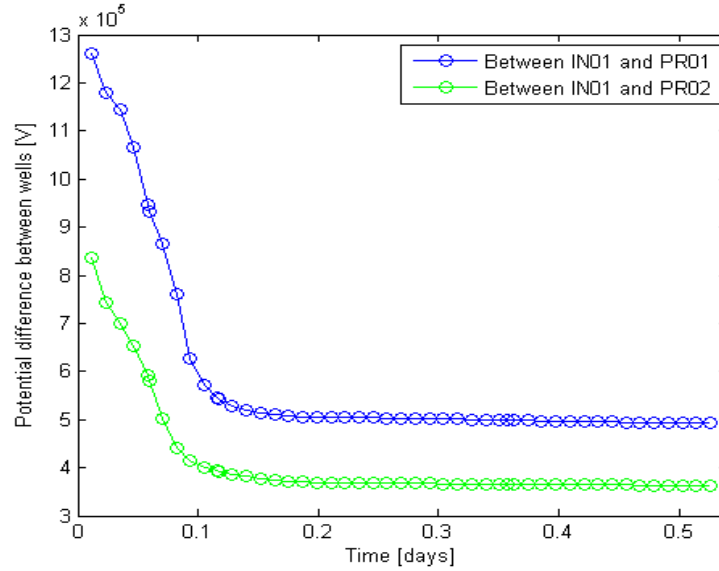


Figure 3.15: Time histories of potential differences between for Case 4.

The potential difference drops faster between injector IN01 and producer PR02 as expected because they are located closer to each other than IN01 and PR01. The shape of the curves are different from the curves in Figure 3.15 since the tracer is now being distributed through the network towards two production wells instead of one. The potential difference drops until after around 0.12 days when the tracer has reached both wells and thereby gone through all possible fractures towards the producers.

If the tracer flow is examined, see Figure 3.16, it can be seen that after 0.08 days when the tracer has reached the production well, both the left and the right paths of the fracture network have been formed with tracer for the electric current to go through.

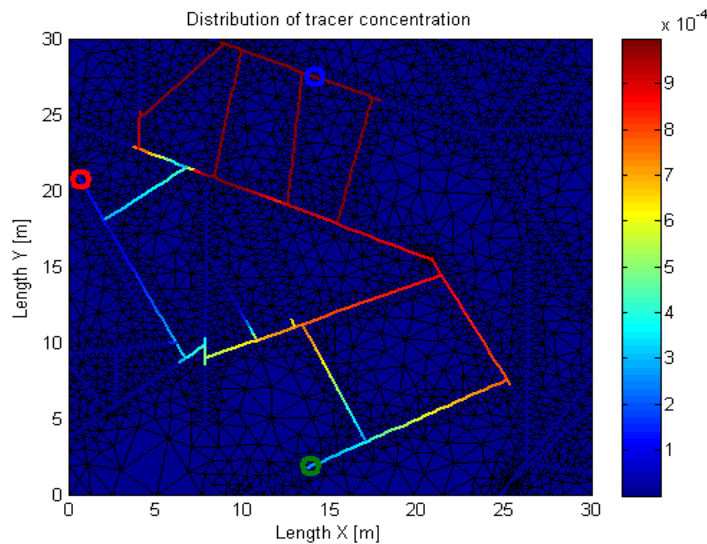


Figure 3.16: Tracer distribution in the reservoir for Case 4 after 0.08 days of tracer injection.

The potential difference will therefore keep dropping until both paths are fully concentrated with tracer instead of dropping until the first path is fully concentrated and then stop dropping until the second path is concentrated with tracer, as in Case 1. Figure 3.17 shows the potential difference for Case 4 compared to Case 1.

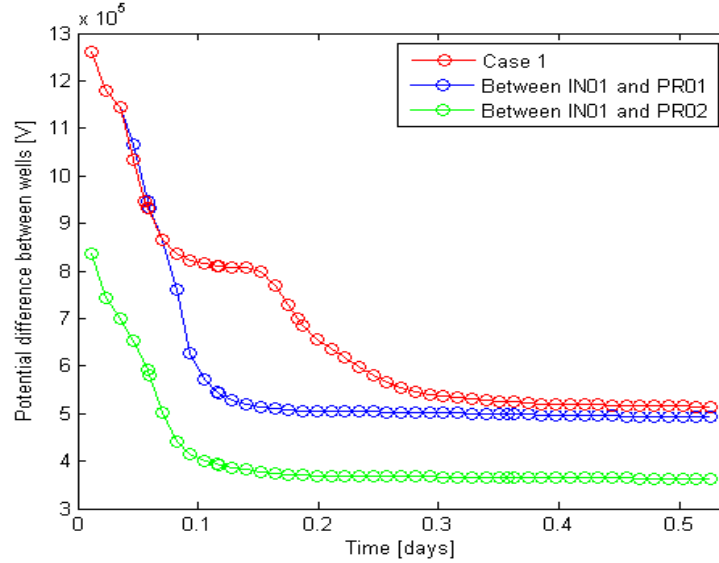


Figure 3.17: Time histories of potential differences for Case 1 and Case 4.

As mentioned previously, in Case 1 the current goes only through the right fracture path of the reservoir, which has the lowest resistance, until the tracer has reached through the whole left path. Therefore, the potential difference in Case 1 stops dropping once the fractures on the right part of the reservoir are fully concentrated with tracer and until the producer has gotten some tracer from the left path as well. In Case 4, the difference is that once the tracer has reached the right path it has also reached the left path, so instead of stop dropping the potential difference keeps going down until both paths are fully concentrated with tracer.

Different fracture patterns need to be studied to further understand that relationship but we ran into trouble when using the DFN code for other networks. Egill and Horne (2010) concluded that the problem is likely to be related to the time stepping algorithm and/or that the solvers used by TOUGH2 are not capable of solving the complex equations. Therefore, using the Stanford General Purpose Reservoir Simulator (GPRS) (Cao, 2002; Voskov, 2006) as they did instead of TOUGH2 might be necessary.

3.7 FUTURE WORK

Future work includes looking at more complicated and realistic fracture networks to study further the relationship between fracture networks and the change in potential differences as conductive tracer is injected into the reservoir. Future work also includes implementing self-potential calculations into the model since the change in self-potential affects the measured potential difference and could facilitate fracture characterization. It is of interest

as well to study the use of nanotracers and different chemical tracer as well as to explore the influence of injecting varying tracer concentration.

Other future goals are to use tracer concentration simulations and electrical potential calculations from TOUGH2 with inverse modeling to estimate the dimensions and topology of a fracture network. In inverse modeling the results of actual observations are used to infer the values of the parameters characterizing the system under investigation. In this study, the output parameters would be the potential differences between wells as a function of time and the input parameters would include the dimensions and orientations of the fractures between the wells. The objective function measures the difference between the model calculation (the calculated voltage difference between the wells) and the observed data (measured potential field between actual wells), as illustrated in Figure 3.18, and a minimization algorithm proposes new parameter sets that improve the match iteratively.

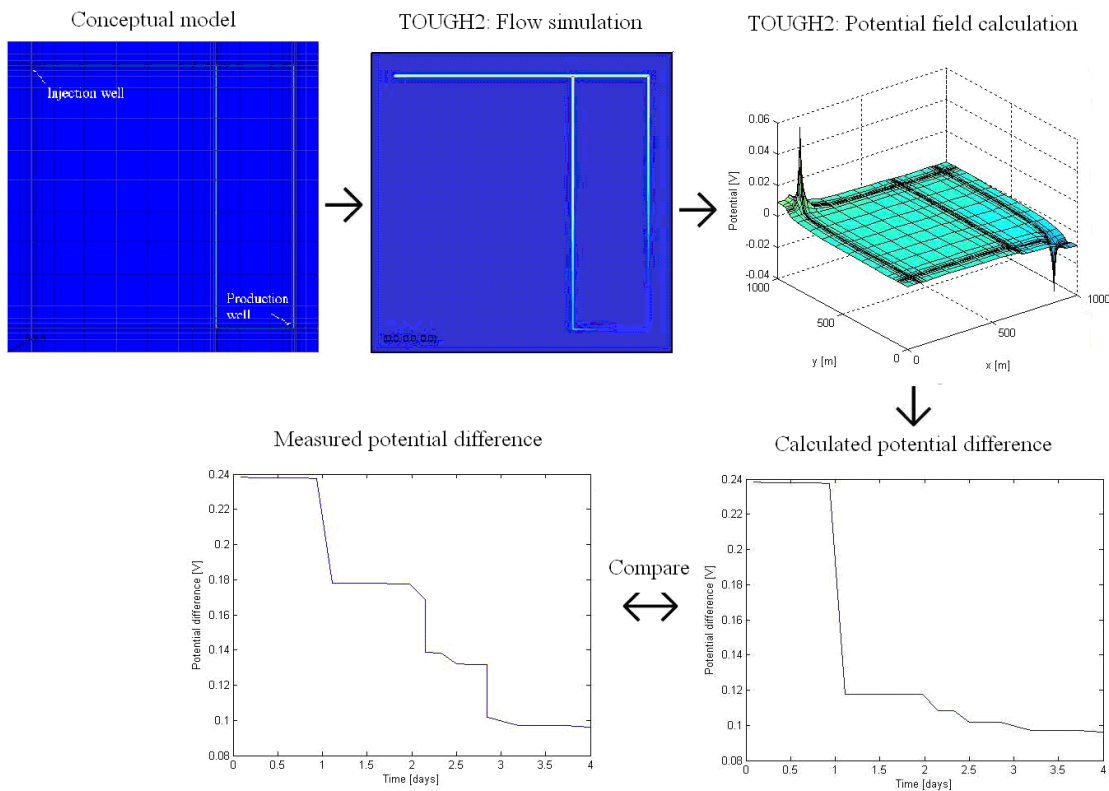


Figure 3.18: The inverse problem; the calculated potential difference is compared to the measured potential difference and the inverse problem solved to characterize fracture patterns.

The possibility of using fewer wells and different well arrangements will be studied to estimate the minimum number of measurement locations necessary to solve the problem. The objective is to develop a method which can be used to find where fractures are located and the character of their distribution.

4. FRACTURE APERTURE DETERMINATION USING THERMAL AND TRACER DATA

This research project is being conducted by Research Assistant Carla Kathryn Co and Professor Roland Horne. The overall objective of this study is to develop a methodology to estimate fracture dimensions. Our current focus is on utilizing thermal breakthrough and tracer return data to determine effective fracture apertures.

4.1 SUMMARY

This study aimed to determine an effective fracture aperture using tracer concentration and thermal breakthrough profiles. A single fracture was used to represent the connectivity between injection and production well pairs. An analytical model derived by Gringarten and Sauty (1975) was used to estimate the fracture aperture from thermal breakthrough time and mean tracer arrival time. Estimated effective fracture aperture values were from 2.1 cm to 42.6 cm.

To further understand the characterization of fractures, a literature review was undertaken. Fields included in this study were: Desert Peak, Nevada and Wairakei, New Zealand. Fracture properties were determined from acoustic imaging techniques. Feed zone locations identified through Pressure, Temperature, and Spinner (PTS) data were then correlated to these properties. Results showed that feed zone locations correspond to depths with higher apertures. Fracture density, however, was not found to be relevant to fluid entry zones.

Comparison of cooling rate predictions from three interwell connection models was done using data from Palinpinon Geothermal Field (Maturgo et al., 2010). These three models were: single fracture model; porous model with heat loss; and isotropic porous medium model (Bodvarsson, 1972) using the software ICEBOX. Results for temperature drawdown versus time showed that all three models predict values within 50°C. This illustrated the viability of using a single effective aperture to characterize producer-injector well connections and predict the thermal effect of different injection scenarios.

For this quarter, an extensive literature review was undertaken to investigate the possibility of integrating scaling relationships with heat and mass transport to improve the single effective fracture model. The main goal was to model fracture networks that are more consistent with the observed patterns in the field. Scaling relationships between relevant fracture properties such as aperture, length, and density were envisioned to become useful in constraining the possible models derived from tracer analysis and temperature matching. Field studies revealed that scaling had been observed in numerous geothermal fields in various scales ranging from thin sections to aerial photographs.

4.2 INTRODUCTION

Fracture aperture is an important parameter in geothermal reservoirs. Aperture influences transport and thermal behavior of the reservoir, both in EGS and in conventional hydrothermal systems. An important application is the determination of the degree of

interwell connectivity. Of critical importance is the prevention of thermal breakthrough from injection wells to production wells.

During the 1980s, several unsuccessful attempts were made to estimate fracture aperture by matching tracer test data. This was because the parameter estimation problem had multiple degrees of freedom, which made it difficult to separate fracture aperture from other unknown reservoir parameters. To constrain the degrees of freedom, thermal response data could be used. This was proposed in the 1980s; however at the time no data existed that provided both tracer and thermal responses. Now that several EGS and fractured reservoirs have been monitored to provide these data, the possibility exists to estimate fracture aperture in those fields. A single fracture model was used to describe the connectivity of an injection and production well pair. Tracer and thermal data were used to estimate the fracture width for this simplified model.

The objective of the initial work done was to determine whether it would be feasible to derive reasonable estimates for the fracture aperture using both thermal and tracer test results. Another objective was to document existing analytical models and field data available in literature. Moreover, calculated fracture width values were compared to those derived from other datasets to check for consistency. Afterwards, aperture values were reevaluated to account for the actual temperature ratio and to correct previous miscalculations. In addition, studies on fracture characterization using acoustic imaging were reviewed to develop a better understanding of feed zone related fractures. Several attempts to simulate a single fracture between wells were done but were not successful.

Cooling predictions from the fracture model were compared to those from two versions of porous models. One was a porous model with heat loss and the other was a tracer derived model calculated using ICEBOX software (Axelsson, 1995). This was done for the Palinpinon Geothermal field data (Maturgo et al., 2010). Focus this quarter has been on understanding the significance of the fracture aperture in predicting possible fracture network models. A comprehensive literature review of the scaling of fracture properties in geothermal reservoirs was undertaken to define the relationships among fracture aperture, length, and density.

4.3 METHODOLOGY

4.3.1 Analytical Model: Fracture Aperture

Gringarten and Sauty (1975) derived a solution that can be used for unsteady-state one-dimensional heat transfer through a fracture. The solution was similar to that for a porous medium, derived by Lauwerier (1955). The solution assumes a thin, uniform reservoir with an adiabatic boundary. Heat is transferred by conduction from the rock layers and the entering fluid. As no mixing is assumed, the result is a stream-like channel flow.

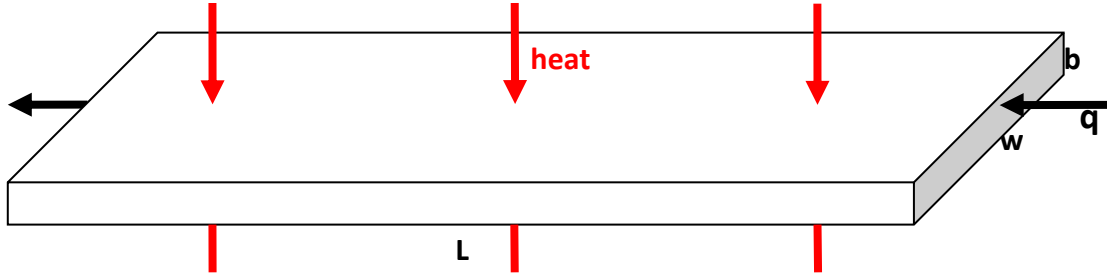


Figure 4.1 Model schematic for the Gringarten and Sauty (1975) derivation

Horne (1996) derived the resulting analytical solution for this model as Equation 4.1 where t_c is the tracer front arrival time, t_{th} is the thermal breakthrough time, and b is the fracture aperture. On the left hand side of Equation 4.1 is the relative temperature ratio T_{ratio} . Here, T_o is the original reservoir temperature, T_w is the reservoir temperature at x , and T_{inj} is the injected fluid temperature. Thus, the fracture aperture can be determined using the thermal and tracer breakthrough data. Knowledge of the fracture aperture can then be used to predict temperature drawdown in producing wells.

$$T_{ratio} = \frac{T_o - T_w}{T_o - T_{inj}} = \operatorname{erfc} \left\{ \left[\frac{(\rho_w C_w)^2}{K_r \rho_r C_r} \left(\frac{b}{t_c} \right)^2 (t_{th} - t_c) \right]^{-\frac{1}{2}} \right\} \quad (4.1)$$

$$b = \left\{ \left(\operatorname{erfc}^{-1} \left[\frac{T_o - T_w}{T_o - T_{inj}} \right] \right)^{-2} \frac{t_c^2}{(t_{th} - t_c)} \frac{K_r \rho_r C_r}{(\rho_w C_w)^2} \right\}^{1/2} \quad (4.2)$$

These are the analytical expressions used to model a single fracture connection between an injector and producer well pair. Equation 4.2 calculates the effective fracture aperture from the thermal arrival time t_{th} ; tracer front arrival time t_c ; and relative temperature ratio T_{ratio} .

4.3.2 Available field data

Results from tracer tests in EGS and conventional fractured geothermal reservoirs have been reported frequently in the literature. However, thermal breakthrough data are not as widely published. For EGS fields, thermal data are obtained usually from long-term circulation tests, as for example in Hijiori, Matsunaga et al. (2002) and Matsunaga et al. (2005). Historic silica geothermometer data are used from Palinpinon field which is a conventional liquid-dominated reservoir, Maturgo et al. (2010). Matsukawa is a conventional vapor-dominated field, Fukuda et al. (2006). Table 4.1 provides a summary of the field data used in this study. The thermal breakthrough time t_{th} here corresponds to the time it takes to reach a T_{ratio} of 0.5.

Table 4.1: Thermal and tracer breakthrough times from field data.

Field	Injector	Producer	t_c	t_{th}	Source
			Days	days	
Hijiori	HDR-1	HDR-2A	1	175	Matsunaga et al. (2002)
	HDR-1	HDR-3	4	266	Matsunaga et al. (2005)
Palinpinon	NJ2RD	NJ5D	15	730 ¹	Maturgo et al. (2010)
	SG2RD	NJ3D	28	365	
Matsukawa	M-6	M-8	1.5	146	Fukuda et al. (2006)

4.3.3 Single Fracture Model: Cooling Rate Prediction

$$T_w = T_o - (T_o - T_{inj}) \operatorname{erfc} \left\{ \left[\frac{(\rho_w C_w)^2}{K_r \rho_r C_r} \left(\frac{qb}{A_{tracer} x} \right)^2 \left(t - \left(\frac{\rho_A C_A}{\rho_w C_w} \right) \frac{A_{tracer} x}{q} \right) \right]^{\frac{1}{2}} \right\} \quad (4.3)$$

$$\rho_A C_A = \phi \rho_w C_w + (1 - \phi) \rho_r C_r \quad (4.4)$$

$$A_{tracer} = \phi A_{cross\ section} \quad (4.5)$$

$$A_{max} = \frac{q_{total}}{v_{mean}} \quad (4.6)$$

$$q = q_{total} \left(\frac{A_{tracer}}{A_{max}} \right) \quad (4.7)$$

The general equation for temperature versus time as derived by Gringarten and Sauty (1975) is shown in Equation 4.3. Here, x is the distance between the injection well and producer well. Thus, once the aperture b is determined, this equation describes the cooling of producing feed zones due to injection with constant volumetric rate (q) and temperature (T_{inj}). Note that q specified here is not the total injection rate. It is the rate of effective injected volume that goes to a particular producer. This is approximated by getting the ratio of the area derived from tracer analysis to the maximum area based on the total injection rate and the observed mean velocity from tracer data. Equations 4.5 to 4.7 illustrate these in more detail.

4.3.4 Porous Channel with Heat Loss Model: Cooling Rate Prediction

Maturgo et al. (2010) use tracer analysis to determine the effective area (A_{tracer}) for two injector and producer well pairs. These are NJ3D-SG2RD and NJ2RD-NJ5D. Using parameters from the general equation and the effective cross sectional area, thermal

¹ Assumed that injection in NJ2RD started in 1998 or 1 year before the start of drawdown in NJ5D based on the Palinpinon injection and production history discussed by Bayon and Ogena (2005).

velocity without heat loss (v_{th}) can be defined as shown in Equation 4.8. From this definition, Equation 4.3 can be rearranged to get Equation 4.9 which describes the cooling effect of injection for a porous connection model. As explained in the previous section, q is the effective volumetric injection rate.

$$v_{th} = \frac{q}{A_{tracer}} \frac{\rho_w C_w}{\rho_A C_A} = v_w \phi \quad (4.8)$$

$$T_w = T_o - (T_o - T_{inj}) \operatorname{erfc} \left\{ \left[\frac{(\rho_A C_A)^2 v_{th}^2 b^2}{K_r \rho_r C_r} \left(t - \frac{x}{v_{th}} \right) \right]^{-\frac{1}{2}} \right\} \quad (4.9)$$

4.4 PRELIMINARY CALCULATIONS AND RESULTS

4.4.1 Fracture Aperture

As described in the previous section, fracture aperture can be estimated directly from the thermal and tracer breakthrough times. Assumptions for the values of the other parameters are listed in Table 4.2. These are the values assigned to these properties in the estimation of fracture aperture. Actual temperature ratios for the injector-producer pairs derived from long term circulation test results are shown in Table 4.3. Estimated fracture aperture values are given in the same table.

Table 4.2: Assumptions used in calculations.

Rock thermal conductivity	K_r	2	W/m-C
Rock density	ρ_r	2200	kg/m ³
Water density	ρ_w	900	kg/m ³
Rock heat capacity	C_r	0.712	kJ/kg-C
Water heat capacity	C_w	4.342	kJ/kg-C

Table 4.3: Relative temperature ratios and calculated fracture aperture from thermal and tracer breakthrough times.

Field	Injector	Producer	T_{ratio}	Calculated b
				cm
Hijori	HDR-1	HDR-2A	0.46	2.1
	HDR-1	HDR-3	0.14	6.9
Palinpinon	NJ2RD	NJ5D	0.17	15.7
	SG2RD	NJ3D	0.07	42.6
Matsukawa	M-6	M-8	0.29 ²	3.5

² Assumed an injection temperature of 60°C

To determine the relative temperature for M-6 and M-8 in Matsukawa, a 60°C injection temperature was assumed. Estimates of effective fracture aperture b varied from 2.1 cm to 42.6 cm. Though the HDR-1 and HDR-2A well pair in Hijiori exhibited the shortest mean tracer arrival time, it had the lowest calculated effective aperture value because of the long thermal breakthrough time. This observation demonstrated the value of using both tracer and thermal results to constrain the effective aperture. Using this analytical solution also provided an alternative method to characterize the flow path between wells.

Results from finite element heat and mass transfer modeling (FEHM) of the Hijiori field demonstrates fracture aperture values of about 2 mm (Tenma et al., 2005). This is significantly lower than the calculated aperture values. Further investigation of results from aperture estimates from numerical modeling will be undertaken. However, effective fracture aperture derived from acoustic imaging logs show a range of values consistent with those calculated. The next section will describe these studies in detail.

4.4.2 Cooling Predictions

Comparison of cooling predictions was the most convenient way of relating the various producer-injector well connection models to each other. We wanted to investigate if the different models would give similar temperature drawdown profiles. Assumptions used for cooling rate calculations are shown in Table 4.4. Area values used to determine the effective injection rate going to the producer are in Table 4.5. These values were used by Maturgo et al. (2010) to predict the temperature drawdown due to injection at a constant rate (q_{total}) and temperature (T_{inj}). Palinpinon data was chosen because it had detailed cooling rate calculations available in literature. It also served as an additional verification of the validity of our models and the results of our calculations.

Table 4.4: Parameters used for cooling rate predictions

Field	Injector	Producer	q_{total}	T_o	T_{inj}	L
			m^3/s	C	C	m
Palinpinon	NJ2RD	NJ5D	0.178	265	160	1500
	SG2RD	NJ3D	0.117	265	160	1500

Table 4.5: Effective injection rate calculation

Field	Injector	Producer	A_{max}	A_{tracer}	q
			m^2	m^2	m^3/s
Palinpinon	NJ2RD	NJ5D	217.5	50.7	0.041
	SG2RD	NJ3D	175.8	39.7	0.027

Cooling rate or temperature drawdown predictions from three models were compared. First was the single fracture model as described in Equation 4.3. Next was the porous

model with heat loss using Equation 4.9. The third one was the isotropic porous medium model derived by Bodvarsson (1972) calculated using the ICEBOX software (Axelsson, 1995 and Axelsson, 2005). As described in the previous section, calculation of temperature drawdown for the first two models was straightforward. On the other hand, values for the third model were just lifted from the same paper where data for aperture calculations were obtained (Maturgo et al., 2010).

Figure 4.2 shows the results for NJ2RD-NJ5D while Figure 4.3 illustrates the forecast for NJ3D-SG2RD. Time in the x axis is measured from the start of injection. For NJ2RD-NJ5D, the fracture model gives a prediction very similar to the one using ICEBOX. However, the porous model for this well pair presents a more pessimistic temperature forecast. On the other hand, both the porous model and fracture model agree on a lower stabilized temperature than the ICEBOX model prediction for NJ3D-SG2RD as seen in Figure 4.3. It is still unclear why the three models behaved differently for these two scenarios. Still, it is good that all three models agree within a range of 50 °C. It proves that the effective single fracture aperture model is a viable one since it can be used to predict injection effects. Further investigation using numerical modeling as well as data from other geothermal fields will have to be made.

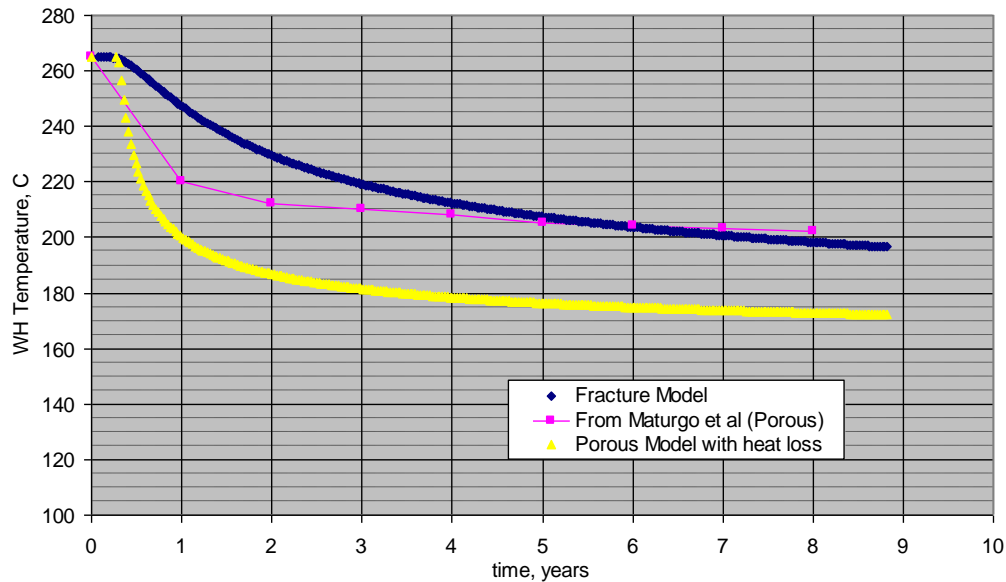


Figure 4.2 Comparison of cooling predictions for NJ2RD-NJ5D from different models: (1) fracture model; (2) porous model with heat loss; (3) ICEBOX (Maturgo et al., 2010).

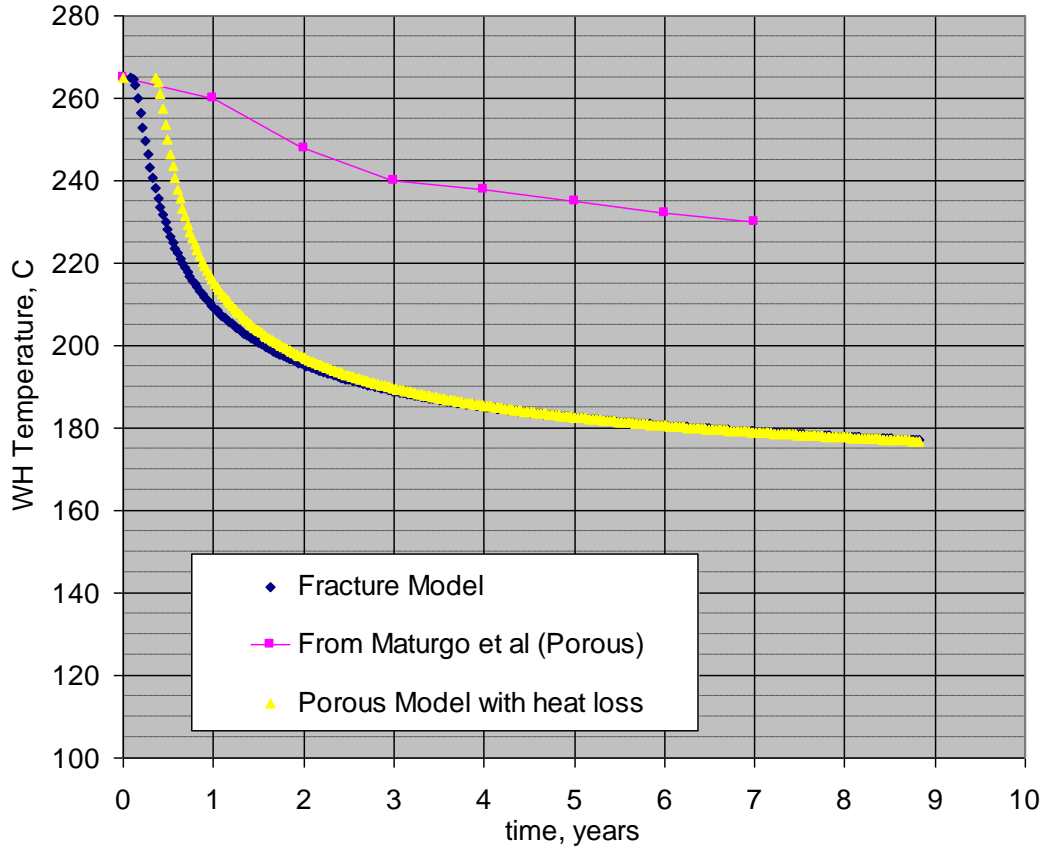


Figure 4.3 Comparison of cooling predictions for NJ3D-SG2RD from different models: (1) fracture model; (2) porous model with heat loss; (3) ICEBOX (Maturgo et al., 2010).

4.5 REVIEW OF RELATED LITERATURE

4.5.1 Acoustic Imaging

Characterization of fluid flow in fractures is an important area of study in geothermal reservoir engineering. Overall permeability in these reservoirs is fault-dominated (Massart et al., 2010). Relevant fracture parameters to fluid flow are: orientation, aperture, extension, and density. These parameters influence transport and thermal behavior of the reservoir, both in enhanced geothermal systems (EGS) and in conventional hydrothermal systems. Recent advances in borehole imaging technology have made it possible to measure fracture properties with greater accuracy.

For the Wairakei geothermal field, McLean and McNamara (2011) used a high temperature acoustic formation imaging tool (AFIT) to collect fracture data. Confidence, azimuth, and amplitude filters were applied to the data prior to analysis. A borehole televiewer (BHTV) similar to AFIT was used in the Desert Peak EGS project. In addition, formation microscanner (FMS) image logs were utilized (Devatzes, 2009).

Published fracture data from various geothermal fields were collected and analyzed. Data sets examined for this study are fracture aperture and density. These were then compared to locations of feed zones to determine their correlation with fluid flow properties. Fracture data from the various geothermal fields showed consistent correspondence between fracture apertures and feed zone locations for most of the data points. In Wairakei, fracture apertures for the feed zones ranged from 10 to 60 cm in wells WK-404, WK-318, and WK-407 (McLean and McNamara, 2011). A similar trend was observed from the Desert Peak data. Data for well 27-15 had aperture values from 3 to 10 cm at fluid entry zones (Devatzes, 2009). Feed zone locations, PTS data, and fracture apertures collected for various wells in Wairakei and Desert Peak are shown in Figures 4.4 to 4.7.

There are two possible explanations for this observation. Using a parallel-plate model, fracture permeability is proportional to b^3 , where b is the fracture aperture (Jourde et al., 2002). Fluid entry, associated to fractures in geothermal reservoirs, occurs at depths with high permeability. Therefore, feed zone locations will be at depths with high apertures. Another rationale is the power-law scaling between joint length and width described by Scholz (2010). He argued that for opening mode in rocks, fracture toughness scales linearly with \sqrt{L} and b scales linearly with L , where L is the length. Therefore, a larger fracture width will correspond to a longer fracture which implies a farther reach for the fluid source.

Marrett et al. (1999) analyzed data sets from natural faults and extension fractures and validated that the data follow power-law scaling in multiple-observational scales. Results from their study show that the power-law scaling applies across six ranges of scale within reasonable uncertainty limits. A similar behavior was observed by Massart et al. (2010) on fractures from the Soultz geothermal field. Thus, zones with higher fracture aperture values would have smaller fracture density values. Based on this, regions with fluid entry zones should have lower fracture densities. However, this was not consistently observed in all the data. The lack of inverse correspondence between fracture density and feed zone location could be due to the binning of data. Tool measurement uncertainties could also cause deviations. Moreover, there were inherent errors associated with the inverse scaling of fracture density and aperture.

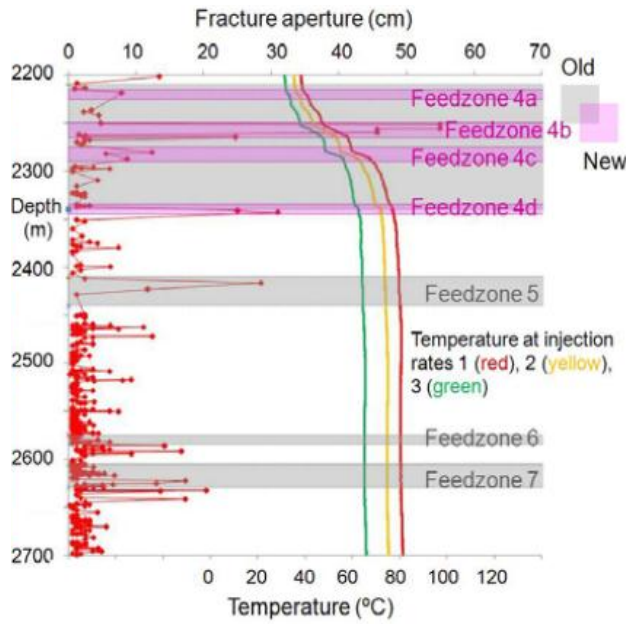


Figure 4.4 Fracture aperture (red) and temperature versus depth for well WK-404 in the Wairakei Geothermal Field (McLean and McNamara, 2011)

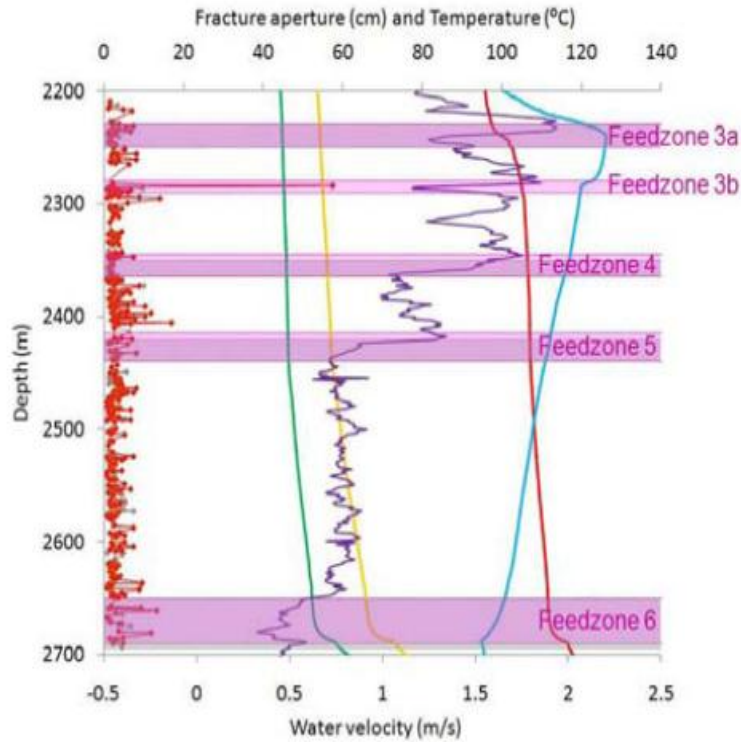


Figure 4.5 Fracture aperture (red), temperature, and spinner velocity (blue) versus depth log for well WK-317 in the Wairakei Geothermal Field (McLean and McNamara, 2011)

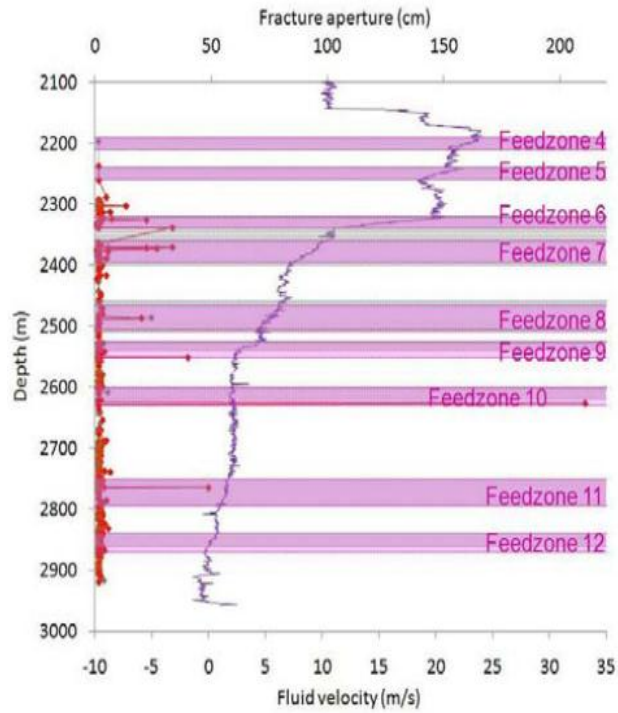


Figure 4.6 Aperture (red) and spinner velocity (blue) versus depth log for well WK-407 in the Wairakei Geothermal Field (McLean and McNamara, 2011)

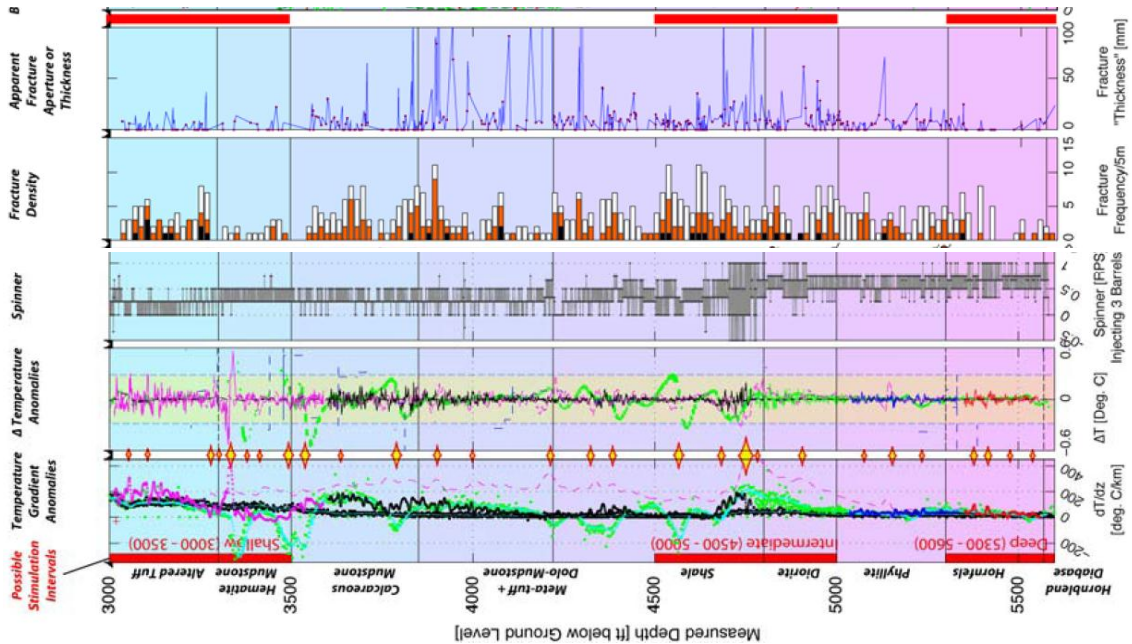


Figure 4.7 Well Log data for well 27-15 in the Desert Peak Geothermal Field, Nevada. Yellow diamonds indicate feed zones derived from temperature anomalies and spinner velocities (Devatzes, 2009)

4.5.2 Scaling Correlations

Aperture and Length Scaling (Opening Mode)

Olson (2003) describes the different mechanisms that lead to linear and sublinear scaling of aperture versus length for opening mode cracks. The two most relevant linear elastic fracture mechanics (LEFM) equations are the following:

$$\frac{b_{max}}{L} = \Delta\sigma \frac{2(1-\nu^2)}{E} = [p_f - \sigma_n] \frac{2(1-\nu^2)}{E} \quad (4.10)$$

$$\Delta\sigma = \frac{K_I}{\sqrt{\frac{\pi L}{2}}} \quad (4.11)$$

Equation 4.10 describes the relationship of the aperture (b_{max}) to the fracture length (L) for non-interacting opening mode fractures under plane strain conditions (Pollard and Segall, 1987). The other relevant parameters are: opening mode driving stress ($\Delta\sigma$), Poisson's ratio (ν), and Young's modulus (E). Another definition for the driving stress is ($p_f - \sigma_n$) where, p_f is the internal fluid pressure and σ_n is the remote normal compressive stress perpendicular to the crack. Furthermore, the driving stress ($\Delta\sigma$) for a uniformly loaded fracture can be expressed in terms of the stress intensity factor at the crack tip (K_I) and fracture length (L) as shown in Equation 4.11.

$$b_{max} = \Delta\sigma \frac{2(1-\nu^2)}{E} L = CL \quad (4.12)$$

Linear scaling can be derived from Equation 4.10 assuming a constant driving stress condition (Equation 4.12). Additionally, C is a constant representing material properties and external stress conditions. The possibility of reaching an unstable dynamic crack growth condition increases as the crack propagates. This is because at constant driving stress, the stress intensity factor (K_I) is proportional to the fracture length (L) (Equation 4.11). Moreover, the minimum requirement for crack propagation is for K_I to be equal to the intrinsic fracture toughness of the material (K_{Ic}). Therefore, extensive crack tip branching behavior should be observed where linear scaling is applicable. Olson (2003) states that this is only possible when there is relaxed loading such as after propagation. In contrast, Scholz (2010) argues that this is the predominant mode of scaling based on the reanalysis of data. Calculated (C) values range from 0.1 to 0.001 (Scholz, 2010).

$$b_{max} = \frac{K_{Ic}(1-\nu^2)}{E\sqrt{\pi/8}} \sqrt{L} \quad (4.13)$$

On the other hand, Olson (2003) claims that sublinear scaling is considered to be the most prevalent mechanism for most geologic conditions. Furthermore, Olson and Schultz (2011) insist that square root scaling provides the best fit for each data set. Sublinear or square root scaling can be derived from the assumption of constant stress intensity factor (K_I) equal to the intrinsic fracture toughness of the material (K_{Ic}) for critical crack propagation as presented in Equation 4.13 (Olson, 2003). Fracture arrest will occur once the internal fluid pressure goes down or the remote stresses are relieved due to

propagation. In addition, sublinear scaling can also happen for subcritical crack growth where the rock has less resistance to failure due to corrosive fluids and long-term loading.

$$b_{max} = CL^e \quad (4.14)$$

$$b_{max} = \frac{4}{\pi} b_{measured} \quad (4.15)$$

Fracture data from various fields across multiple length scales (1 cm to 2 km) were fitted to a power law equation (Equation 4.14). The maximum aperture (b_{max}) can be derived from the measured aperture ($b_{measured}$) using Equation 4.15 for an elliptical opening distribution. Here, e was the scaling exponent and C was a constant. Values calculated by Olson (2003) for e ranged from 0.38 to 0.41. The deviation from the predicted exponent value of 0.5 could be due to several other interfering factors. One example of this was the mechanical interaction of multisegment features. Thus, overlapping multisegment fractures would behave like one long fracture. Another was the presence of strata boundaries such that the aperture scales with the fracture height (H) instead of length (L).

Renshaw and Park (1997) examined data from the Krafla fissure swarm in Iceland and observed a break in slope for the aperture (b) versus length (L) when L reaches the maximum value. They postulated that this threshold value was the length at which the smaller apertures were affected by stress perturbations of larger fractures. Superlinear scaling was observed for smaller fractures while linear scaling was observed for larger ones.

4.5.3 Field Studies

Glynn-Morris et al. (2011) investigated the characteristics of feed zones of wells in the Wairakei and Tauhara Geothermal Fields in New Zealand. They sought to evaluate whether the permeability was derived from lithology or structures. Feedzone locations were identified from PTS logs and completions tests. The characteristic signature of primary permeability from lithology was a diffuse change in PTS reading. In contrast, structurally based secondary permeability demonstrated sharp variations in PTS logs. Other measured properties from drilled cores included the following: lithology, rock-quality designation (RQD), core recovery factor, loss circulation zones, porosity, smectite presence, rock strength, and core photos. It was concluded that secondary permeability from structures becomes more important as the feed zone depth increases.

On the other hand, steam production at The Geysers geothermal field was attributed to a network of fractures within a wide shear zone bounded by the right lateral Maacama and Collayomi Fault zones (Sammis et al., 1991). Steam feed zones were observed to occur in a few major fractures hosted in a relatively impermeable greywacke rock. Because steam feed zones were typically observed at shallow depths, this result contradicted the observations of the previous study discussed where shallow feed zones were attributed to lithology and not structures. Various methods for modeling fractured systems were the following: equivalent porous models, discrete fracture network models, statistical models, and multiporosity models such as Warren and Root.

Sammis et al. (1991) also observed that fracture patterns in shear zones were self-similar which meant that they could be characterized using fractal geometry. This rendered classical differential equations of transport for non-fractal media as inadequate. Hence, fracture networks on an outcrop from a freshly cut vertical wall (dm scale) were mapped and analyzed for the fractal dimension using the box counting method. Results confirmed self-similarity with the calculated fractal dimensions ranging from 1.87 to 1.926 (Sammis et al., 1991).

On a follow-up study (Sammis et al., 1992), similarity was investigated for other scales by analyzing two additional maps from larger scales. The first was from a road-cut outcrop (m scale) and the other was from a regional map of the area (km scale). Density versus fracture length scaling was observed in all length scales. Core observations were also performed. It was observed that most of the small fractures are sealed so a tentative conclusion was that transport occurs through large shear fractures. Using statistical analysis of the steam zone distributions, it was determined that the spacing of the relevant fractures was between 300 and 900 m (Sammis et al., 1992). Lastly, depths with high rate of penetration (ROP) over short distances in drilling logs were consistent with steam feed zone locations because they represent highly sheared rocks.

Different fractal analysis methods on various scales for two geothermal reservoirs, Germencik and Kizildere, in southwestern Turkey were done by Babadagli (2000). Analysis was done on four scales. Aerial photographs were used for the km scales and the calculated fractal dimensions were 1.575 and 1.583. Similarly, outcrop photos were used for the m scale and fractal dimensions ranged from 1.07 to 2. Furthermore, rock samples were analyzed for the cm scale which resulted to a fractal dimension range of 1.161 to 1.257. Lastly, thin sections were examined for the micrometer scale and the fractal dimension ranged from 1.011 to 1.039. Overall, linear scaling was consistently observed across all scales.

Tateno et al. (1995) studied cores from the Kakkonda geothermal field and also concluded that the fractures can be described by fractals. Another conclusion was that fractal dimensions varied with the fracture type and location due to the difference in fracture formation processes. Calculated fractal dimensions ranged from 0.38 to 0.53.

4.6 FUTURE WORK

The relationship between scaling properties and heat and mass transport will be further investigated. Fracture networks will be generated using the software Fracman using scaling properties. This generated network will then be used in a simulation. To avoid instability problems during numerical simulations in TOUGH2, the finite element code Feflow will be used instead. This program does not have phase change modeling capability; however, it would suffice for this particular modeling application because fluid is injected deep and hence remains as a single phase. Moreover, Feflow is more stable especially in handling

tracer modeling. The plan is that simulated results from the analytical model of the idealized fracture connection be compared to the simulated numerical models.

5. REFERENCES

- Alshehri, A., (2009). Low Tension Methods for Fractured Resources. Master thesis.
- Arnason, K.: Viðnámsmælingar í Jarðhitarannsóknum á Íslandi, Orkustofnun, Orkuþing (2001).
- Babadagli, T.: "Evaluation of outcrop fracture patterns of geothermal reservoirs in southwestern Turkey," *Proceedings, World Geothermal Congress*. 2000.
- Basel, E., Juliusson, E., and Horne, R. N.: A New Look at Well-to-Well Correlations using Nonparametric, Nonlinear Regression, *Thirty-Sixth Workshop on Geothermal Reservoir Engineering*, Stanford, (2011).
- Bayon, F.E.B. and Ogena, M.S.: "Handling the Problem of Rapid Reinjection Returns in Palinpinon-I and Tongonan, Philippines," *Proceedings, World Geothermal Congress*. 2005.
- Buckley, J.S. (1991): "Multiphase Displacements in Micromodels," *Interfacial Phenomena in Petroleum Recovery*, Morrow, N.R. (ed.), Marcel Dekker Inc., New York, NY, 157-189.
- Cao, H.: Development of techniques for general purpose simulators, Ph.D. Thesis, Stanford University, Stanford, CA (2002).
- Devatzes, N.C. and Hickman, S.H.: "Fractures, stress, and fluid flow prior to stimulation of well 27-15, Desert Peak, Nevada, EGS project," *Proceedings, 34th workshop on Geothermal Reservoir Engineering*, Stanford University. 2009.
- Devatzes, N.C. and Hickman, S.H.: "In-situ stress and fracture characterization for planning of an EGS stimulation in the Desert Peak Geothermal Field, Nevada," *Proceedings, 35th workshop on Geothermal Reservoir Engineering*, Stanford University. 2010.
- Fukuda, D., Akatsuka, T., and Sarudate, M.: "Characterization of inter-well connectivity using alcohol tracer and steam geochemistry in the Matsukawa vapor-dominated geothermal field, Northeast Japan," *GRC Transactions*. 2006, 797-801.
- Glynn-Morris, T., McLean, K., and Brockbank, K.: "Characterizing feed zones in geothermal fields: integrated learnings from completion testing, image logs and continuous core," *Proceedings, New Zealand Geothermal Workshop*. 2011.
- Gringarten, A.C. and Sauty, J. P.: "A theoretical study of heat extraction from aquifers with uniform regional flow," *Journal of Geophysical Research*. 1975, 4956-122.
- Holder, D.S.: *Electrical Impedance Tomography: Methods, History and Applications*, IOP, UK (2004).
- Hornbrook J., (1991). Visualization of Foam/Oil Interactions in a New, High Resolution Sandstone Replica Micromodel. Master thesis.

- Horne, R.N.: “Reservoir Engineering of Reinjection,” Course Notes. Stanford University, 1996.
- Horne, R.N., and Szucs, P.: Inferring Well-to-Well Connectivity Using Nonparametric Regression on Well Histories, *Thirty-Second Workshop on Geothermal Reservoir Engineering*, Stanford, (2007).
- Inwood, S., (2008). High-Resolution Microvisual Study of High Mobility Ratio, Immiscible Displacements. Energy Resources Engineering Department. Stanford University. Master thesis.
- Jourde, H., Flodin, E.A., Aydin, A., Durlofsky, L.J., Wen, X.H.: “Computing permeability of fault zones in eolian sandstone from outcrop measurements,” *American Association of Petroleum Geologists Bulletin*. 2002.
- Julusson, E, and Horne, R.N.: Fracture Characterization using Production and Injection Data, *DOE Quarterly Report (2009 January to March), Contract DE-FG36-08GO18182*, (2009), 1-17.
- Julusson, E, and Horne, R.N.: Study and Simulation of Tracer and Thermal Transport in Fractured Reservoirs, *Proceedings, 35th Workshop on Geothermal Reservoir Engineering*, Stanford University, Stanford, CA (2010).
- Julusson, E., and Horne, R. N.: Characterization of Fractures in Geothermal Reservoirs, *World Geothermal Congress*, International Geothermal Association, (2010).
- Julusson, E., and Horne, R. N.: Analyzing Tracer Tests during Variable Flow Rate Injection and Production, *Thirty-Sixth Workshop on Geothermal Reservoir Engineering*, Stanford, (2011).
- Karimi-Fard, M., Durlofsky, L.J. and Aziz, K.: An Efficient Discrete Fracture Model Applicable for General Purpose Reservoir Simulators, SPE 79699, SPE Reservoir Simulation Symposium, Houston, TX (2003).
- Kreft, A., and Zuber, A.: On the physical meaning of the dispersion equation and its solutions for different initial and boundary conditions, *Chemical Engineering Science*, **33(11)**, 1471–1480, Elsevier, (1978).
- Lee, K., Ortega, A., Jafroodi, N., and Ershaghi, I.: A Multivariate Autoregressive Model for Characterizing Producer Producer Relationships in Waterfloods from Injection/Production Rate Fluctuations, *SPE Western Regional Meeting* (2010).
- Marrett, R., Ortega, O.J., Kelsey, C.M.: “Extent of power-law scaling for natural fractures in rock,” *Geology*. 1999. 799-802.
- Massart, B., Paillet, M., Henrion, V., Sausse, J., Dezayes, C., Genter, A., Bisset, A.: “Fracture characterization and stochastic modeling of the granitic basement in the HDR Soultz Project (France),” *Proceedings, World Geothermal Congress*. 2010.
- Matsunaga, I., Yanagisawa, N., Sugita, H., Tao, H.: “Reservoir monitoring by tracer testing during a long term circulation test at the Hijiori HDR site,” *Proceedings*,

- Twenty-Seventh Workshop on Geothermal Reservoir Engineering, Stanford University. 2002.
- Matsunaga, I., Yanagisawa, N., Sugita, H., Tao, H.: "Tracer tests for evaluation of flow in a multi-well and dual fracture system at the Hijiori HDR test site," *Proceedings, World Geothermal Congress*. 2005.
- Maturgo, O.O., Sanchez, D. R., and Barroca, G.B.: "Tracer test using naphthalene disulfonates in Southern Negros Geothermal Production Field, Philippines," *Proceedings, World Geothermal Congress*. 2010.
- McLean, K. and McNamara, D.: "Fractures interpreted from acoustic formation imaging technology: correlation to permeability," *Proceedings, 36th workshop on Geothermal Reservoir Engineering, Stanford University*. 2011.
- Olson, J.E.: "Sublinear scaling of fracture aperture versus length: An exception or the rule?," *Journal of Geophysical Research*. 2003.
- Olson, J.E. and Schultz, R.A.: "Comment on "A note on the scaling relations for opening mode fractures in rock" by C.H. Scholz," *Journal of Structural Geology*. 2011, 1523-1524.
- Place, J., Garzic, E. L. E., Geraud, Y., Diraison, M., and Sausse, J.: Characterization of the Structural Control on Fluid Flow Paths in Fractured Granites. *Thirty-Sixth Workshop on Geothermal Reservoir Engineering*. Stanford, (2011).
- Pollard, D.D. and Segall, P.: "Theoretical displacement and stresses near fractures in rock: with applications to faults, joints, veins, dikes, and solution surfaces. In B.K. Atkinson, ed.," *Fracture Mechanics of Rock*, Academic Press Inc. 1987, 277-349.
- Pritchett, J.W.: Finding Hidden Geothermal Resources in the Basin and Range Using Electrical Survey Techniques. A Computational Feasibility Study (2004).
- Pruess, K. and Bodvarsson, G. S.: "Thermal effects of reinjection in geothermal reservoirs with major vertical fractures," *Journal of Petroleum Technology*. 1984, 1567-1578.
- Rangel-Germán, E., (2002). Water Infiltration in Fractured Porous Media: In-situ Imaging, Analytical Model, and Numerical Study. Energy Resources Engineering Department. Stanford University. PhD thesis.
- Renshaw, C.E. and Park, J.C.: "Effect of mechanical interactions on the scaling of fracture length and aperture," *Nature*. 1997, 482-484.
- Sagar, N.S. and Castanier, L.M. (1997): "Oil-Foam Interactions in a Micromodel," SUPRI TR110 Report, Stanford University.
- Sammis, C.G., An, L.J., Ershaghi, I.: "Fracture patterns in greywacke outcrops at the Geysers geothermal field," *Proceedings, 16th workshop on Geothermal Reservoir Engineering, Stanford University*. 1991.

- Sammis, C.G., An, L.J., Ershaghi, I.: “Determining the 3-D fracture structure in the Geysers geothermal reservoir,” *Proceedings*, 16th workshop on Geothermal Reservoir Engineering, Stanford University. 1992.
- Scholz, C.H.: “A note on the scaling relations for opening mode fractures in rock,” *Journal of Structural Geology*. 2010, 1485-1487.
- Shewchuk J.R.: Triangle: Engineering a 2D Quality ;Mesh Generator and Delaunay Triangulator, *Applied Computational Geometry: Towards Geometric Engineering*, **1148**, (1996), 203-222.
- Shewchuk, J. R.: Triangle: Engineering a 2D quality mesh generator and Delaunay triangulator, *Lecture Notes in Computer Science*, **1148**, 203–222, Springer, (1996).
- Singha, K. and Gorelick, S.M. Saline Tracer Visualized with Three-dimensional Electrical Resistivity Tomography: Field-scale Spatial Moment Analysis. *Water Resources Research*, **41**, (2005), W05023.
- Slater, L., Binley, A.M., Daily, W. and Johnson, R. Cross-hole Electrical Imaging of a Controlled Saline Tracer Injection. *Journal of Applied Geophysics*, **44**, (2000), 85-102.
- Sullera, M. M., and Horne, R. N.: Inferring injection returns from chloride monitoring data, *Geothermics*, **30(6)**, 591–616, Elsevier, (2001).
- Stacey, R.W., Li, K. and Horne, R.N.: Electrical Impedance Tomography (EIT) Method for Saturation Determination, *Proceedings*, 31st Workshop on Geothermal Reservoir Engineering, Stanford University, Stanford, CA (2006).
- Tateno, M., Watanabe, K., Nakatsuka, K., and Takahashi, H.: “Fractal Characterization of the Fracture Distribution and the Permeability in Geothermal Reservoirs,” *Proceedings*, World Geothermal Congress. 1995.
- Tenma, N., Yamaguchi, T., and Zyvoloski, G.: Variation of the characteristics of the shallow reservoir at the Hijiori test site between 90-days circulation test and long-term circulation test using FEHM code.” *Proceedings*, World Geothermal Congress. 2005.
- Ucok, H., Ershaghi, I. and Olhoeft, G.R.: Electrical Resistivity of Geothermal Brines, *Journal of Petroleum Technology*, **32**, (1980), 717-727.
- Urbino, E. G., and Horne, R. N.: Optimizing reinjection strategy at Palinpinon, Philippines, based on chloride data. *Sixteenth Workshop on Geothermal Reservoir Engineering*. Stanford, (1991).
- Voskov, D.: Description of the Thermal GPRS, Technical Report, Department of Energy Resources Engineering, Stanford University, Stanford, CA (2006).
- Wang, P. and Horne, R.N.: Integrating Resistivity Data with Production Data for Improved Reservoir Modeling, SPE 59425, SPE Asia Pacific Conference, Yokohama, Japan (2000).

Wang, Yuliang and Younan Xia (2004): "Bottom-Up and Top-Down Approaches to the Synthesis of Monodispersed Spherical Colloids of Low Melting-Point Metals," Nano Letters, 4(10), 2047-2050.